Extraction of Quark Distributions on Transverse Spin of the Nucleon at the HERMES Experiment

A Dissertation

By

Hidekazu Tanaka

February 2005

Department of Physics
Tokyo Institute of Technology

Abstract

This thesis describes extraction of the Collins and Sivers asymmetries for charged and neutral pions via measurement of the single-spin asymmetries with a transversely polarized hydrogen target at HERMES. Especially, this thesis stresses the Sivers function extracted from the observed Sivers asymmetries. The Sivers function is a parton distribution which depends on the intrinsic transverse momentum of the parton. This has never been measured before. The Sivers function has a nature of naive time reversal odd. Also the function provides information of the quark orbital angular momentum. EMC experiment reputed in 1988 that the quark spin contribution to the nucleon spin is small. In a series of experiments following EMC, the quark spin contribution to the nucleon spin measured to be 20 - 30%. Quark angular momentum obtained attention as it is one of the candidates to fill the missing fraction of the nucleon spin.

It had been thought that all transverse spin effects does not influence interaction of high energy particles, because the transverse spin is no longer eigenstate of transverse spin operator when it is boosted to infinite momentum frame. However from 70's to 90's, several experiments have been carried out to measure the "single-spin asymmetries A_N" (left-right asymmetry) with inclusive pion measurement using transversely polarized (unpolarized) proton beam and unpolarized (polarized) proton target. Large asymmetries have been observed depending on transverse momentum of final state hadron, whereas the theoretical expectation based on the naive parton model lead to $A_N = 0$.

To describe the single-spin asymmetries, two theoretical models are available at the moment, Collins [1] and Sivers [2] effects. Those were motivated by completely different mechanisms to generate the single-spin asymmetry. The Collins mechanism generates the single-spin asymmetries in *hadronization* processes, so this mechanism requires spin dependent fragmentation function, so-called *Collins function*. In contrast, Sivers effect originates from quark intrinsic transverse momentum. This mechanism is described with a parton distribution function, so-called *Sivers function*. Especially the Sivers function provides information on the quark orbital motion. If the Sivers function is found to be non-zero, it suggests non-zero quark orbital angular momentum which can contribute to spin structure of the nucleon.

It was not possible to separate these two mechanisms in inclusive measurement of pion production in hadron-hadron collisions. Up to now there are no experimental information on Collins and Sivers function, separately.

However those two effects can be disentangled in semi-inclusive measurement of deep inelastic scattering (DIS) using correlations between the direction of target nucleon polarization and the transverse momentum of the final state hadron. The HERMES experiment has carried out the measurement of single-spin asymmetries with the transversely polarized hydrogen target and the unpolarized positron beam from 2002.

The HERMES experiment is an experiment at DESY-HERA, designed to study the spin structure of the nucleon with deep inelastic scattering of positrons at 27.5 GeV off polarized internal gas targets.

This work aims to derive the Sivers function from the measurement of the single-spin asymmetries. This thesis describes a method to measure the single-spin asymmetries arising from the Sivers and Collins mechanisms, separately. HERMES experiment succeeded to separate the Sivers and Collins mechanisms for the first time, thanks to the asymmetry data from semi-inclusive measurements with hadron identification. The Sivers function is then actually extracted. The results are compared with theoretical predictions.

The observed Sivers type asymmetry of π^+ shows positive value with 3σ significance, for π^0 it is slightly positive 2σ level and for π^- it is consistent with zero within the statistical uncertainties. From these asymmetries, the Sivers functions for u- and d-quarks are derived. The extracted Sivers function for u-quark is negative, and d-quark is slightly positive. This is the first experimental results on the Sivers function.

Contents

Chapter 1

Introduction

Quantum Chromo Dynamics (QCD) is the theory of the strong interaction, which describes the interactions between quarks and gluons. One of the triumphs of QCD is that it has successfully accounted for the strong interaction processes observed at high energy particle colliders, and particularly phenomena such as 'jet' production in e^+e^- collision. Even with this success, QCD has not yet provided complete explanation on structure of hadrons. Such structure, at present, cannot be calculated from first principles. The main reason is that non-perturbative component is crucial in the confined structure. There are non-perturbative QCD tools, such as lattice QCD, they are under development. At this moment, experiment is the only way to extract information on non-perturbative confining effects in hadrons.

To explore the internal structure of hadrons, spin is a good probe. Such a well defined probe as spin guides us to a better understanding of confinement from first principles. A typical example which is revealed by experiment with spin is the nucleon spin structure. As we shall see in the following section, the experimental results suggest that the nucleon internal structure is considerably complicated than had been believed. Newly found quark distribution and fragmentation functions which have received a lot of attention recently are giving insights of such complexity of the non-perturbative structure of the nucleon and hadrons. These new functions are called as the Sivers function, transversity and the Collins function. In particular, existence of the Sivers function requires dynamic structure of the nucleon.

Historically, a picture that quarks are statically bound inside the nucleon has been predominant. Actually, before the appearance of the so-called "spin crisis" [3, 4], many of physical phenomena, such as baryon magnetic moment, are well explained with the simple static quark picture.

1.1 Spin Structure of the Nucleon

In general, spin 1/2 "point like" charged particles (Dirac particle) have magnetic moment of

$$\mu = g \cdot \frac{e}{2m} \cdot \frac{\hbar}{2} \tag{1.1}$$

where g is the g-factor and has a value of 2, except electromagnetic higher correction. The proton and neutron (collectively called nucleon) are also spin 1/2 particle, but measured magnetic moment of them are not consistent with 2,

$$\mu_p = \frac{g_p}{2}\mu_N = +2.79 \cdot \mu_N, \tag{1.2}$$

$$\mu_n = \frac{g_n}{2}\mu_N = -1.91 \cdot \mu_N, \tag{1.3}$$

$$\mu_N \equiv \frac{e\hbar}{2M_p},$$

where M_p is proton mass. This "anomalous magnetic moment" suggest that the nucleon is not point like particle and has structure in the interior of it. From the measured magnetic moment Eqs. (1.2) and (1.3), we can see a simple relation between proton and neutron,

$$\frac{\mu_n}{\mu_p} = \frac{-1.91}{+2.79} \simeq -\frac{2}{3}. \tag{1.4}$$

This result indicates an important information on the nucleon internal structure. In naive quark model (NQM), the nucleon consists of three Dirac particles, so-called quarks. For example, the proton consists of two *up*-quarks (u-quarks) and one *down*-quark (d-quark). This model provides a simple picture for the nucleon magnetic moment

$$\boldsymbol{\mu}_{p/n} = \sum_q \boldsymbol{\mu}_q, \tag{1.5}$$

where $\boldsymbol{\mu}_q$ is the quark magnetic moment. Proton magnetic moment is $\boldsymbol{\mu}_p = \boldsymbol{\mu}_u + \boldsymbol{\mu}_u + \boldsymbol{\mu}_d$, for example. The quark magnetic moment can be written as,

$$\boldsymbol{\mu}_q = g_q \, \frac{e_q\hbar}{2m_q} \, \boldsymbol{J}_q, \tag{1.6}$$

where m_q is quark mass, g_q is the g-factor of the quark, e_q is quark charge and has value of $e_u = +\frac{2}{3}e$, $e_d = -\frac{1}{3}e$, $\boldsymbol{J}_q$ is angular momentum of the quark.

Since the model assumes that the quark is Dirac particle, the g-factor g_q equals to 2. The expectation value of the $\boldsymbol{\mu}_{p/n}$ in Eq. (1.5) can be obtained using nucleon wave function. If the quarks are statically bound inside the nucleon (namely quarks does not have orbital angular momentum), the non-relativistic wave function can be expressed as,

$$|p^{\uparrow}\rangle = \sqrt{\frac{1}{18}}\left\{2\ |u^{\uparrow}u^{\uparrow}d^{\downarrow}\rangle - |u^{\uparrow}u^{\downarrow}d^{\uparrow}\rangle - |u^{\downarrow}u^{\uparrow}d^{\uparrow}\rangle + \text{permutation}\right\} \tag{1.7}$$

where arrows $\uparrow/\downarrow$ indicate proton and quark spin direction. For the statically bounded quark, only its spin is responsible for the total angular momentum given in Eq. (1.6), $\boldsymbol{J}_q = \boldsymbol{\sigma}_q/2$. Thus one can calculate the expectation value of quark spin for parallel and anti-parallel to the nucleon spin using Eq. (1.7).

$$\begin{aligned} u^{+} &\equiv \langle p^{\uparrow}|\sigma_{u^{\uparrow}}|p^{\uparrow}\rangle \overset{\text{NQM}}{=} \frac{5}{3}, \quad u^{-} \equiv \langle p^{\uparrow}|\sigma_{u^{\downarrow}}|p^{\uparrow}\rangle \overset{\text{NQM}}{=} \frac{1}{3}, \\ d^{+} &\equiv \langle p^{\uparrow}|\sigma_{d^{\uparrow}}|p^{\uparrow}\rangle \overset{\text{NQM}}{=} \frac{1}{3}, \quad d^{-} \equiv \langle p^{\uparrow}|\sigma_{d^{\downarrow}}|p^{\uparrow}\rangle \overset{\text{NQM}}{=} \frac{2}{3}. \end{aligned} \tag{1.8}$$

By introducing new symbol $\Delta q \equiv q^{+} - q^{-}$ which is the spin contribution of quark type q to the nucleon spin, the nucleon magnetic moment can be expressed as,

$$\langle p^{\uparrow}|\boldsymbol{\mu}_p|p^{\uparrow}\rangle \equiv \mu_p = \sum_{q=u,d}\langle p^{\uparrow}|\boldsymbol{\mu}_q|p^{\uparrow}\rangle \tag{1.9}$$

$$= g_u\,\frac{e_u\hbar}{2m_u}\left(\frac{\Delta u}{2}\right) + g_d\,\frac{e_d\hbar}{2m_d}\left(\frac{\Delta d}{2}\right) \tag{1.10}$$

$$\overset{\text{NQM}}{=} \frac{4}{3}\,\frac{e_u\hbar}{2m_u} - \frac{1}{3}\,\frac{e_d\hbar}{2m_d}, \tag{1.11}$$

where $g_u = g_d = 2$ was used. The neutron magnetic moment can be obtained by interchanging $u \leftrightarrow d$. If we take identical mass for u- and d-quarks ($m_u = m_d$), we can obtain the same results as in Eq. (1.4),

$$\frac{\mu_n}{\mu_p} = -\frac{2}{3}.$$

Moreover, it is also possible to compute each magnetic moment, μ_p and μ_n. For example, by taking the identical quark mass $m_{q=u,d} \simeq 0.336$ GeV/c^2 ($m_q \simeq 0.36\ M_p$) of "constituent quark mass" (or effective mass), the proton magnetic moment is obtained as,

$$\begin{aligned} \frac{\mu_p}{\mu_N} &= \frac{1}{\mu_N}\left\{\frac{4}{3}\left(\frac{e_u\hbar}{2m_u}\right) - \frac{1}{3}\left(\frac{e_d\hbar}{2m_d}\right)\right\} \\ &= \frac{1}{0.36} \simeq 2.78. \end{aligned} \tag{1.12}$$

Depending on the choice of the quark masses, the results can be slightly changed. However this simple picture well explains the nucleon anomalous magnetic moment [5, 6, 7].

Although the naive quark model provided successful explanation of nucleon anomalous magnetic moment, EMC group [3, 4] showed in 1998, the quark spin contribution, $\Delta\Sigma$, to nucleon spin is rather small, it is around 20 - 30%. The quark spin contribution $\Delta\Sigma$ is defined as sum of the Δq over possible quarks,

$$\Delta\Sigma = \Delta u + \Delta d + \Delta\bar{u} + \Delta\bar{d} + ... \tag{1.13}$$

So if the quarks are 100% polarized parallel to the nucleon spin, its spin contribution equals to $\Delta\Sigma = 1$ as the naive quark model predicted,

$$\frac{1}{2}\Big|_{\text{proton spin}} = \frac{1}{2}\Delta\Sigma \quad \Rightarrow \quad \Delta\Sigma = 1, \tag{1.14}$$
$$(\Delta u = 4/3, \quad \Delta d = -1/3)$$

but the experimental results suggest,

$$\frac{1}{2}\Big|_{\text{proton spin}} \neq \frac{1}{2}\Delta\Sigma \quad \Rightarrow \quad \Delta\Sigma = 0.2 - 0.3. \tag{1.15}$$

This means that the nucleon spin 1/2 cannot be reconstructed with sum of the quark spins alone. This is so-called nucleon "spin crisis". The measured quark spin contribution to the nucleon spin for each quark type, including sea-quarks, is [8, 9, 10],

$$\begin{aligned} &\Delta u \simeq +0.6, \\ &\Delta d \simeq -0.3, \\ &\Delta\bar{q} \sim 0. \end{aligned} \tag{1.16}$$

From the experimental results, it is thought that the nucleon spin can be reconstructed with total angular momentum of constituents [11] as,

$$\frac{1}{2} = \frac{1}{2}\Delta\Sigma + \Delta G + L_q + L_g \tag{1.17}$$

where ΔG is gluon spin contribution, $L_{q,g}$ is quark and gluon orbital angular momentum. As far as the nucleon magnetic moment is concerned, the gluon does not contribute to the magnetic moment because it is a neutral particle (at least in first approximation). Thus it can be attributed that the quark orbital angular momentum plays important roles for the missing piece of the

nucleon magnetic moment. Extending Eq. (1.10) with Eq. (1.17), the nucleon magnetic moment is rewritten as,

$$\mu_p = \sum_{q/\bar{q}} g_q \frac{e_q \hbar}{2m_q} \left(\frac{\Delta q}{2} + L_q \right) \tag{1.18}$$

Therefore, the sum of the quark orbital angular momentum should positively contribute to the magnetic moment since the quarks are not highly polarized as seen in Eq. (1.16). If we assume the quark orbital angular momentum L_q has similar behavior to the its spin Δq, the orbital angular momentum of the quarks can be expected as $L_u > 0$, $L_d < 0$ and $L_{\bar{q}} \simeq 0$. However, at the moment, there is no experimental information on the orbital angular momentum, because even definition of the orbital angular momentum of quark and/or gluon is not yet clear. As pointed out in reference [11], $\Delta\Sigma$ is measurable but other three components ΔG and $L_{q/g}$ are not: they are not gauge or renomalization invariant separately. This is because there are interaction between quarks and gluons in the framework of QCD.

Recent theoretical studies [12, 13] propose to express the nucleon spin with QCD angular momentum operator in its gauge invariant form [14],

$$\hat{J}_{QCD} = \hat{J}_q + \hat{J}_g. \tag{1.19}$$

Using this operator, the expectation value of the nucleon spin is decomposed as [15, 14],

$$\frac{1}{2} = \frac{1}{2}\Delta\Sigma(\mu) + L_q(\mu) + J_g(\mu) \tag{1.20}$$

where μ indicates renomalization scale and scheme dependence. As shown in above relation, the quark spin and quark orbital angular momentum can be expressed in gauge invariant form, separately. Thus in this framework, the quark spin, $\Delta\Sigma$, and orbital angular momentum, L_q, can be measured independently, but for the gluon, separation J_g into spin and orbital is gauge dependent [16]. By extending the QCD angular momentum, the orbital angular momentum can be defined with generalized parton distribution (GPD) function. One physics channel to access the quark orbital angular momentum is Deeply Virtual Compton Scattering (DVCS) [12, 17].

Also another possibility to access the orbital angular momentum is presently being studied. A new class of quark distribution functions depending on the intrinsic transverse momentum of the quarks inside the nucleon was introduced, with its most prominent member being the so-called Sivers function [2, 18]. Such distributions can only exist if the quark orbital angular

momentum is non-zero [19, 20]. A different approach of GPD [21, 22, 23] provides physical interpretation of the Sivers function. At the moment, no direct relation to the orbital angular momentum is available, but models at least see such a connection.

There are other interesting theoretical issues related to the nucleon magnetic moment and quark orbital angular momentum. Reference [24] proposes a new sum rules for quark spin contribution Δq and quark orbital angular momentum L_q as, $\Delta q + L_q = \delta q$, where δq is a quark distribution function, the so-called transversity. On the other hand, in reference [26], a relation between transversity (tensor charge) and the spin part of the quark magnetic moment is suggested.

The Sivers function and transversity can be accessed only through the quark fragmentation function. In particular, due to the chiral-odd nature of transversity, it has to be coupled to another chiral-odd object, which is the so-called Collins fragmentation function. The Collins function also has transverse momentum dependence. This transverse momentum dependence is the key to measure these two quark distribution functions: the Sivers function and transversity. As will be explained in the following chapters the transverse momentum dependence creates observable left-right asymmetries, the so-called Sivers and Collins asymmetries, which can be measured as single target-spin asymmetries in the semi-inclusive deep inelastic scattering (DIS) experiments.

This thesis describes the Sivers and Collins asymmetries measured at HERMES and its quark model interpretation. This thesis is organized as follows.

The second chapter describes single-spin asymmetry with theoretical overview of DIS. The third chapter provides an interpretation of the Sivers, the Collins functions and transversity and their connection to measurable single-spin asymmetries. The detector components of the HERMES experiment are described in the forth chapter. In the fifth chapter the measurement of the transverse single-spin asymmetry and the result of the measured asymmetries are described. In the sixth chapter, a smearing correction of the measured asymmetries is discussed. The extraction of the Sivers functions is described in the seventh chapter. The eighth chapter is the conclusion of this thesis.

Chapter 2

Single-Spin Asymmetry and Structure of the Nucleon

This chapter reviews the relevant theory of nucleon structure. After introductory review of historical background of single-spin asymmetry and relevant simple interpretation of the asymmetry, the chapter focuses on deep inelastic scattering (DIS). The spin nucleon structure in quark parton model will be discussed. The final sections of this chapter provide definition of the Sivers, Collins and transversity and related functions.

2.1 Single-Spin Asymmetry

Single-spin asymmetry in particle interactions is a well known phenomena such as the left-right asymmetry due to spin-orbit interaction. It has been thought that the single-spin asymmetry vanishes in high energy interactions because the transverse components of spin and momentum are suppressed. However in the 70's and 80's, single-spin asymmetries A_N (left-right asymmetry) have been observed in inclusive measurements of pion production using transversely polarized (unpolarized) proton beam of a few 10 GeV and unpolarized (polarized) proton target [27, 28, 29, 30]. The observed asymmetries increase as transverse momentum of the final state hadrons increases, whereas the theoretical expectation based on the naive parton model is $A_N = 0$.

Triggered by these experimental results, asymmetry measurement have been carried out at higher energy regions in proton-proton collision. A large left-right asymmetries shown in Fig. 2.1 have been observed with 200 GeV transversely polarized (anti-)proton beam by E704 experiment [31, 32] at Fermilab and recently at RHIC-STAR [33].

In order to explain these phenomena two mechanisms were proposed: the

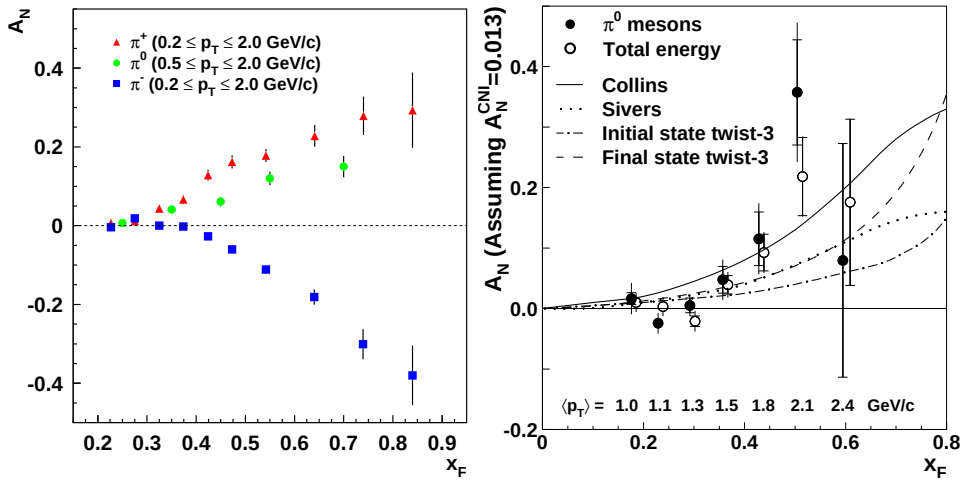

Figure 2.1: Single transverse-spin asymmetries A_N of inclusive measurement of pion production in proton-proton collision measured by E704 experiment [32] at Fermilab (left plot) and by STAR experiment [33] at BNL (right plot). In the left plot, A_N of π^+ (circle), π^- (square) and π^0 (cross) are shown as a function x_F. In right plot, A_N of π^0 (close mark) is shown.

Sivers and the *Collins* mechanisms. Both mechanisms lead to correlations between the momentum of the final state hadron P_h and the transverse spin of the nucleon $S_\perp$. But the ideas of these mechanisms arise from completely different motivations. D. Sivers [2] proposed that the source of the single-spin asymmetry is the orbital motion of the quark inside the nucleon. This mechanism is represented by a parton distribution function, the so-called Sivers function. On the other hand, J. Collins [1] proposed a spin dependent fragmentation function, the so-called Collins function, which generates the single-spin asymmetry.

However it was not possible to disentangle the two mechanisms in an inclusive measurement of pion production in hadron-hadron collision. At the moment, there is hence no reliable experimental information about the Collins and Sivers mechanisms. It should be noted that the Collins function can be measured in e^+e^- experiment, and the measurement of the Collins function is ongoing at Belle experiment (KEK) [34] and Babar experiment.

In contrast to hadron-hadron collisions, it is possible to separate the two effects in deep inelastic lepton scattering (DIS), since those two mechanisms lead to different correlation between P_h and $S_\perp$. In DIS with unpolarized

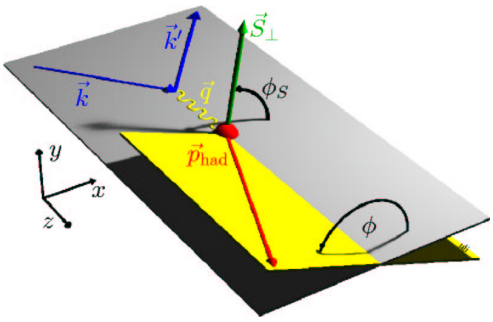

Figure 2.2: Definition of azimuthal angles, ϕ and ϕ_S. ϕ is the angle between lepton scattering plane and hadron production plane. ϕ_S is the angle between lepton scattering plane and hadron and target polarization plane.

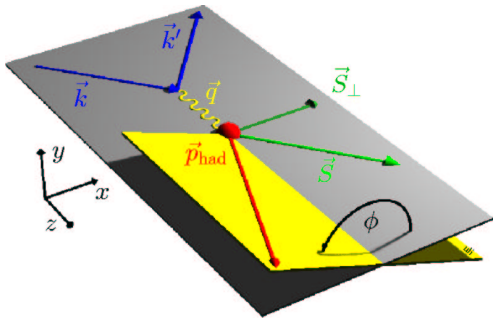

Figure 2.3: Definition of azimuthal angle ϕ in case of longitudinally polarized target. The *longitudinal* polarization is defined in parallel to the beam direction ($\vec{k}$). This corresponds to Fig. 2.2 in case of $\phi_S = 0, \pi$.

beam and transversely polarized target, the correlation between P_h and $S_\perp$ is described with two azimuthal angles, ϕ and ϕ_S. The definition of the azimuthal angles is illustrated in Fig. 2.2. The angle ϕ is defined as an angle between the lepton scattering plane and the plane determined by the momenta of virtual photon and produced hadron. The angle ϕ_S is as an angle defined between the lepton scattering plane and transverse component of the target polarization vector.

The P_h and $S_\perp$ correlation is translated as a combination of the azimuthal angles; $(\phi - \phi_S)$ for Sivers, $(\phi + \phi_S)$ for Collins mechanisms. From the references [35, 36], it is suggested that the single-spin asymmetry arising from the Sivers and Collins mechanisms have sine-type behavior; i.e. $\sin(\phi \pm \phi_S)$.

The HERMES experiment carried out measurement of single-spin asymmetry with unpolarized positron beam and polarized target. As the first step, the single-spin asymmetry with longitudinally polarized deuterium target has been measured [37]. Here *longitudinal* is defined in the direction parallel to the incoming positron beam. Thus there is a small but non-vanishing transverse spin component $S_\perp$ (see Fig. 2.3). The results are presented in Fig. 2.4. As shown in Fig. 2.4, the observed asymmetries show non-zero values and a $\sin(\phi)$ behavior. Even though the transverse spin component is small, this result suggests the Sivers and/or the Collins mechanisms. However the asymmetries obtained with longitudinal target do not allow us to disentangle the two contributions because ϕ_S is fixed with $\phi_S = 0, \pi$ as shown in Fig. 2.3.

If we use a transversely polarized target, the additional degree of freedom

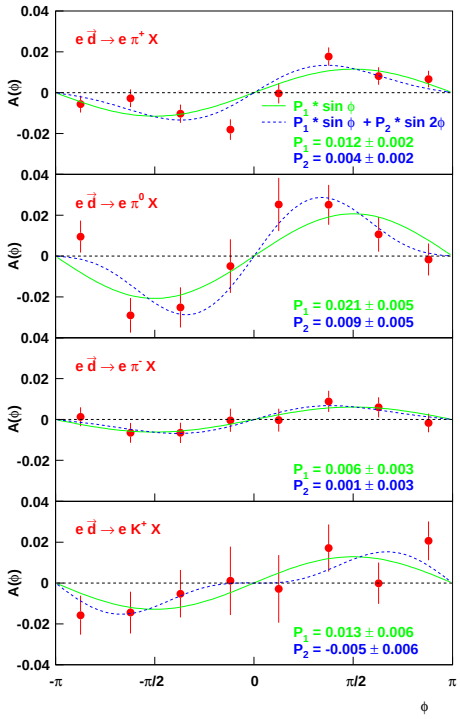

Figure 2.4: Single-spin asymmetries for π^+ (top), π^0 (second from the top), π^- (third from the top), K^+ (bottom) measured at HERMES with longitudinally polarized deuterium target and unpolarized positron beam [37].

ϕ_S is given. This will result in distinctive signatures: $\sin(\phi - \phi_S)$ for Sivers mechanism, $\sin(\phi + \phi_S)$ for Collins mechanism.

2.1.1 Sivers and Collins Functions in a Simple Parton Model

The Sivers and Collins mechanisms can be disentangled in DIS with transversely polarized target. Those mechanisms are described with the Sivers and Collins functions: the Sivers function is a parton distribution function, the Collins function is a fragmentation function.

Before describing details of the Sivers and Collins functions, a simple introduction to the Sivers and Collins functions is given. This discussion is

based on reference [38].

In order to introduce the functions, we consider single-spin asymmetries in the following reaction,

$$\gamma^* + N^\uparrow \to h + X, \tag{2.1}$$

where γ^* is the virtual photon, N is the target nucleon, h and X is final state hadrons. The superscript of N indicates the spin direction of the target nucleon. In this case, the nucleon spin is polarized transversely in upward direction ($\uparrow$). The reaction in Eq. (2.1) can be interpreted at a quark level reaction as

$$\gamma^* + \left(q^{\uparrow,\downarrow}\right) \to q'(\to h). \tag{2.2}$$

The cross section of this reaction can be expressed as a product of a parton distribution f and a fragmentation D functions,

$$d\sigma^\uparrow \sim f_\uparrow^\uparrow D(+\boldsymbol{\mathcal{P}}_{q'}) + f_\downarrow^\uparrow D(-\boldsymbol{\mathcal{P}}_{q'}) \tag{2.3}$$

where $f_\uparrow^\uparrow$ and $f_\downarrow^\uparrow$ are parton distribution functions which describes the probability to find the transversely polarized quarks parallel ($\uparrow$) or anti-parallel ($\downarrow$) to the nucleon polarization, $\pm\boldsymbol{\mathcal{P}}_{q'}$ is the spin polarization vector of the struck (final state) quark q'.

One can easily transform the expression of Eq. (2.3) as follows,

$$\begin{aligned} d\sigma^\uparrow &\sim \frac{1}{2}\left(f_\uparrow^\uparrow + f_\downarrow^\uparrow\right)\left[D(+\boldsymbol{\mathcal{P}}_{q'}) + D(-\boldsymbol{\mathcal{P}}_{q'})\right] \\ &+ \frac{1}{2}\left(f_\uparrow^\uparrow - f_\downarrow^\uparrow\right)\left[D(+\boldsymbol{\mathcal{P}}_{q'}) - D(-\boldsymbol{\mathcal{P}}_{q'})\right] \qquad (2.4) \\ &\equiv f^\uparrow \bar{D} + \frac{1}{2}\,\Delta f^\uparrow\,\Delta D(\boldsymbol{\mathcal{P}}_{q'}) \qquad (2.5) \end{aligned}$$

where we introduce new symbols for the difference and the sum of the parton distribution and fragmentation functions. These are defined as,

$$\begin{aligned} f^\uparrow &\equiv f_\uparrow^\uparrow + f_\downarrow^\uparrow & (2.6)\\ \Delta f^\uparrow &\equiv f_\uparrow^\uparrow - f_\downarrow^\uparrow & (2.7)\\ \bar{D} &\equiv \frac{1}{2}\left[D(+\boldsymbol{\mathcal{P}}_{q'}) + D(-\boldsymbol{\mathcal{P}}_{q'})\right] & (2.8)\\ \Delta D(\boldsymbol{\mathcal{P}}_{q'}) &\equiv D(+\boldsymbol{\mathcal{P}}_{q'}) - D(-\boldsymbol{\mathcal{P}}_{q'}) & (2.9) \end{aligned}$$

where $\bar{D}$ is found the quark spin averaged fragmentation function, $f^\uparrow$ is also (initial) quark spin averaged parton distribution function. The fragmentation

function $\bar{D}$ corresponds to usual unpolarized (spin averaged) fragmentation function D_1.

Similarly, one can obtain the downward polarized cross section as follows,

$$d\sigma^{\downarrow} \sim f^{\downarrow} D_1 - \frac{1}{2}\, \Delta f^{\downarrow}\, \Delta D(\boldsymbol{\mathcal{P}}_{q'}). \tag{2.10}$$

where $\Delta f^{\downarrow} \equiv f^{\downarrow}_{\downarrow} - f^{\downarrow}_{\uparrow}$ is used. Parity invariance gives $f^{\uparrow}_{\uparrow} = f^{\downarrow}_{\downarrow}$ and $f^{\uparrow}_{\downarrow} = f^{\downarrow}_{\uparrow}$. Thus $\Delta f^{\downarrow}$ satisfies the following relation,

$$\Delta f^{\uparrow} = \Delta f^{\downarrow} \equiv \Delta_T f. \tag{2.11}$$

A non-zero single-spin asymmetry suggests $d\sigma^{\uparrow} - d\sigma^{\downarrow} \neq 0$. This leads to the following result,

$$\begin{aligned} d\sigma^{\uparrow} - d\sigma^{\downarrow} &\sim \left(f^{\uparrow} - f^{\downarrow}\right) \bar{D} + \frac{1}{2}\left(\Delta f^{\uparrow} + \Delta f^{\downarrow}\right) \Delta D(\boldsymbol{\mathcal{P}}_{q'}) && (2.12)\\ &= \left(f^{\uparrow} - f^{\downarrow}\right) \bar{D} + \Delta_T f\ \Delta D(\boldsymbol{\mathcal{P}}_{q'}) && (2.13)\\ &\neq 0. && (2.14) \end{aligned}$$

This result suggests

$$\begin{aligned} \left(f^{\uparrow} - f^{\downarrow}\right) &\propto f^{\perp}_{1T} \neq 0, && (2.15)\\ \Delta D(\boldsymbol{\mathcal{P}}_{q'}) &\propto H^{\perp}_{1} \neq 0, && (2.16)\\ \Delta_T f &\propto h_1 \neq 0, && (2.17) \end{aligned}$$

where $f^{\perp}_{1T}$ is the Sivers function, and $H^{\perp}_{1}$ is the Collins function. This notations are based on the naming scheme in References [39, 40]; h_1 in the last line is the so-called transversity distribution.

The Sivers and Collins functions represent mechanisms to generate the single spin asymmetry. In particular, non-zero Sivers function indicates $f^{\uparrow} - f^{\downarrow} \neq 0$, namely unpolarized quark distribution is different in up and down nucleon spin state. This difference originates from the quark transverse momentum p_T.

2.1.2 Definition of Transverse Momenta

Quarks can have transverse momentum relative to their parent hadron momenta. The transverse momentum in the initial state is called "intrinsic transverse momentum p_T". It is defined relative to the momentum P of the target nucleon as shown in the left plot of Fig. 2.5. In the figure p indicates quark momentum in initial state. In the final state, the transverse momentum is k_T which is defined with respect to the momentum P_h of the produced

hadron as shown in the right plot of Fig. 2.5. In the figure, k indicates quark momentum in final state.

The parton distribution and fragmentation functions can be expressed as a function of transverse momentum.

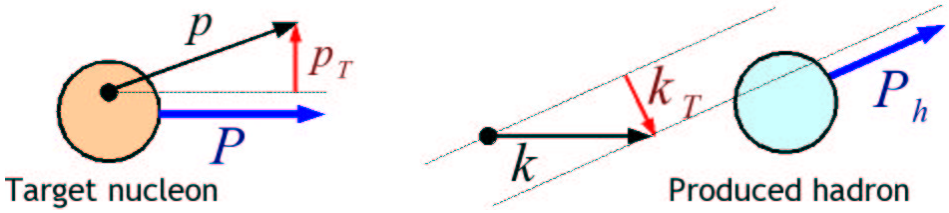

Figure 2.5: Definition of quark transverse momenta p_T and k_T.

2.2 Deep Inelastic Scattering

Deep inelastic scattering (DIS) has been used as one of the cleanest probe to investigate the nucleon structure, especially quarks and gluons. The lepton-hadron scattering with high momentum transfer produces one or more hadrons. Hence, it is described as,

$$l + N \rightarrow l' + X,$$

where l is the initial lepton, N is the target nucleon and l' is the scattered lepton, X is the final state hadrons.

Fig. 2.6 shows a schematic diagram of deep inelastic scattering. Using four-momentum of initial lepton $l^\mu = (E, \vec{l})$ and the four-momentum of final lepton $l'^\mu = (E', \vec{l'})$, the virtual photon four-momentum $q^\mu = l^\mu - l'^\mu$, where the squared momentum $q^2 < 0$ in the high energy region.

2.2.1 Kinematics

The main kinematic variables of DIS are listed together with expression in the target rest frame with labeled "Lab" below,

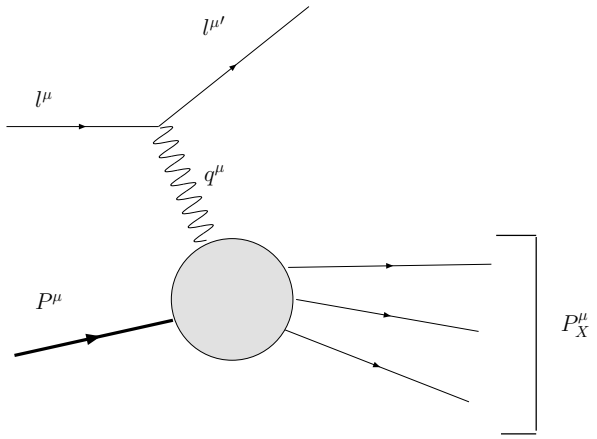

Figure 2.6: Diagram of a deep inelastic scattering.

$$
\begin{aligned}
&P \overset{\text{Lab}}{=} (M,0,0,0) \\
&Q^2 = -q^2 = -(l^\mu - l'^\mu)^2 \overset{\text{Lab}}{\simeq} 4EE' \sin^2 \frac{\theta}{2} \\
&\nu = \frac{P\cdot q}{M} \overset{\text{Lab}}{=} E - E' && \text{Energy transfer.} \\
&x = -\frac{q^2}{2P\cdot q} \overset{\text{Lab}}{=} \frac{Q^2}{2M\nu} && \text{Momentum fraction carried by quark.} \\
&y = \frac{P\cdot q}{P\cdot k} \overset{\text{Lab}}{=} \frac{\nu}{E} && \text{Energy fraction.} \\
&W^2 = (P^\mu + q^\mu)^2 \overset{\text{Lab}}{=} M^2 + 2M\nu - Q^2 && \text{Invariant mass of the final state hadrons.}
\end{aligned}
\tag{2.18}
$$

Usually in deep inelastic scattering, physics is described at the Bjorken limit, i.e. $Q^2, \nu \to \infty$, with x fixed.

2.2.2 Inclusive DIS Measurements

The differential cross section for inelastic scattering of leptons detected in the solid angle $d\Omega$ and in the final energy range $(E, E' + dE')$ is written in terms of the lepton and hadron tensors $L^{\mu\nu}$ and $W_{\mu\nu}$,

$$
\frac{d^2\sigma}{d\Omega\, dE'} = \frac{\alpha^2}{2Mq^4}\frac{E'}{E} L_{\mu\nu} W^{\mu\nu} \tag{2.19}
$$

where α is the fine structure constant. Here we start with the structure functions which can be accessed with inclusive DIS measurement. In 'inclusive' measurement only the scattered lepton is detected.

In the approximation of one photon exchange with a target nucleon, the lepton tensor is calculated from the spinors according to the Feynman rules,

$$L^{\mu\nu} = [\bar{u}(k', s'_l)\gamma^\mu u(k, s_l)] \cdot [\bar{u}(k, s_l)\gamma^\nu u(k', s'_l)]. \tag{2.20}$$

If we have a polarized beams, Eq. (2.20) is summed over final state (scattered) lepton spin, $s_{l'}$. Then the lepton tensor in Eq. (2.20) becomes,

$$\begin{aligned} L^{\mu\nu} &= \sum_{s'_l} [\bar{u}(l', s'_l)\gamma^\mu u(l, s_l)] \cdot [\bar{u}(l, s_l)\gamma^\nu u(l', s'_l)] && (2.21)\\ &= \mathrm{Tr}\left[(\not{l} + m_l)2^{-1}(1 + \gamma_5 \not{s}_l)\gamma^\mu (\not{l}' + m_l)\gamma^\nu\right] && (2.22)\\ &= 2\left[l^{\mu'} l^\nu + l^\mu l^{\nu'} - l \cdot l' g^{\mu\nu} - i\epsilon^{\mu\nu\alpha\beta} q_\alpha s_{l\beta}\right], && (2.23) \end{aligned}$$

where $s_{l\beta}$ is the spin four-vector of the incoming lepton and $\epsilon^{\mu\nu\alpha\beta}$ is the totally anti-asymmetric Levi-Civita tensor.

From Eq. (2.23), the lepton-tensor can be decomposed into two parts, spin-dependent (Symmetric) part and spin-independent (Asymmetric) part,

$$L_{\mu\nu} = L^{(S)}_{\mu\nu}(l; l') + iL^{(A)}_{\mu\nu}(l, s_l; l') \tag{2.24}$$

The hadronic tensor $W^{\mu\nu}$ is

$$\begin{aligned} W_{\mu\nu} &= \frac{1}{2\pi} \sum_X \int \frac{d^3\boldsymbol{P}_X}{(2\pi)^3 2E_X} (2\pi)^4 \delta^4(P + q - P_X) \\ &\quad \times \langle P, S|J^\mu(0)|X\rangle\langle X|J^\nu(0)|P, S\rangle && (2.25)\\ &= \frac{1}{2\pi} \int d^4\xi \ \mathrm{e}^{iq\cdot\xi} \langle P, S|J^\mu(\xi)J^\nu(0)|P, S\rangle. \end{aligned}$$

The hadronic tensor is similarly defined in terms of four structure functions as,

$$\begin{aligned} W_{\mu\nu} &= W_1(Q^2, \nu)\left(-g_{\mu\nu} + \frac{q_\mu q_\nu}{q^2}\right) && (2.26)\\ &+ \frac{W_2(Q^2, \nu)}{M^2}\left(P_\mu - \frac{P\cdot q}{q^2} q_\mu\right)\left(P_\nu - \frac{P\cdot q}{q^2} q_\nu\right) && (2.27)\\ &+ G_1(Q^2, \nu) M i\epsilon_{\mu\nu\lambda\sigma} q^\lambda S^\sigma && (2.28)\\ &+ \frac{G_2(Q^2, \nu)}{M} i\epsilon_{\mu\nu\lambda\sigma} q^\lambda (P\cdot q S^\sigma - S\cdot q P^\sigma), && (2.29)\\ & && (2.30) \end{aligned}$$

where S is the axial polarized vector of a spin-$\frac{1}{2}$ target. From the above equation, the hadronic tensor can also be decomposed into two separated parts: spin-independent term, (2.26),(2.27), and spin-dependent terms; (2.28), (2.29),

$$W_{\mu\nu} = W^{(S)}_{\mu\nu}(q;P) + iW^{(A)}_{\mu\nu}(q;P,S) \tag{2.31}$$

where the symmetric ($W^{(S)}_{\mu\nu}$) and anti-symmetric ($W^{(A)}_{\mu\nu}$) parts are expressed in terms of structure functions.

Then introduce dimensionless structure functions for the symmetric part.

$$F_1(x,Q^2) = MW_1(Q^2,\nu), \tag{2.32}$$

$$F_2(x,Q^2) = \nu W_2(Q^2,\nu). \tag{2.33}$$

Measurements of the structure functions of the proton reveal that they depend only very weakly on Q^2, which is called Bjorken scaling. This indicates that the proton consists of point like sub-particles which is called partons. Furthermore, the Callan-Gross relation

$$F_1 - \frac{1}{2x}F_2 \sim \frac{1}{\ln Q^2} \tag{2.34}$$

$$F_2(x) = 2xF_1(x) \tag{2.35}$$

is measured to be valid to a high degree. This relation is a direct consequence of the spin-$\frac{1}{2}$ property of the quarks inside the proton because the relation is only true for the scattering of point-like spin-$\frac{1}{2}$ particles by exchange of a vector boson.

Similarly to the spin-independent case, two dimensionless spin structure functions are introduced,

$$g_1(x,Q^2) = M^2\nu G_1(Q^2,\nu), \tag{2.36}$$

$$g_2(x,Q^2) = M\nu^2 G_2(Q^2,\nu). \tag{2.37}$$

The structure function g_1 represents the helicity structure of the nucleon.

2.3 The Nucleon Structure

The nucleon internal structure can be described by means of the structure functions Eqs. (2.32)-(2.37). If we like to investigate the nucleon structure at quark level, the decomposition of the hadron tensor into the structure functions is not sufficient. It does not give information on the connection to quark content.

2.3.1 Hadronic Tensor and Quark-Quark Correlation

In order to describe the nucleon structure in the quark-parton model, the hadronic tensor Eq. (2.25) is rewritten by a handbag diagram shown in Fig. 2.7,

$$\begin{aligned} W_{\mu\nu}(q,P,S) &= \frac{1}{2\pi}\sum_q e_a^2 \sum_X \int \frac{d^3\boldsymbol{P}_X}{(2\pi)^3 2E_X} \int \frac{d^4p}{(2\pi)^4} \int \frac{d^4k}{(2\pi)^4} \\ &\times (2\pi)^4\delta^4(P-p-P_X)(2\pi)^4\delta^4(p+q-k) \\ &\times \Big(\left[\bar{u}(k)\gamma^\mu \phi(p;P,S)\right]^* \left[\bar{u}(k)\gamma^\nu \phi(p;P,S)\right] \\ &+ \left[\bar{\phi}(p;P,S)\gamma^\mu u(k)\right]^* \left[\bar{\phi}(p;P,S)\gamma^\nu u(k)\right] \Big). \end{aligned} \tag{2.38}$$

where p and k are quark momenta before and after interaction with the virtual photon, P and S indicate the nucleon momentum and its spin. The hadronic tensor can be decomposed into two parts, hard process and soft process as shown in Fig. 2.7. The *soft* part contains a non-perturbative QCD

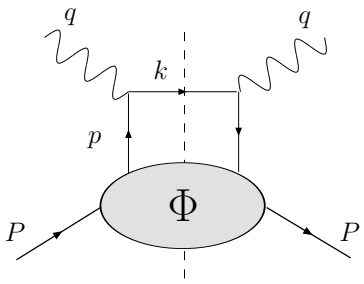

Figure 2.7: Handbag diagram. The virtual photon with 4-momentum q strikes a quark inside the nucleon with momentum p.

part. In order to describe the soft part, we introduce a function, the so-called quark-quark correlation function Φ ,

$$\begin{aligned} \Phi_{ij}(p,P,S) &= \sum_X \int \frac{d^3\boldsymbol{P}_X}{(2\pi)^3 2E_X}(2\pi)^4\delta^4(P-p-P_X) \\ &\times \langle PS|\bar{\psi}_j(0)|X\rangle\langle X|\psi_i(0)|PS\rangle \end{aligned} \tag{2.39}$$

At leading order of $1/Q$, the correlation function contains all the relevant information on the non-perturbative dynamics of quarks inside the nucleon.

Because of its non-perturbative nature, it was not possible to calculate it from the first principle. Lattice QCD calculation is a new challenge to this problem. At the moment, experiment is the only way to investigate it.

Using this quark-quark correlation function, we can rewrite the hadronic tensor with a quark field between the nucleon and its remnant $\phi_i(p,P,S) = \langle X|\psi_i(0)|PS\rangle$

$$\begin{aligned} W^{\mu\nu}(q,P,S) &= \sum_q e_q^2 \int \frac{d^4p}{(2\pi)^4}\delta\left((p+q)^2 - m_q^2\right) \\ &\times \mathrm{Tr}\left[\Phi(p,P,S)\gamma^\mu(\not{p}+\not{q}+m_q)\gamma^\nu + \bar{\Phi}(p,P,S)\gamma^\nu(\not{p}+\not{q}-m_q)\gamma^\mu\right] \end{aligned} \quad (2.40)$$

where Fourier transformation of Dirac delta function and the completeness of the $|X\rangle$ are used. $\bar{\Phi}$ is the correlation function of anti-quark which is obtained from Eq. (2.39) by interchanging ψ with $\bar{\psi}$.

2.3.2 Parton Distribution Functions

The quark-quark correlation function gives quark level information of the nucleon. The information is expressed in terms of the parton distribution functions (PDF).

Here we consider the nucleon momentum in light-cone coordinate system $P = (P^+, P^-, \boldsymbol{P}_T = \boldsymbol{0})$ where $P^\pm = (P^0 \pm P^3)/\sqrt{2}$, and we chose the light-cone momentum P^+. Accordingly, the quark momentum is expressed as $p = (p^+, p^-, \boldsymbol{p}_T)$. The PDF is derived from the quark-quark correlation function and is obtained by integrating Φ over the rest components of quark momentum, p^- and $\boldsymbol{p}_T$. Thus the integrated Φ is a function of the light-cone momentum p^+. If we choose the infinite momentum frame, the transverse component of the momentum $|\boldsymbol{p}_T|$ is small enough in comparison with the nucleon momentum P^+. Then one can write $p^+ \simeq xP^+$. The resulting integrated Φ depends only on the light-cone momentum fraction $x = p^+/P^+$ and S,

$$\int dp^-\ d^2\boldsymbol{p}_T\ \Phi_{ij}(p,P,S)\Big|_{p^+=xP^+} = \Phi_{ij}(x,S) \quad (2.41)$$

It is useful to introduce the *projected* correlation function $\Phi^{[\Gamma]}$ which is defined as

$$\Phi^{[\Gamma]}(x) \equiv \frac{1}{2}\int dp^-\ d^2\boldsymbol{p}_T\ \mathrm{Tr}(\Phi(p,P,S)\ \Gamma) \quad (2.42)$$

where Γ is a 4×4 Dirac matrix. The projection Γ determines the characteristic of the quark current J^q,

$$J^q = \frac{1}{2}\bar{\psi}\Gamma\psi. \quad (2.43)$$

For example, vector and axial currents are expressed as

$$\begin{aligned} \text{Vector current}: \quad & J_v^q = \tfrac{1}{2}\bar{\psi}\gamma^+\bar{\psi}, \\ \text{Axial current}: \quad & J_a^q = \tfrac{1}{2}\bar{\psi}\gamma^+\gamma^5\psi. \end{aligned} \tag{2.44}$$

PDF's are defined using the projected Φ. In case of the vector current, the projection $\Gamma = \gamma^+$ gives the spin-independent parton distribution function f_1,

$$\Phi^{[\gamma^+]}(x) = f_1(x) \tag{2.45}$$

The spin-independent structure function F_1 is reconstructed as the sum of the f_1 for possible quarks q and anti-quarks $\bar{q}$,

$$F_2(x) = 2xF_1(x) = \sum_{q/\bar{q}} e_q^2 \; f_1^q(x). \tag{2.46}$$

Similarly, we obtain the structure function g_1 using the quark helicity distribution[1] Δq which is obtained choosing the projection $\Gamma = \gamma^+\gamma^5$,

$$\Phi^{[\gamma^+\gamma^5]}(x) = \Delta q(x), \tag{2.47}$$

$$g_1(x) = \frac{1}{2}\sum_q e_q^2 \; \Delta q(x). \tag{2.48}$$

In addition to above two PDFs, there is the third quark distribution function so-called *transversity* distribution denoted as h_1. The transversity distribution is obtained from the projection $\Gamma = i\sigma^{i+}\gamma^5 = \gamma^+\gamma^1\gamma^5$

$$\Phi^{[i\sigma^{i+}\gamma^5]}(x) = h_1(x). \tag{2.49}$$

Sum of the transversity distribution corresponds to the 'tensor-charge' of the nucleon. In Fig. 2.8, an interpretation of respective PDFs is shown. As shown in Fig. 2.8, the helicity distribution Δq represents longitudinally polarized quarks inside a longitudinally polarized nucleon. The transversity h_1 describes transversely polarized quarks inside a transversely polarized nucleon. Thus both PDFs describes quark polarization regarding to the nucleon spin direction. It is expected that both PDFs are consistent, $\Delta q = h_1$ in the

[1]Historically the quark helicity distribution has been expressed as Δq. But from recent studies of nucleon structure, the number of the different quark distributions has increased. So the symbol g_1 is frequently used for the quark helicity distribution.

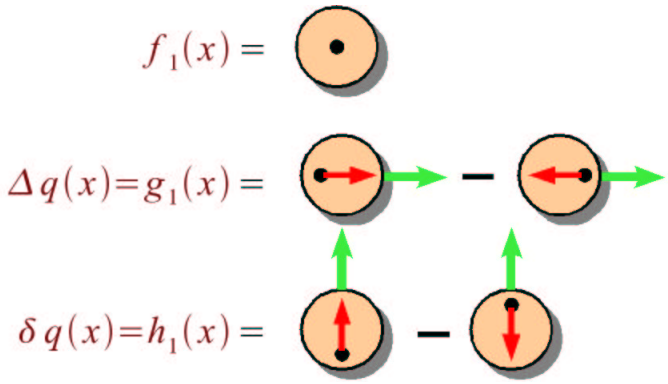

Figure 2.8: Probabilistic interpretation of leading order integrated PDFs.

non-relativistic region, but they can be different in the relativistic limit, e.g. at high energy interaction. Therefore the transversity distribution allows us to learn more about the relativistic nature of quarks inside the nucleon.

At leading twist[2], these three distributions are the all which can be obtained from the integrated correlation function.

2.3.3 Transverse Momentum Dependent PDFs

As seen in the previous section, the PDFs are obtained by projections of the integrated quark-quark correlation function Eq. (2.41). At leading twist, the quark distribution functions which can be obtained from the integrated correlation function were presented. But if we take into account the transverse momentum appearing in Eq. (2.41) in the hard processes, other quark distributions can be defined. In this case, new distributions which are also functions of p_T are introduced. For example, the spin-independent quark distribution function f_1 defined in Eq. (2.45) is

$$f_1(x) = \int d^2\boldsymbol{p}_T \; f_1(x, \boldsymbol{p}_T^2) \tag{2.50}$$

The transverse momentum dependent PDF itself is not very new, because as we saw in Eq. (2.41) the transverse component appears naturally. But

[2] The operator product expansion technique offers a simple representation of the nucleon structure in terms of so-called twists. Twists are $1/Q$ power terms in the Taylor expansion of the hadronic tensor. The first term, twist-2 or leading twist, contains information on individual parton distributions. This term expresses the asymptotic freedom of the nucleon constituents. The higher twist terms imply an interaction among partons inside the nucleon. [41, 42] Normally, the higher twist terms, for example twist-2 terms, are suppressed by power of $1/Q$.

historically it had been thought that the transverse momentum is irrelevant in describing the hard processes. However in order to describe the observed single spin asymmetries, the transverse momenta are needed. In particular, correlations between the nucleon spin and the transverse momenta p_T and k_T are the key properties to understand the single spin asymmetries.

The p_T dependent PDF is defined using projections of the un-integrated correlation function. This projected correlation function is defined as

$$\Phi^{[\Gamma]}(x, \boldsymbol{p}_T) \equiv \frac{1}{2} \int dp^- \ \mathrm{Tr}(\Phi(p, P, S)\ \Gamma). \tag{2.51}$$

Using this projected correlation function, the PDFs given in the previous section are rewritten at leading order in $1/Q$ [43],

$$\begin{aligned}
\Phi^{[\gamma^+]}(x, \boldsymbol{p}_T) &= f_1(x, \boldsymbol{p}_T^2) + \frac{\varepsilon_T^{ij} p_{Ti} S_{Tj}}{M_N}\ f_{1T}^{\perp}(x, \boldsymbol{p}_T^2) && (2.52)\\
\Phi^{[\gamma^+\gamma^5]}(x, \boldsymbol{p}_T) &= \lambda g_{1L}(x, \boldsymbol{p}_T^2) + \frac{\boldsymbol{p}_T \cdot \boldsymbol{S}_T}{M_N} g_{1T}(x, \boldsymbol{p}_T^2) && (2.53)\\
\Phi^{[i\sigma^{i+}\gamma^5]}(x, \boldsymbol{p}_T) &= S_T^i h_{1T}(x, \boldsymbol{p}_T^2) + \frac{p_T^i}{M_N}\left(\lambda h_{1L}^{\perp}(x, \boldsymbol{p}_T^2) + \frac{\boldsymbol{p}_T \cdot \boldsymbol{S}_T}{M_N} h_{1T}^{\perp}(x, \boldsymbol{p}_T^2)\right) \\
&\quad + \frac{\varepsilon_T^{ij} p_T^j}{M_N} h_{1\perp}(x, \boldsymbol{p}_T^2). && (2.54)
\end{aligned}$$

where $f_{1T}^{\perp}$ is the Sivers function. In Fig. 2.9, probabilistic interpretations for the above PDFs are illustrated. The Sivers function $f_{1T}^{\perp}$ describes the unpolarized quark inside a transversely polarized nucleon. This function has a nature of (naive) time-reversal odd (T-odd). Because of this T-odd nature, the Sivers function can generate the single spin asymmetries. We will see a detailed account for the Sivers function in next chapter.

The PDFs introduced in the previous section, the helicity distribution Δq (Eq. (2.48)) and transversity h_1 (Eq. (2.49)), are rewritten as [43],

$$\begin{aligned}
\Delta q(x, \boldsymbol{p}_T^2) &= g_{1L}(x, \boldsymbol{p}_T^2) && (2.55)\\
h_1(x, \boldsymbol{p}_T^2) &= h_{1T}(x, \boldsymbol{p}_T^2) + \frac{\boldsymbol{p}_T^2}{2M_N} h_{1T}^{\perp}(x, \boldsymbol{p}_T^2) && (2.56)
\end{aligned}$$

It should be noted that the transversity h_1 can be expressed as a function of transverse momentum as in above. However as we already saw in the previous section the transversity represents the transverse polarization of quark inside the transversely polarized nucleon. Therefore, even if no transverse momentum $p_T = 0$, the transversity itself can be non-zero, as helicity distribution Δq is so.

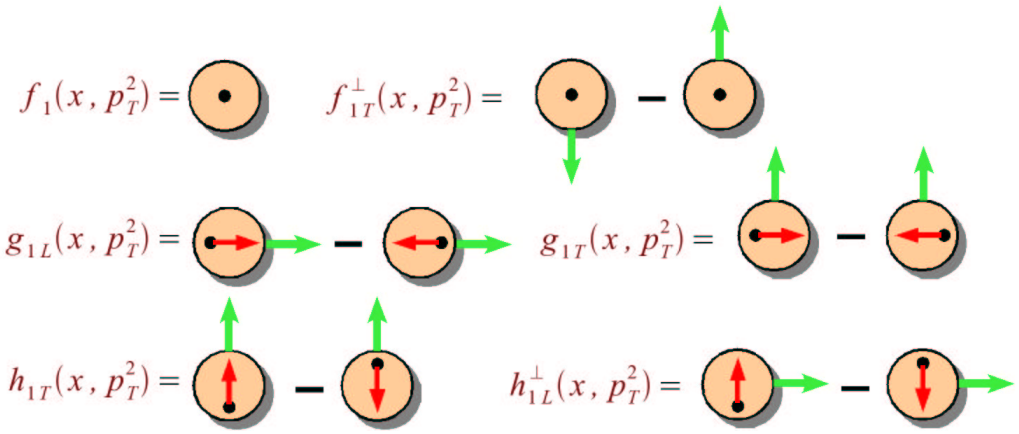

Figure 2.9: Probabilistic interpretation of leading order transverse momentum dependent PDFs. Large circle indicates nucleon and arrow on the circle denotes the nucleon spin direction. The small circle inside the nucleon indicates the quark, and arrow on them denotes the quark spin direction.

These transverse momentum dependent PDFs can be classified with the nucleon polarization state. The quark-quark correlation function is expressed by separating the terms corresponding to unpolarized (O), longitudinally (L) and transversely (T) polarized target [43],

$$\Phi_O(x, \boldsymbol{p}_T)\gamma^+ = \left\{ f_1(x, \boldsymbol{p}_T^2) + i h_1^{\perp}(x, \boldsymbol{p}_T^2) \frac{\not{p}_T}{M} \right\} P_+ \tag{2.57}$$

$$\Phi_L(x, \boldsymbol{p}_T)\gamma^+ = \left\{ \lambda \Delta q(x, \boldsymbol{p}_T^2)\gamma_5 + \lambda h_{1L}^{\perp}(x, \boldsymbol{p}_T^2)\gamma_5 \frac{\not{p}_T}{M} \right\} P_+ \tag{2.58}$$

$$\begin{aligned} \Phi_T(x, \boldsymbol{p}_T)\gamma^+ = & \left\{ f_{1T}^{\perp}(x, \boldsymbol{p}_T^2) \frac{\varepsilon_{T\rho\sigma} p_T^{\sigma} S_T^{\sigma}}{M} + g_{1T}(x, \boldsymbol{p}_T^2) \frac{\boldsymbol{p}_T \cdot S_T}{M} \gamma_5 \right. \\ & \left. + h_{1T}(x, \boldsymbol{p}_T^2)\gamma_5 \not{S}_T + h_{1T}^{\perp}(x, \boldsymbol{p}_T^2) \frac{\boldsymbol{p}_T \cdot S_T}{M} \gamma_5 \frac{\gamma_5 \not{p}_T}{M} \gamma_5 \right\} P_+ \end{aligned} \tag{2.59}$$

where the sum of these correlation functions gives the full (spin) structure of the nucleon,

$$\Phi(x, \boldsymbol{p}_T) = \Phi_O(x, \boldsymbol{p}_T) + \Phi_L(x, \boldsymbol{p}_T) + \Phi_T(x, \boldsymbol{p}_T). \tag{2.60}$$

In order to access the Sivers function, DIS measurement with transversely polarized target is required. However the transverse spin is naturally suppressed in high energy interaction since the transverse component of the spin

is no longer eigenstate of transverse spin operator. Moreover it is expected that transverse momentum p_T is very small compared to the nucleon momentum P^+. As the results, the transverse momentum related mechanisms, such as Sivers effect, is suppressed with power of $1/P^+$. Therefore the inclusive measurement does not help to access to the above transverse momentum dependent PDFs.

2.4 Semi-Inclusive Deep Inelastic Scattering

In semi-inclusive measurements, a produced hadron in the final state is also detected in coincidence of the scattered lepton. Fig. 2.10 shows a schematic

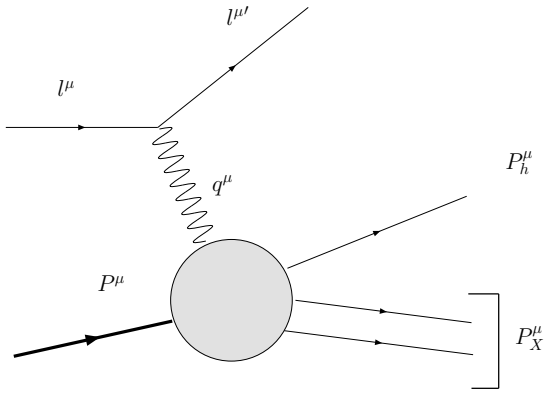

Figure 2.10: Diagram of a deep inelastic scattering.

diagram of a semi-inclusive measurement. The produced hadrons can carry information on the flavor of the struck quark.

The semi-inclusive measurement allows us to access the transverse momentum dependent PDFs in DIS experiment. The quark parton model will be extended by a fragmentation model which allows to relate the appearance of certain hadrons h in the final state to the parton distribution functions for different flavors by so-called "fragmentation functions" (FFs). Figure 2.11 presents the handbag diagram of semi-inclusive measurement. The quark fragmentation functions are derived from the quark-decay functions Δ [44], which is also matrix elements of hadronic tensor.

Before the discussion of the decay function, the kinematic variables of semi-inclusive measurements are introduced. There are important kinematic

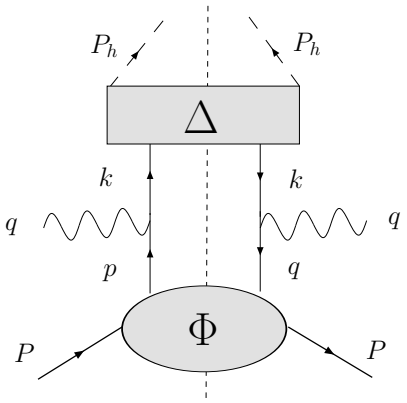

Figure 2.11: Handbag diagram of semi-inclusive DIS measurement.

variables,

$$\begin{array}{ll} z = \dfrac{P \cdot P_h}{P \cdot q} \overset{\text{Lab}}{=} \dfrac{E_h}{\nu} & \text{Fractional energy of a hadron in lab. frame} \\ |\boldsymbol{P}_{h\perp}| = \dfrac{|\boldsymbol{q} \times \boldsymbol{P}_h|}{|\boldsymbol{q}|} & \text{Transverse momentum of hadron in } \gamma^* N \text{ frame} \end{array} \tag{2.61}$$

where E_h and $\boldsymbol{P}_h$ are the energy and 3-momentum of hadron, and $\boldsymbol{q}$ indicates the virtual photon 3-momentum.

2.4.1 Fragmentation Function

The hadron tensor as in Eq. (2.40) is expanded with decay function Δ [36, 45],

$$\begin{aligned} W_{\mu\nu}(q, P, P_h) &= \sum_q e_q^2 \int \frac{d^4p}{(2\pi)^4} \frac{d^4k}{(2\pi)^4}\, \delta^{(4)}(p+q-k) \mathrm{Tr}\left(\Phi(p, S, P)\gamma^\mu \Delta(k, P_h)\gamma^\nu\right) \\ &= \sum_q e_q^2 \int \frac{d^2\boldsymbol{p}_T}{(2\pi)^4} \frac{d^2\boldsymbol{k}_T}{(2\pi)^4} \delta^2(\boldsymbol{p}_T - \frac{\boldsymbol{P}_{h\perp}}{z} - \boldsymbol{k}_T) \\ &\quad \times \mathrm{Tr}\left(\Phi(x, \boldsymbol{p}_T)\gamma_\mu \Delta(z, \boldsymbol{k}_T)\gamma_\nu\right) \end{aligned} \tag{2.62}$$

where the delta function requires transverse momentum conservation, k_T is the transverse momentum of the quark which is defined in Fig. 2.5. The decay-function is defied as [36],

$$\Delta(z, \boldsymbol{k}_T) = \sum_X \int d\xi^+ d^2\boldsymbol{\xi}_T e^{ik\cdot\xi} \langle 0|\psi(\xi)|X; P_h, S\rangle\langle X; P_h, S|\bar{\psi}(0)|0\rangle \tag{2.63}$$

where $z = P_h^-/k^-$ is the light-cone momentum fraction of the produced hadron. In the hadron-nucleon collinear system, the hadron moves to opposite direction to the nucleon, thus the P_h^- component is dominant. The decay-function describes the probabilities that the struck quark fragments into a hadronic state $|X; P_h, S\rangle$.

Adopting the similar procedure to that of the parton distribution function, the decay function can be decomposed with $\boldsymbol{k}_T$-dependent fragmentation functions [36],

$$\begin{aligned}\Delta(z,\boldsymbol{k}_T) &= \frac{1}{2}\Bigg\{ D_1(z,\boldsymbol{k}_T)\not{n}_- + D_{1T}^{\perp}(z,\boldsymbol{k}_T)\frac{\varepsilon_{\mu\nu\rho\sigma}\gamma^\mu n_-^\nu k_T^\rho S_{hT}^\sigma}{M_h} + G_{1s}(z,\boldsymbol{k}_T)\gamma_5\not{n}_- \\ &\quad + H_{1T}(z,\boldsymbol{k}_T)i\sigma_{\mu\nu}\gamma_5 n_-^\mu S_{hT}^\nu + H_{1s}^{\perp}(z,\boldsymbol{k}_T)\frac{i\sigma_{\mu\nu}\gamma_5 n_-^\nu k_T^\nu}{M_h} \\ &\quad + H_1^{\perp}(z,\boldsymbol{k}_T)\frac{i\sigma_{\mu\nu}\gamma_5 n_-^\nu k_T^\nu}{M_h}\Bigg\} \end{aligned} \tag{2.64}$$

For example, spin-independent fragmentation function D_1 is given by integrating over $\boldsymbol{k}_T$,

$$D_1(z) = z^2 \int d^2\boldsymbol{k}_T \; D_1(z, z^2\boldsymbol{k}_T^2). \tag{2.65}$$

2.4.2 Cross Section of Semi-Inclusive DIS

For the study of the Sivers and Collins functions, the present work uses a transversely polarized target. The cross section measured with a transversely polarized target $d\sigma^\uparrow$ can be written as follows,

$$d\sigma^\uparrow = d\sigma_{UU} + |\boldsymbol{S}_T| d\sigma_{UT} + |\boldsymbol{S}_L| d\sigma_{UL}. \tag{2.66}$$

where S_T and S_L are the transverse and the longitudinal spin component of the nucleon spin. The subscripts U (Unpolarized), T (Transverse), L (Longitudinal) represent beam and target polarization. The first subscript is for the beam, the second is for target. For example σ_{UT} is the cross section of DIS of unpolarized beam and transversely polarized target. The measured cross section involves not only the transverse spin component but also unpolarized and longitudinal spin component, since the target polarization is defined with respect to beam direction (not to virtual photon direction).

Each term of the cross section can be computed using the leptonic and hadronic tensors. In leading twist, the cross sections are expressed in terms

of PDF and FF as follows [45],

$$d\sigma_{UU} \propto \Bigg\{ A(y) \sum_q e_q^2 \mathcal{I}\left[f_1^q(x, \boldsymbol{p}_T^2) D_1^q(z, z^2 \boldsymbol{k}_T^2) \right] \\ -B(y)\cos(2\phi) \sum_q e_q^2 \mathcal{I}\left[h_1^{\perp q}(x, \boldsymbol{p}_T^2) H_1^{\perp q}(z, z^2 \boldsymbol{k}_T^2) \right] \Bigg\}, \tag{2.67}$$

$$d\sigma_{UL} \propto -B(y) \sum_q e_q^2 B(y)\sin(2\phi) \sum_q e_q^2 \mathcal{I}\left[h_{1L}^{\perp q}(x, \boldsymbol{p}_T^2 H_1^{\perp q}(z, z^2 \boldsymbol{k}_T^2)) \right], \tag{2.68}$$

$$d\sigma_{UT} \propto \Bigg\{ -B(y)\sin(\phi + \phi_S) \sum_q e_q^2 \mathcal{I}\left[h_1^q(x, \boldsymbol{p}_T^2) H_1^{\perp q}(z, z^2 \boldsymbol{k}_T^2) \right] \\ -A(y)\sin(\phi - \phi_S) \mathcal{I}\left[f_{1T}^{\perp q}(x, \boldsymbol{p}_T^2) D_1^q(z, z^2 \boldsymbol{k}_T^2) \right] \\ -B(y)\sin(2\phi - \phi_S) \sum_q e_q^2 \mathcal{I}\left[h_{1T}^{\perp q}(x, \boldsymbol{p}_T^2) H_1^{\perp q}(z, z^2 \boldsymbol{k}_T^2) \right] \Bigg\}, \tag{2.69}$$

$$A(y) \equiv (1 - y + \frac{y^2}{2}),\ B(y) \equiv (1 - y),$$

where ϕ and ϕ_S are the azimuthal angles which are defined in Fig. 2.2, $\mathcal{I}\left[\cdots \right]$ indicates a convolution integral of p_T and k_T which will be explained later.

It has to be noted that the azimuthal angles themselves depend on coordinate system, but of course the physics does not depend on the system. Historically, different coordinate systems were sometimes adopted, which has opposite z-axis (and also y-axis) comparing to Fig. 2.2 since in theoretical discussion it is normally defined so that the target proton moves to positive z-direction, just for convenience. The resulting coordinate system has azimuthal angle with opposite sign. In this thesis, the coordinate system shown in Fig. 2.2 is used according to [46].

As shown in Eq. (2.67) to Eq. (2.69), except the usual spin-independent cross section, all terms are expressed with sine- or cosine-terms with different combination of the azimuthal angles. Those are expressed with a Fourier expansion. Thus they are naturally orthogonal functions and can be disentangled without interference between the terms.

A complete explanation of each PDF and FF lies outside of the scope of this thesis. Only some of them which are related to the present experiment will be explained in the next chapter.

Chapter 3

Cross Section and Sivers Function

In this chapter, specific formalism to access the Sivers function in deep inelastic scattering with transversely polarized target and unpolarized beam. Together with the Sivers function, Collins function, transversity and related functions are also discussed. Some interpretations of the Sivers mechanism (function) and its connection to quark orbital angular momentum are discussed. In the last section of this chapter, theoretical predictions of the Sivers function are introduced.

3.1 Convolution Integral

The transverse component of the differential cross section $d\sigma_{UT}$ can be written as a Fourier expansion of respective azimuthal angle dependences. At leading twist, the cross section is written as follows,

$$\begin{aligned} d\sigma_{UT}(\phi, \phi_S) &= d\sigma_{\mathcal{S}} \cdot \sin(\phi - \phi_S) \\ &+ d\sigma_{\mathcal{C}} \cdot \sin(\phi + \phi_S) \\ &+ d\sigma_{\mathcal{O}1} \cdot \sin(3\phi - \phi_S) \end{aligned}$$

where $d\sigma_{\mathcal{S}}$, $d\sigma_{\mathcal{C}}$ and $d\sigma_{\mathcal{O}1}$ involve several parton distribution and fragmentation functions as described in the previous chapter (see Eq. (2.69)). Each term is related to these functions as following [35, 36]:

$$\begin{aligned} d\sigma_{\mathcal{S}} &\sim f_{1T}^{\perp} \; D_1 \\ d\sigma_{\mathcal{C}} &\sim h_1 \; H_1^{\perp} \\ d\sigma_{\mathcal{O}1} &\sim h_{1T}^{\perp} H_1^{\perp} \end{aligned} \tag{3.1}$$

In this analysis, we are not concerned with the $d\sigma_{\mathcal{O}1}$ term. We focus on 'Sivers' and 'Collins' type cross sections $d\sigma_{\mathcal{S}}$ and $d\sigma_{\mathcal{C}}$. In principle, $d\sigma_{\mathcal{S}}$, $d\sigma_{\mathcal{C}}$ and $d\sigma_{\mathcal{O}1}$ can be extracted from $d\sigma^{\uparrow}$ separately (no cross-talk), since the sine modulations of the azimuthal angles are expressed as a Fourier expansion.

Each differential cross section $d\sigma_{\mathcal{S}}$ and $d\sigma_{\mathcal{C}}$ can be expressed in terms of quark distribution and fragmentation functions [35, 36]:

$$d\sigma_{\mathcal{S}} \equiv \frac{d^6\sigma_{\mathcal{S}}}{dx\ dy\ dz\ d\phi_S\ d^2\boldsymbol{P_{h\perp}}} = -\frac{2\alpha^2}{sxy^2}A(y)\sum_q e_q^2\ \mathcal{I}\left[\left(\frac{\boldsymbol{p_T}\cdot\hat{\boldsymbol{P}}_{\boldsymbol{h}\perp}}{M_N}\right)\ f_{1T}^{\perp q}D_1^q\right], \quad (3.2)$$

$$d\sigma_{\mathcal{C}} \equiv \frac{d^6\sigma_{\mathcal{C}}}{dx\ dy\ dz\ d\phi_S\ d^2\boldsymbol{P_{h\perp}}} = -\frac{2\alpha^2}{sxy^2}B(y)\sum_q e_q^2\ \mathcal{I}\left[\left(\frac{\boldsymbol{k_T}\cdot\hat{\boldsymbol{P}}_{\boldsymbol{h}\perp}}{M_h}\right)\ h_1^q H_1^{\perp q}\right], \quad (3.3)$$

$$\hat{\boldsymbol{P}}_{\boldsymbol{h}\perp} \equiv \frac{\boldsymbol{P_{h\perp}}}{|\boldsymbol{P}_{h\perp}|},$$

where M_N and M_h are the masses of the nucleon and produced hadron, $\boldsymbol{p}_T$ and $\boldsymbol{k}_T$ are the quark intrinsic and fragmentation transverse momentum, $\mathcal{I}\big[\cdots\big]$ is a convolution integral on $\boldsymbol{p}_T$ and $\boldsymbol{k}_T$ defined as,

$$\mathcal{I}\Big[\mathcal{M}\ f^q\ D^q\Big] \equiv \int d^2\boldsymbol{p_T}d^2\boldsymbol{k_T}\ \delta^{(2)}\left(\boldsymbol{p_T}-\frac{\boldsymbol{P_{h\perp}}}{z}-\boldsymbol{k_T}\right)\Big[\mathcal{M}\ f^q(x,\boldsymbol{p_T})\ D^q(z,\boldsymbol{k_T})\Big], \quad (3.4)$$

where $\mathcal{M}$ is a function of transverse momenta, which depends on the involved distribution and fragmentation functions.

In addition to the polarized cross section, we need the unpolarized cross section expressed as,

$$d\sigma_{UU} \equiv \frac{d^6\sigma_{UU}}{dx\ dy\ dz\ d\phi_S\ d^2\boldsymbol{P_{h\perp}}} = \frac{2\alpha^2}{sxy^2}A(y)\sum_q e_q^2\ \left\{\mathcal{I}\Big[f_1^q D_1^q\Big] - B(y)\ \cos(2\phi)\mathcal{I}\left[\frac{2(\boldsymbol{p}_T\cdot\hat{\boldsymbol{P}}_{h\perp})(\boldsymbol{k}_T\cdot\hat{\boldsymbol{P}}_{h\perp})}{M_N M_h}h_1^{\perp,q}H_1^{\perp,q}\right]\right\}, \quad (3.5)$$

The unpolarized cross section Eq. (3.5) also involves an azimuthal dependence. This is discussed e.g. in references [35, 36]. In this chapter, we will neglect the possible $\cos(2\phi)$ term to present a basic formalism accessing the Sivers and Collins effects.

3.1.1 Deconvolution of PDFs and FFs

The Sivers function $f_{1T}^{\perp}$, the transversity h_1, the Collins fragmentation function $H_1^{\perp}$ and spin-independent fragmentation function D_1 are defined as fol-

lows,

$$f_{1T}^{\perp}(x) = \int d^2\boldsymbol{p_T} f_{1T}^{\perp}(x, \boldsymbol{p_T}^2) \tag{3.6}$$

$$h_1(x) = \int d^2\boldsymbol{p_T} h_1(x, \boldsymbol{p_T}^2) \tag{3.7}$$

$$H_1^{\perp}(z) = z^2 \int d^2\boldsymbol{k_T} H_1^{\perp}(z, z^2\boldsymbol{k_T}^2) \tag{3.8}$$

$$D_1(z) = z^2 \int d^2\boldsymbol{k_T} D_1(z, z^2\boldsymbol{k_T}^2) \tag{3.9}$$

The cross sections $d\sigma_{\mathcal{S}/\mathcal{C}}$ involve the convolution integral over the transverse momenta, $\boldsymbol{p}_T$ and $\boldsymbol{k}_T$ as defined in Eq. (3.4). This convolution integral connects the involved transverse momenta, and the delta-function $\delta^{(2)}(\boldsymbol{p_T} - \boldsymbol{P}_{h\perp}/z - \boldsymbol{k_T})$ ensures conservation of transverse momenta. Because of the convolution, in general, the PDF $f(x, \boldsymbol{p}_T^2)$ and FF $D(z, z^2\boldsymbol{k}_T^2)$ are no longer independent functions in the cross sections.

In order to resolve the convolutions in Eqs. (3.2) and (3.3), i.e. in order to obtain $f_{1T}^{\perp}(x)$, $h_1(x)$ and $H_1^{\perp}(z)$ in a factorized way, one needs to weight the cross section [36]. Here, we introduce *weight function* $\mathcal{W}$ which is defined as follows,

$$\mathcal{W} = \begin{cases} \dfrac{|\boldsymbol{P}_{h\perp}|}{M_N} & : \text{Sivers} \\ \dfrac{|\boldsymbol{P}_{h\perp}|}{M_h} & : \text{Collins} \end{cases} \tag{3.10}$$

Using these weight functions, one can obtain a deconvoluted expression of the cross section after integration over $P_{h\perp}$. For example the *weighted* Sivers type cross section[1], is expressed from Eq. (3.2)

$$\begin{aligned} &\int d^2\boldsymbol{P_{h\perp}} \left(\left[\frac{|\boldsymbol{P}_{h\perp}|}{M_N} \right] \cdot d\sigma_{\mathcal{S}} \right) \\ &\quad = -\frac{2\alpha^2}{sxy^2} A(y) \sum_q e_q^2 \int d^2\boldsymbol{p_T}\; d^2\boldsymbol{k_T}\; d^2\boldsymbol{P_{h\perp}}\; \delta^{(2)} \left(\boldsymbol{p_T} - \frac{\boldsymbol{P_{h\perp}}}{z} - \boldsymbol{k_T} \right) \left(\frac{\boldsymbol{p_T} \cdot \hat{\boldsymbol{P}}_{h\perp}}{M_N} \right) \\ &\qquad \times \left[\frac{|\boldsymbol{P}_{h\perp}|}{M_N} \right] \cdot f_{1T}^{\perp q}(x, \boldsymbol{p_T^2}) D_1^q(z, z^2\boldsymbol{k_T}^2) \\ &\quad = -\frac{2\alpha^2}{sxy^2} A(y) \sum_q e_q^2 z f_{1T}^{\perp(1)q}(x) D_1^q(z) \end{aligned} \tag{3.11}$$

[1] see details in Appendix A

$$\int d^2\boldsymbol{P_{h\perp}}\; d\sigma_{UU}$$
$$= \frac{2\alpha^2}{sxy^2}B(y)\sum_q e_q^2 \int d^2\boldsymbol{p_T}\; d^2\boldsymbol{k_T}\; d^2\boldsymbol{P_{h\perp}}\delta^{(2)}\left(\boldsymbol{p_T} - \frac{\boldsymbol{P_{h\perp}}}{z} - \boldsymbol{k_T}\right)$$
$$\times f_1(x, \boldsymbol{p_T^2}) D_1(z, z^2 \boldsymbol{k_T}^2)$$
$$= \frac{2\alpha^2}{sxy^2}B(y)\sum_q e_q^2 f_1^q(x) D_1^q(z) \tag{3.12}$$

where $f_{1T}^{\perp(1)}$ is the transverse momentum squared moment of the Sivers function which is defined as

$$f_{1T}^{\perp(1)}(x) \equiv \int d^2\boldsymbol{p}_T \left(\frac{\boldsymbol{p}_T^2}{2M_N^2}\right) f_{1T}^{\perp}(x, \boldsymbol{p}_T^2). \tag{3.13}$$

In the same manner, the moment of the Collins function is introduced

$$H_1^{\perp(1)}(z) \equiv z^2 \int d^2\boldsymbol{k_T} \left(\frac{\boldsymbol{k_T}^2}{2M_h^2}\right) H_1^{\perp}(z, z^2\boldsymbol{k_T}^2) \tag{3.14}$$

and the deconvoluted Collins parton model expression can be obtained by weighting the cross section according to Eq. (3.10).

$$\int d^2\boldsymbol{P_{h\perp}} \left(\left[\frac{|\boldsymbol{P}_{h\perp}|}{M_h}\right] \cdot d\sigma_{\mathcal{C}}\right) = -\frac{2\alpha^2}{sxy^2}A(y)\sum_q e_q^2 z h_1^q(x) H_1^{\perp(1)q}(z) \tag{3.15}$$

It is worth while to point out that the weighted cross section of $d\sigma_{\mathcal{S}/\mathcal{C}}$ has extra z-factor likes

$$d\sigma_{\mathcal{S}/\mathcal{C}} \propto \sum_q e_q^2\; z\; f^q(x)\; D(z).$$

3.1.2 Resolving the Convolution without Weighting

In addition to what we had discussed in the previous section, there are two special cases in which the convolution is naturally resolved without any additional factors. For this discussion, it is useful to introduce another moment of the transverse momentum dependent PDF and FF,

$$f_{1T}^{\perp(1/2)}(x) \equiv \int d^2\boldsymbol{p}_T \left(\frac{\boldsymbol{p}_T}{2M_N}\right) f_{1T}^{\perp}(x, \boldsymbol{p}_T^2). \tag{3.16}$$

$$H_1^{\perp(1/2)}(z) \equiv z^2 \int d^2\boldsymbol{k_T} \left(\frac{\boldsymbol{k_T}}{2M_h}\right) H_1^{\perp}(z, z^2\boldsymbol{k_T}^2) \tag{3.17}$$

1. **No intrinsic transverse momentum ($p_T = 0$)**
This gives the simplest expression with a delta-function of the intrinsic transverse momentum $\boldsymbol{p}_T$,

$$f^q(x, \boldsymbol{p}_T^2) \propto f^q(x)\delta\left(\boldsymbol{p}_T^2\right), \tag{3.18}$$

for generic PDFs. In this case, the transverse momentum conservation $\delta^{(2)}(\boldsymbol{p}_T - \boldsymbol{P}_{h\perp}/z - \boldsymbol{k}_T)$ gives $\boldsymbol{P}_{h\perp} = -z\boldsymbol{k}_T$, therefore

$$\hat{\boldsymbol{P}}_{h\perp} \equiv \frac{\boldsymbol{P}_{h\perp}}{|\boldsymbol{P}_{h\perp}|} = \frac{-z\boldsymbol{k}_T}{|-z\boldsymbol{k}_T|}. \tag{3.19}$$

The parton distribution and fragmentation functions are no longer convoluted. The unweighted cross sections are written as,

$$\begin{aligned}\int d^2\boldsymbol{P}_{h\perp}\, d\sigma_{\mathcal{S}} &\propto -\sum_q e_q^2\, \mathcal{I}\left[\left(\frac{\boldsymbol{p_T}\cdot\hat{\boldsymbol{P}}_{\boldsymbol{h}\perp}}{M_N}\right)\cdot f_{1T}^{\perp,q} D_1^q\right] \\ &= 0. \end{aligned} \tag{3.20}$$

$$\begin{aligned}\int d^2\boldsymbol{P}_{h\perp}\, d\sigma_{\mathcal{C}} &\propto -\sum_q e_q^2\, \mathcal{I}\left[\left(\frac{\boldsymbol{k_T}\cdot\hat{\boldsymbol{P}}_{\boldsymbol{h}\perp}}{M_h}\right)\cdot h_1^q H_1^{\perp q}\right] \\ &\propto \sum_q e_q^2\, h_1^q(x) H_1^{\perp(1/2)q}(z), \end{aligned} \tag{3.21}$$

The Sivers type cross section vanishes, but the Collins type survives as the transversity distribution h_1 can be non-zero even in case of no intrinsic transverse momenta ($p_T = 0$).

2. **Gaussian transverse momentum distribution**
If the intrinsic transverse momentum is non-zero, and both $\boldsymbol{p}_T$ and $\boldsymbol{k}_T$ follow a Gaussian distribution, the PDF and FF can be written like,

$$f^q(x, \boldsymbol{p}_T^2) = f^q(x)\frac{\exp\left(-\boldsymbol{p}_T^2/\langle\boldsymbol{p}_T^2\rangle\right)}{\pi\langle\boldsymbol{p}_T^2\rangle}, \tag{3.22}$$

$$D^q(z, z^2\boldsymbol{k}_T^2) = D^q(z)\frac{\exp\left(-z^2\boldsymbol{k}_T^2/\langle z^2\boldsymbol{k}_T^2\rangle\right)}{\pi\langle z^2\boldsymbol{k}_T^2\rangle}. \tag{3.23}$$

In this case, the x and z dependence of the PDF's and FF's is separated from the transverse momentum dependence, therefore they do not affect the integration over transverse momenta, $\boldsymbol{p}_T$, $\boldsymbol{k}_T$. The convolution

integral in the cross section becomes,

$$\mathcal{I}\left[\left(\frac{\boldsymbol{p}_T\cdot\hat{\boldsymbol{P}}_{\boldsymbol{h}\perp}}{M_h}\right)\ f_{1T}^{\perp,q}(x,\boldsymbol{p}_T^2)D_1^q(z,z^2\boldsymbol{k}_T^2)\right]$$
$$= \frac{x f_{1T}^{\perp}\ D_1(z)}{z^2\pi^2\langle\boldsymbol{p}_T^2\rangle\langle\boldsymbol{k}_T^2\rangle}\int d^2\boldsymbol{p}_T\ d^2\boldsymbol{k}_T\ d^2\boldsymbol{P}_{h\perp}\left(\frac{\boldsymbol{p}_T\cdot\hat{\boldsymbol{P}}_{\boldsymbol{h}\perp}}{M_h}\right)$$
$$\times\delta^{(2)}(\boldsymbol{p}_T-\frac{\boldsymbol{P}_{h\perp}}{z}-\boldsymbol{k}_T)\exp\left(-\frac{\boldsymbol{p}_T^2}{\langle\boldsymbol{p}_T^2\rangle}-\frac{\boldsymbol{k}_T^2}{\langle\boldsymbol{k}_T^2\rangle}\right)$$
$$= f_{1T}^{\perp}(x)\cdot D_1(z)\cdot\frac{|\boldsymbol{P}_{h\perp}|}{M_N\pi z^3}\cdot\frac{\langle\boldsymbol{p}_T^2\rangle}{(\langle\boldsymbol{p}_T^2\rangle+\langle\boldsymbol{k}_T^2\rangle)^2}\exp\left[-\frac{\boldsymbol{P}_{h\perp}^2}{z^2(\langle\boldsymbol{p}_T^2\rangle+\langle\boldsymbol{k}_T^2\rangle)}\right]$$

By substituting this convolution integral to the $P_{h\perp}$ integration of the cross section, we obtain the deconvoluted expression with the Sivers function (1/2)-moment,

$$\int d^2\boldsymbol{P}_{h\perp}\ d\sigma_{\mathcal{S}}\propto-\sum_q\frac{e_q^2 f_{1T}^{\perp(1/2)q}(x)D_1^q(z)}{\sqrt{1+\langle\boldsymbol{p}_T^2\rangle/\langle\boldsymbol{k}_T^2\rangle}} \tag{3.24}$$

where the relation of transverse momenta $\langle\boldsymbol{P}_{h\perp}^2\rangle=z^2(\langle\boldsymbol{p}_T^2\rangle+\langle\boldsymbol{k}_T^2\rangle)$ is used. Similarly the Collins type cross section is obtained

$$\int d^2\boldsymbol{P}_{h\perp}\ d\sigma_{\mathcal{S}}\propto-\sum_q\frac{e_q^2 h_1^q(x)H_1^{\perp(1/2)q}(z)}{\sqrt{1+\langle\boldsymbol{k}_T^2\rangle/\langle\boldsymbol{p}_T^2\rangle}}.$$

One should note that both $\langle p_T^2\rangle$ and $\langle k_T^2\rangle$ can depend on x and z, respectively.

It is interesting to see the relation between $f_{1T}^{\perp(1)}$ and $f_{1T}^{\perp(1/2)}$. In particular in the Gaussian case, the moment of the Sivers functions is given by

$$f_{1T}^{\perp(1)}(x) = f_{1T}^{\perp}(x)\frac{\langle\boldsymbol{p}_T^2\rangle}{2M_N^2} \tag{3.25}$$
$$f_{1T}^{\perp(1/2)}(x) = f_{1T}^{\perp}(x)\frac{1}{4M_N}\sqrt{\pi\langle\boldsymbol{p}_T^2\rangle} \tag{3.26}$$

Hence we have the relation

$$\frac{f_{1T}^{\perp(1)}}{f_{1T}^{\perp(1/2)}}=\frac{2\sqrt{\langle\boldsymbol{p}_T^2\rangle}}{M_p\sqrt{\pi}}. \tag{3.27}$$

If we have both moments of the Sivers function $f_{1T}^{\perp(1)}$ and $f_{1T}^{\perp(1/2)}$, then they could give us information on the average intrinsic transverse momentum.

3.2 Collins Effect and Transversity

In this section, a common understanding about the Collins effect and transversity is explained.

In order to describe the Collins effect (or fragmentation function), it is needed to know about transversity which is introduced in Eq. (2.49) and Eq. (2.56).

Transversity is defined in Eq. (2.49). As shown in the definition, transversity is a tensor component of the quark-quark correlation function. In the helicity basis spin density matrix, the tensor component represents a helicity flip, and thus is a chiral-odd object. Transversity cannot be given a probabilistic interpretation in the helicity basis. However, in a transverse spin basis it reflects the probability of finding the transversely polarized quark inside the transversely polarized nucleon [41].

Due to the chiral-odd nature of transversity, it has to be coupled to an other chiral-odd object, which is the Collins fragmentation function $H_1^\perp$. This requirement comes from the fact that the experimental observables must be chiral-even in total. Also this fragmentation function is odd under *naive* time reversal (T-odd) which is time reversal without interchange of initial and final states. The single spin asymmetry arising from Collins function reflects the T-odd nature. Such asymmetries with longitudinal target polarization have been observed in pion electroproduction at HERMES [37].

Other chiral-odd PDFs

There are three other chiral-odd partners of the Collins function in the cross sections at leading twist (see Eqs. (2.67) - (2.69)).

- $h_1^\perp$ appears with $\cos(\phi)$ dependent in the cross section σ_{UU}. This function represents transversely polarized quarks inside the unpolarized nucleon.

- $h_{1L}^\perp$ shows up in the cross section of longitudinal spin component σ_{UL} together with $\sin(2\phi)$. This function describes transversely polarized quarks inside the longitudinally polarized nucleon.

- $h_{1T}^\perp$ is also coupled with the Collins function. But this function brings higher polynomials of transverse momenta and squared mass of the nucleon. It is expected to be suppressed.

3.3 Sivers Effect and Quark Orbital Angular Momentum

As we saw in Section 2.3, the Sivers function describes unpolarized quark inside a transversely polarized nucleon. It is thought that the Sivers function provides knowledge about "quark orbital angular momentum". If quarks do not have orbital angular momentum then the Sivers function should be zero.

In this section, possible interpretations of the Sivers effect (function) are presented. They are based on two theoretical views [22, 47].

The Sivers effect is understood as a final state interaction of the struck quark with the spectator system as presented in Fig. 3.2. The virtual photon

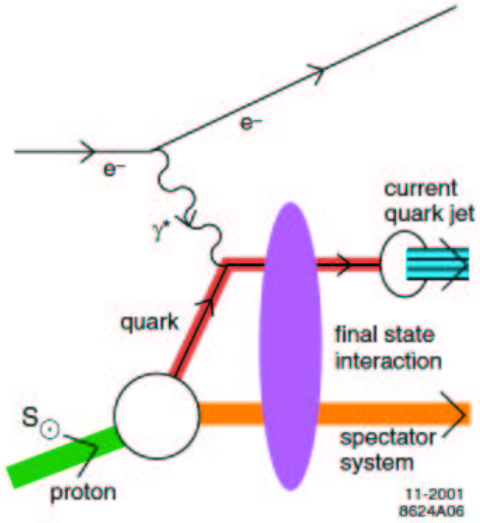

Figure 3.1: The virtual photon strike a quark inside the nucleon. The outgoing struck quark interferes with the spectator system "before" it fragmened into a hadron. [47]

strikes a quark inside the nucleon. The outgoing struck quark interacts with the spectator system "before" it fragments into hadron. The interference of the tree level graph and the one-loop graph including a gluon line are creating such a T-odd nature of this function. Even though the Sivers effect involves a final state interaction, factorization is proved for the Sivers function [48, 49].

The Sivers function itself is predicted to create Drell-Yan (e.g. $q\bar{q} \rightarrow q\bar{q}$) single-spin asymmetries [50]. It is expected that T-odd functions, such as the Sivers function, have a process dependence. The Sivers function has to change its sign between space-like (semi-inclusive DIS; SIDIS) and time-like

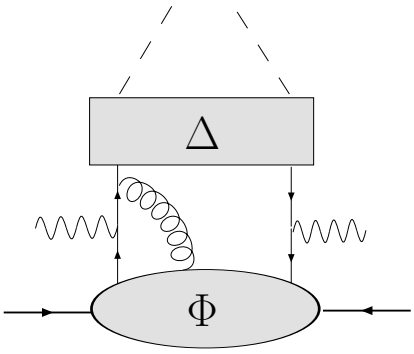

Figure 3.2: Add one gluon exchange to handbag diagram (*cf.* Fig. 2.11) [51]

(Drell-Yan; DY) processes due to the gauge link structure [52, 48] in order to regain time reversal symmetry of QCD,

$$f_{1T}^{\perp}\Big|_{SIDIS} = -f_{1T}^{\perp}\Big|_{DY}. \tag{3.28}$$

The interference between struck quark and the spectator system is described with a gauge-link. This gauge-link can be interpreted as a "soft" gluon exchange between the outgoing quark and spectator at leading order approximation. In this case, the outgoing quark is deflected by exchanging one gluon with the spectator. The interaction depends on the transverse spin of the nucleon leading to a left-right asymmetry in the direction of the outgoing quark (hadron).

A different approach is given in reference [22] using impact parameter dependent PDF's. The impact parameter dependent PDF is a physical interpretation of the generalized parton distributions [53, 54, 55]. The impact parameter $\boldsymbol{b}_\perp$ is defined as the distance between the active (struck) quark and center of longitudinal momentum. $\boldsymbol{b}_\perp$ is Fourier-conjugation to the transverse momentum $\boldsymbol{p}_T$. For transversely polarized nucleon targets, generalized parton distributions are asymmetric in impact parameter space. This impact parameter space asymmetry, together with the final state interaction, gives rise to the Sivers asymmetry. In the following, an interpretation of this mechanism based on the classical picture is described.

If quarks have orbital angular momentum parallel to the nucleon spin direction, then the probability to find a quark which carries momentum fraction of x is different, like a Doppler shift, between left and right sides in the nucleon when viewed from the virtual photon. The parton distribution are decreasing function of x. Namely, in this case, quarks are displaced to the left side with respect to the nucleon spin direction. In a model calculation

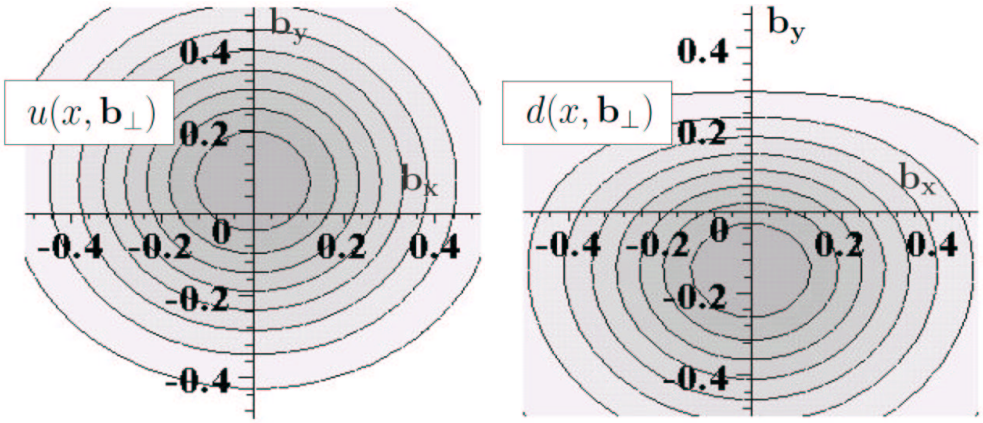

Figure 3.3: Distribution of u- (left) and d-quarks (right) in the $b_\perp$ space [22]. The proton is polarized to the positive b_x direction.

[22], such a displacement of is more pronounced for d-quark than for u-quark as shown in Fig. 3.3.

From above, if we assume u-quark has orbital angular momentum parallel to the nucleon spin, probability that virtual photon strikes the quark on the left side is dominant and outgoing struck u-quark gets deflected to the the "right side" via a soft gluon exchange as shown in Fig. 3.4 and 3.5. Finally, in this case, we may detect π^+ on the right side more often than on the left side with respect to the target spin direction.

3.4 Theoretical Predictions of Sivers function

At this moment, some theoretical predictions are available [56, 57, 39, 58, 59]. In Fig. 3.6, some of the theoretical predictions are plotted.

As shown in Fig. 3.6, even the sign of the Sivers function is not yet clear. However three theoretical predictions observe the same feature that the magnitude of the Sivers function for u-quarks is larger than that of d-quark, and they have opposite signs.

In the following, a short summary of the each prediction is listed.

Spectator model [58]

This gives the Sivers function in a spectator model with scalar and axial-vector diquarks. This model was developed from [60]. For the evaluation of the Sivers function one-gluon exchange is implemented as

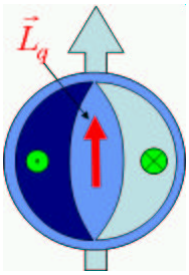

Figure 3.4: Schematic drawing of the impact parameter dependence. In case that the quark has orbital angular momentum L_q parallel to the nucleon spin direction, the probability for finding a quark on the left part of the nucleon (viewed from virtual photon) is larger than for finding a quark on the right side.

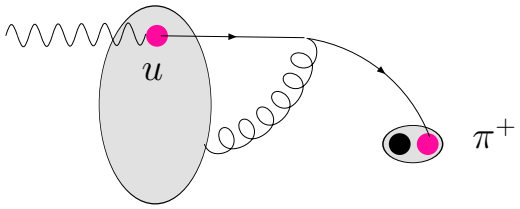

Figure 3.5: Combination of one-gluon exchange and the impact parameter dependence can generate the left-right asymmetry with respect to the nucleon spin direction. In the figure, picture of u-quark fragmenting into π^+ is displayed, for example.

a final state interaction. In this model, non-zero d-quark Sivers function can be obtained by including axial-vector diquarks in the spectator.

As the results, $f_{1T}^{\perp(1)u} > 0$ and $f_{1T}^{\perp(1)d} < 0$ is predicted.

MIT bag model [59]

The bag quark wave functions contain both S-wave and P-wave components, and their interference leads to non-vanishing Sivers functions. For the final state interaction the one-gluon approximation is used.

The obtained Sivers function from this model predicts; $f_{1T}^{\perp(1)u} < 0$ and $f_{1T}^{\perp(1)d} > 0$.

Fit $p^{\uparrow}p$ SSA data [57]

This gives the Sivers function with two inputs;

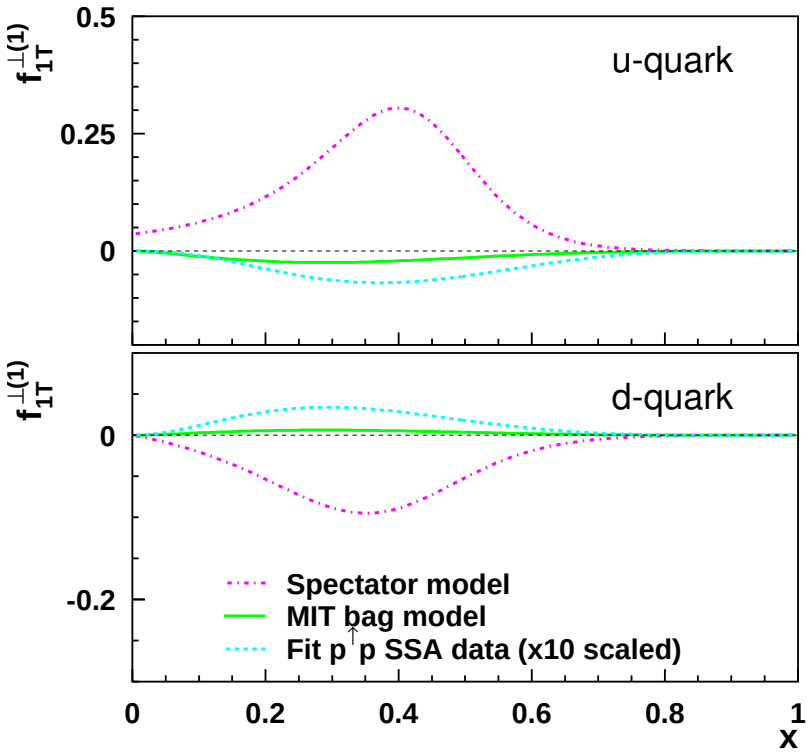

Figure 3.6: Theoretical predictions of the Sivers function for u- (upper panel) and d-quark (lower panel).

1. A parameterization [56] of $p^{\uparrow}p \to \pi X$ from FNAL E704 experiment [31], assuming the presence of Sivers effect only.
2. The value of the averaged transverse momentum $\langle p_T \rangle$ obtained from [61].

From this estimation, the Sivers function is obtained as $f_{1T}^{\perp(1)u} < 0$ and $f_{1T}^{\perp(1)d} > 0$. It should be noted that the sign of the Sivers functions are set to opposite to those in the paper [57] according to the reference [46].

In all the cases except [58], a small Sivers function is predicted. To that end, it is suggested in [58] that the difference of the magnitude of [58] from other predictions could be originated from sea-quark contributions because in particular the Sivers function of [57] was obtained from phenomenological studies of single spin asymmetry measured with $p^{\uparrow}p$ collision. From this

suggestion, the Sivers function of sea-quarks could have opposite sign to valence quarks.

Chapter 4

The HERMES Experiment

The HERMES experiment has been designed to study the spin structure of the nucleon. The experiment is studying the nucleon spin structure with the "Hadron Elektron Ring Anlage" (HERA), a synchrotron accelerator of the "Deutsches Elektronen Synchrotron" (DESY). It takes data on Deep Inelastic Scattering (DIS) of polarized positrons (electrons) and polarized and unpolarized nucleon gas targets.

The data presented in this thesis were collected in the years 2002 and 2003 at HERMES with a transversely polarized hydrogen target.

The spectrometer used in HERMES is a forward spectrometer [62] with a large acceptance to detect the scattered lepton and produced hadrons in the DIS processes. An overview of the spectrometer can be seen in Figure 4.1.

In the figure a part of detector is cut away in order to show the inside of the detector. The horizontal line is the positron (electron) beam pipe. In sequence, HERMES spectrometers consists of VC (Vertex Chamber), FC (Front Chamber), Hodoscope (H1, H2, H0), Spectrometer magnet, BC (Back Chamber), RICH (Ring Imaging Cherenkov counter), TRD (Transition Radiation Detector), and Calorimeter. The total length is about 10 m.

This chapter describes the components of the HERA accelerator relevant to the HERMES experiment, the HERMES target, and HERMES spectrometer.

4.1 The Beam

The HERMES experiment is located in the east straight section of the HERA facility at the DESY laboratory in Hamburg, Germany. HERA consists of two storage rings, with a 27.5 GeV positron (electron) beam and a 820 GeV proton beam.

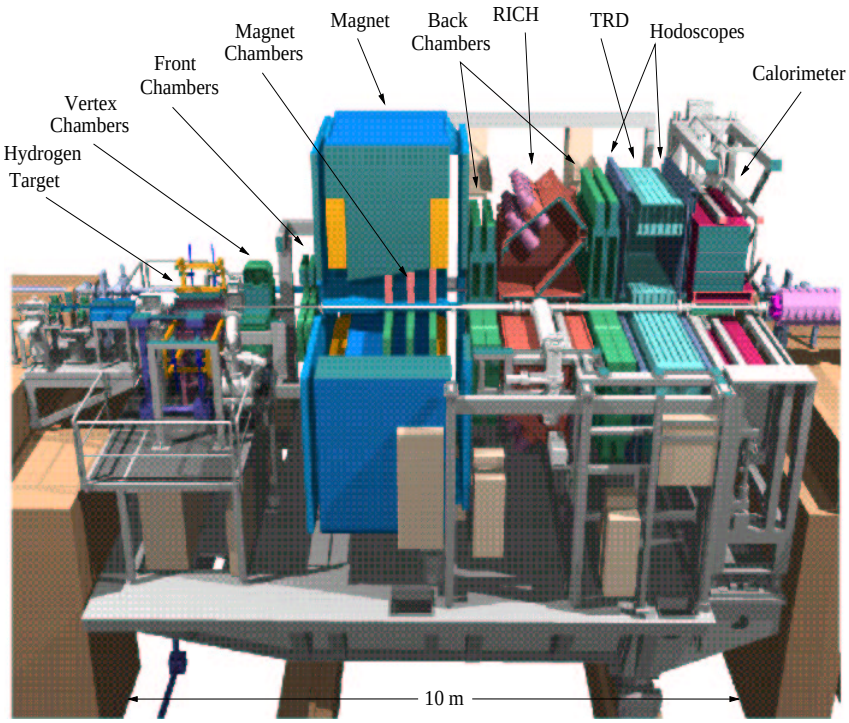

Figure 4.1: A three dimensional CAD diagram of the HERMES Spectrometer.

The HERMES experiment uses only the 27.5 GeV positron beam with maximum current of 40 mA at the beginning of a fill. Due to the residual gas interactions the beam current decreases nearly exponentially. Usually the beam will be dumped at around 10 mA or dumped after drastically reducing the current by inserting high density unpolarized gas in the HERMES target. Therefore typical fill length is around 8 hours.

The positron beam is separated into 220 bunches out of which up to 200 are filled. Generally the positron/electron beam gets polarized by itself transversely by the Sokolov-Ternov mechanism [63]. There are two spin rotators located up and downstream of the HERMES spectrometer. The first rotates the lepton spin to the longitudinal direction and the second one rotates it back to transverse. The transverse beam polarization is measured by a polarimeter in the West Hall of HERA. The polarization is constant in the whole storage ring. The polarization after passing through the first spin rotator and the detector is measured by the LPol (Longitudinal Polarimeter).

In the years from 1995 to 2000, double spin asymmetries have been measured using longitudinally polarized beam and targets to extract the polarized

nucleon structure function and quark helicity distributions. However for the asymmetries presented in this work, no beam polarization is required. The net beam polarization during the data taking presented in this thesis was small or zero.

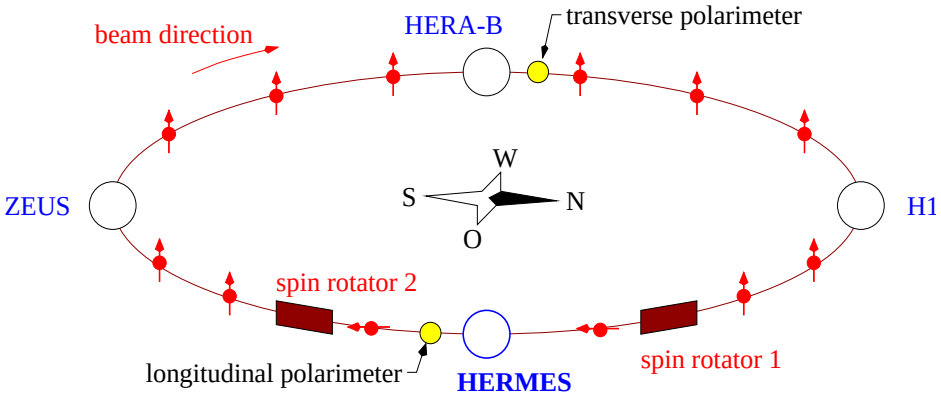

Figure 4.2: The HERA storage ring with HERMES and the other three experiments, ZEUS, H1 and HERA-B. The two spin rotators are located up and downstream of the HERMES experiment to realizing the longitudinal beam polarization.

4.2 The Target

It is technically difficult to polarize the nucleon of a pure solid material to a high degree and use them as a target in the lepton beam. Instead, HERMES uses internal gas targets, together with a storage cell technique to enhance the target density. Figure 4.3 shows a schematic view of the target. Hydrogen molecules are dissociated to hydrogen atoms. From one side the gas atoms are injected into a thin-walled, T-shaped tube which is called "storage cell". The storage cell is made of aluminum with length of 400 mm and wall thickness of 0.125 mm. The target atoms remain inside the cell for typically 3 ms and cross the interaction region many times. When the target atoms are in the target cell, the following interactions are needed to be considered;

- Recombination: the atoms inside the target storage cell hit the cell walls and form molecules.
- Wall depolarization: the atoms attached to the wall by collision lead

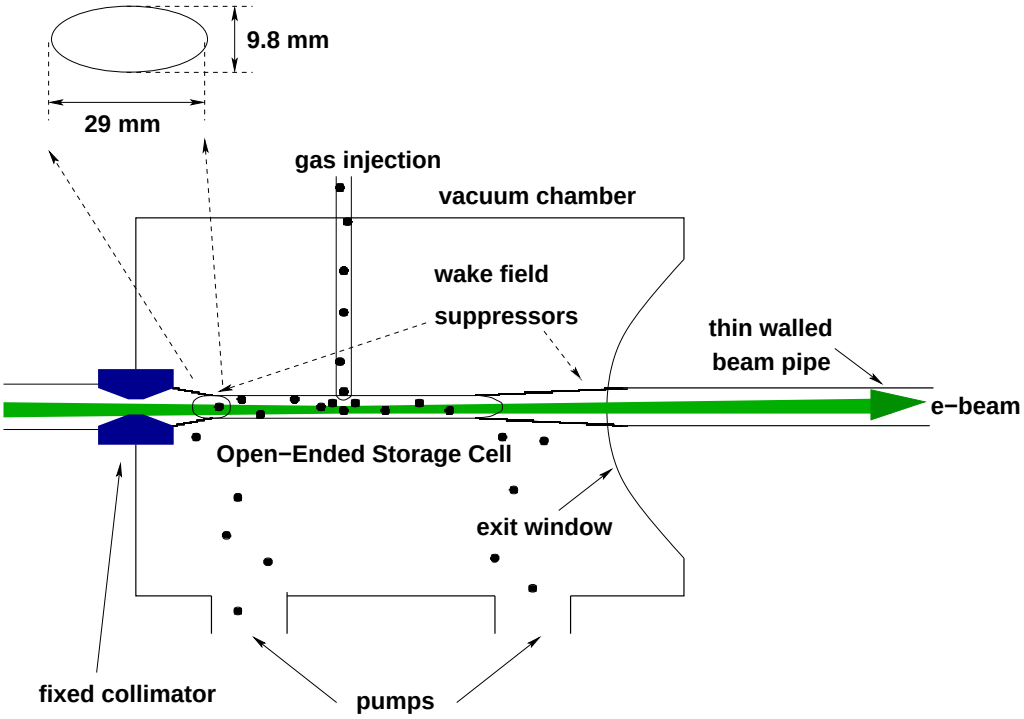

Figure 4.3: Schematic view of the HERMES together with storage cell.

to a relaxation of the atom polarization by the interaction with surface magnetic fields.

- Spin exchange collisions: a collision of the atoms may lead to a spin exchange between the hyperfine states of the atoms and cause exchange of electron and proton spin.

Now the target thickness achieved is 7×10^{13} atoms/cm^2, which is more than two orders of magnitude higher compared to the target thickness by a free jet target, usually 2×10^{11} atoms/cm^2 [62]. These are the surface density viewed from the electron beam direction. The orientation of the target spin is reversed every 60 seconds, including the removal of the target gas from the cell, to keep systematic influences on the asymmetry measurements at a minimum level.

Once the gas reaches the target cell a magnetic holding field defines the quantization axis for the nuclear polarized states. Before 2001 this field was longitudinally oriented with respect to the lepton beam, which allowed to measure longitudinally polarized target spin asymmetries. In the year 2001

the magnet was replaced by a transverse target magnet (see Fig. 4.4). Such

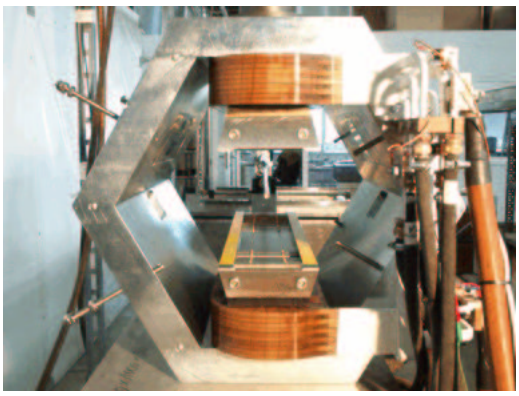

Figure 4.4: Front-view of the transverse magnet.

a transverse magnet field deflects all charged particles by the Lorentz force, therefore correction coils were employed to stabilize the orbit of the lepton beam.

4.3 The Detector Components

HERMES spectrometer has a large acceptance in the forward direction. This spectrometer is shown in Figgure 4.5 and Figure 4.1 [62]. With the HERMES detector, scattered and produced particles are accepted in vertical angle 40 mrad $< |\theta_y| <$ 140 mrad, and in horizontal angle $|\theta_x| <$ 170 mrad, where the lower vertical limit is given by the septum plate. The total acceptance of scattering angles is 40 mrad $< |\theta| <$ 220 mrad [62].

A spectrometer magnet and several detectors for particle tracking allow the determination of particle momenta. The tracking system consists of microstrip gas chambers, drift chambers and three proportional chambers in the magnet.

For semi-inclusive measurements, HERMES needs a very good particle identification (PID), not only to separate leptons from hadrons, but also to identify the hadrons. Semi-inclusive measurement means that a part of hadrons are detected in coincidence with the scattered lepton. To achieve a high quality particle identification, the HERMES spectrometer is equipped with four special PID detectors, an electromagnetic lead-glass calorimeter, a preshower hodoscope, a transition radiation detector (TRD) and Cherenkov Counter. The original threshold Cherenkov has been replaced in 1998 by a

Ring Imaging Cherenkov Counter (RICH) to allow a clean hadron identification over the momentum range of $2 \sim 15$ GeV/c.

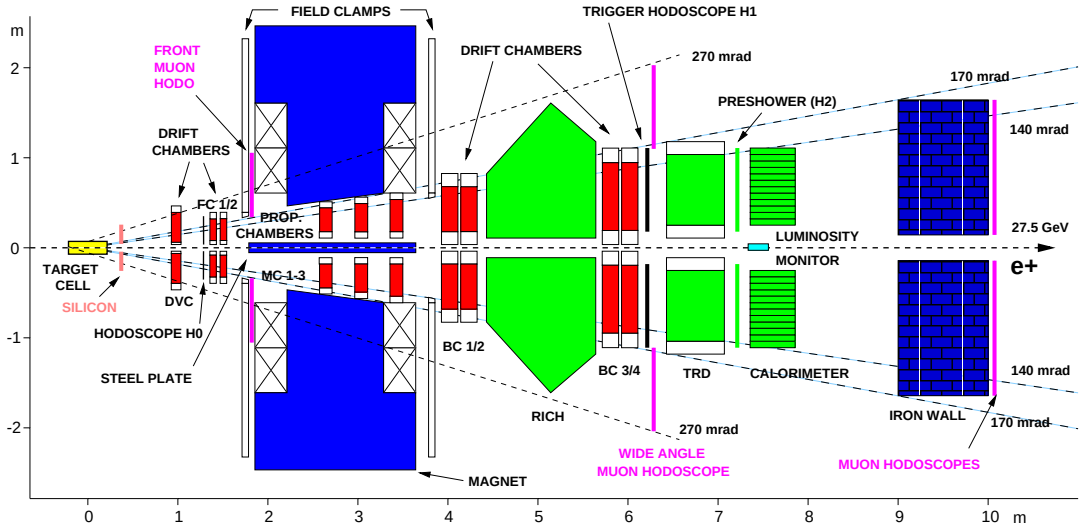

Figure 4.5: The HERMES Spectrometer. Two identical detectors are built above and below the beam line. The Cherenkov Counter was operated as a threshold Cherenkov Counter during 1995 - 1997 data taking. Since 1998, a Ring Imaging Cherenkov Counter is installed to identify produced hadrons.

4.3.1 The Tracking System

Spectrometer Magnet

The HERMES spectrometer has a H-type magnet with a deflecting power of 1.5 Tm and it is usually operated at 1.3 Tm for the momentum measurement. The lepton beam line is protected by a horizontal septum plate with compensator coils which are arranged in the beam plane.

Vertex and Front Chambers

In the upstream region of the spectrometer magnet, the drift vertex chambers DVC and the drift front chambers FC1/2 are installed to reconstruct the particle vertex and to determine the scattering angle.

The FC's are a pair of drift chambers, each chamber has 6 planes. The size of drift cell is 7 mm (3.5 mm maximum drift length), and the used gas is $Ar/CO_2/CF_4$ ($Ar:CO_2:CF_4$ 90:5:5) like in all other HERMES drift chambers.

The DVC acceptance is vertically $\pm$ 35 mrad $\sim \pm$ 270 mrad and horizontally $\pm$ 200 mrad. The DVC drift cell is smaller than the FC's.

Magnet Chambers

The proportional wire chambers MC1/2/3 are installed in the gap of the spectrometer magnet. They were originally installed to analyze multiple tracks in high multiplicity events.

It has turned out that they are also particularly useful for the analysis of particles with low energy which are deflected by the magnet so that they are not detected by the BC's; pion from the Λ-decays, for example. Each chamber consists of 3 modules. The distance between anode and cathode planes is 4.00 ± 0.03 mm. The gas is the same as the drift chambers but the proportions of the mixture is different ($Ar:CO_2:CF_4$ 65:30:5).

Back Chambers

In the region downstream of the spectrometer magnet two sets of the back drift chambers BC1/2 and BC3/4 are mounted. The difference between BC1/2 and BC3/4 is the detector size. The active areas of these modules depend on their z-position and the acceptance of the spectrometer. The BC1/2 active area is horizontally 1880 mm and vertically 520 mm, and the BC3/4's is 2890 mm and 710 mm. Each set of chambers has two modules with 6 planes. The efficiency of the drift chamber depends on the drift distance and the typical efficiency is well above 99%. The details are shown in [64]. These detectors are shown in Fig.4.6.

4.3.2 The Particle Identification System

As mentioned before, a clean particle identification is very important at HERMES. The PID is performed in two steps: first a lepton-hadron separation and second the identification of the hadron. Especially the second point is essential for the study of the quark spin distribution. As for the lepton-hadron separation, the hadron rejection factor (HRF) of the system is designed to be 10^4 at least, where HRF is defined as the total number of hadrons divided by the number of hadrons misidentified as leptons.

This value depends on the efficiency for the lepton identification. The contamination of the lepton sample by hadrons is below 1% for the whole

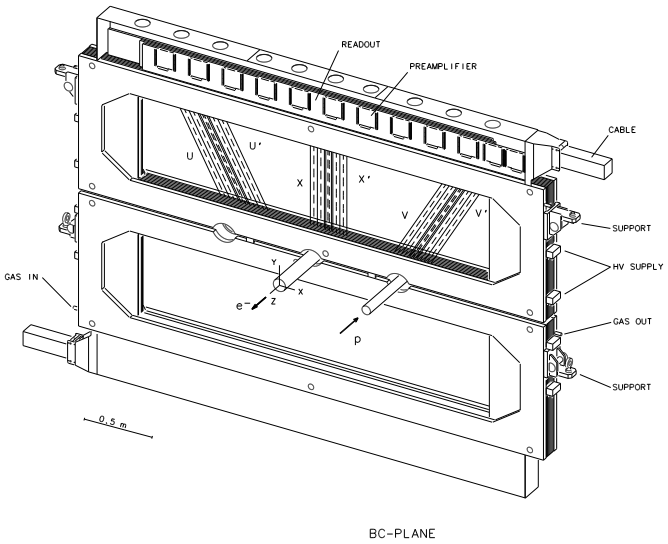

Figure 4.6: Schematic view of the HERMES BC module.

kinematic range. This hadron rejection is achieved by the calorimeter, the preshower hodoscope and the TRD. The second step, the hadron identification is done by the fourth PID detector, the RICH. These four detectors are described in the following.

Calorimeter

The calorimeter (Fig.4.7) is part of the first level trigger for scattered positrons (electrons). It consists of two modules which have 420 blocks each above and below the beam line. All 840 blocks are made by identical lead-glass blocks with size of $9 \times 9 \times 50$ cm (about 18 radiation length), and are arranged in a 42×10 array for each module. The lead glass chosen is F101 which has high durability for radiation damage [65]. The blocks are polished, wrapped with 50 μm thick alminized mylar foil and covered with a 125 μm thick tedlar foil to provide light insulation. Each block is coupled to a 7.5 cm Philips XP3461 photo-multiplier with a silicon glue (SILGARD 184) with a refractive index of 1.41. Each block is read out by a photo-multiplier tube (PMT). Both calorimeter walls can be moved 50 cm vertically from the beam pipe to prevent radiation damage during beam injection or dump.

The energy resolution of this detector is parameterized by the following

function;

$$\frac{\sigma_E}{E}[\%] = \frac{5.1 \pm 1.1}{\sqrt{E[\mathrm{GeV}]}} + (2.0 \pm 0.5) + \frac{10.0 \pm 2.0}{E[\mathrm{GeV}]} \tag{4.1}$$

which is slightly degraded compared to the test beam results ($\sigma_E/E = 1.5 \pm 0.5 + (5.1 \pm 1.1)/\sqrt{E(\mathrm{GeV})}$) [66]. Combined with the preshower counter, the efficiency for the detection of lepton is about 95%. The actual energy resolution of the calorimeter can be seen in Figure 4.8.

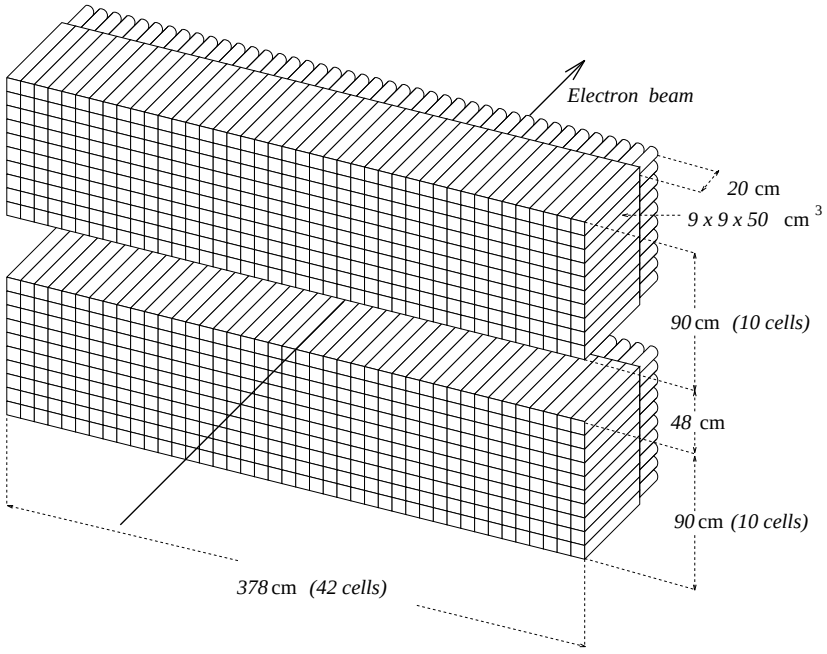

Figure 4.7: Isometric view of the HERMES Calorimeter.

The calorimeter basically evaluates the energy of the incident particle by the number of Cherenkov photons. Incoming particles produce electrons in the lead glass, then the shower electrons emit Cherenkov photons. The calorimeter PMT reads out the number of emitted photons. The shower which was produced by the incident particle is spread to the neighboring eight blocks. To estimate the incoming particle energy it is summed over all lead glass blocks on which the preshower spread. Usually the sum is taken for 9 blocks.

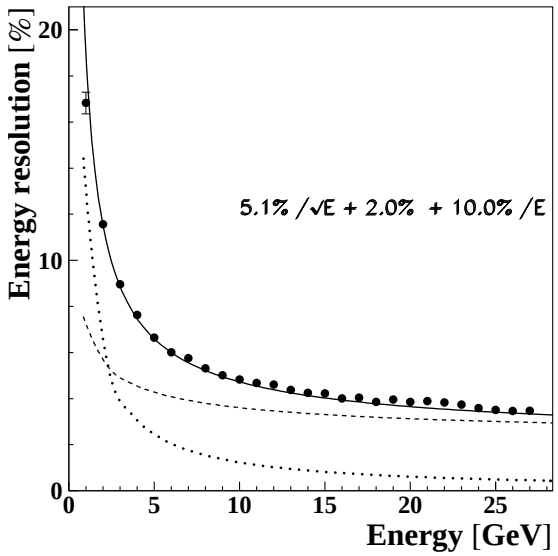

Figure 4.8: Energy resolution of the calorimeter. The circles are real data corrected by Monte Carlo. The solid line is sum of the calibrations from the lead glass (dashed curve) and from the preshower (dotted curve).

Hodoscopes

There are hodoscopes H0, H1 and H2, which are plastic scintillators. H2 is behind the 11 mm Pb radiator (two radiation lengths) sandwiched between two 1.3 mm stainless steel sheets and used as a preshower counter in front of the calorimeter.

The first level trigger is obtained by a combination of the calorimeter, H0, H1 and H2. Both hodoscopes consist of 42 vertical scintillator modules each in the upper and lower detector. The size of the modules is $9.3 \times 91 \times 1$ cm^3 and they are read out by PMTs of 5.2 cm diameter.

Transition Radiation Detector

The transition radiation detector (TRD) is used for the discrimination between leptons and hadrons [67]. Only leptons emit transition radiation in the HERMES energy region.

The HERMES TRD is a multiwire proportional chamber constructed by 6 modules above and below the beam. Each module has polyethylene/ polypropylene fibers as radiators and Xe/CH_4 gas (90:10) in the proportional

chamber. The fibers used for the radiators are 17-20 μm in diameter and have a material density of 0.059 g/cm^3. The radiators are 6.35 cm thick, and Xe/CH_4 has been chosen because of its efficient X-ray absorption.

The chambers are 2.54 cm thick and the wire diameter was unusually large 75 μm to allow operation at high voltage while limiting the gas gain to about 10^4. The original purpose of the TRD is to obtain a pion rejection factor (PRF) of at least 100 with 90% lepton efficiency at 5 GeV and above, accordingly the energy averaged PRF is about 300 [67] with 90% lepton efficiency. When we analyze the data as a function of momentum, the PRF of 130 is obtained at 5 GeV. The design goal is therefore accomplished.

Ring Imaging Cherenkov Counter

To study the quark spin structure, it is necessary that produced hadrons (pions, kaons, protons) are identified separately. Until 1998, a threshold Cherenkov Counter was used to identify pions which are produced in a DIS event. This threshold Cherenkov Counter had good performance for pion separation from hadrons. The efficiency of this counter was above 99%. In 1998 a Ring Imaging Cherenkov Counter (RICH) was installed as a substitute for the threshold Cherenkov Counter. The HERMES RICH is designed to identify pions, kaons and protons in a momentum region of $2 \sim 15$ GeV/c. This RICH has two radiators : aerogel and C_4F_{10} gas. Measuring two ring images produced by Cherenkov photons on the PMT plane, we can identify and separate each particle. Actual efficiency of the pion identification reaches 98%, kaon identification efficiency reaches 93%[68].

All of these 4 detector responses give some information to the distinction between leptons and hadrons. Combined likelihood ratios for the 2 assumptions were created for these detector components which are defined as

$$\mathrm{PID} = \log_{10} \frac{P(e)}{P(h)} \tag{4.2}$$

and are called PID values. The sum of the PID values from preshower, Calorimeter and the RICH used as an threshold Cherenkov are defined as PID_3; the PID value of the TRD is defined as PID_5. The combination of these 2 PID values allows a lepton and hadron detection efficiency of 98%.

4.4 Luminosity Monitor

The luminosity monitor is based on the detection of Møller or Bhabha scattering off electrons from the shell of the target atom. Two calorimeter on

both sides of the beam pipe measure symmetric scattering with an angular acceptance of 4.5 to 8.2 mrad. The coincidence rates depend on the type of the beam : For a nominal beam current and a nominal H target density of 1×10^{14} atoms/cm^2 in the case of the electron beam (Møller scattering) the coincidence rate is 116 Hz and in case of the positron beam (Bhabha scattering and pair production) the coincidence rate is 86 Hz. The energy of scattered electrons and positrons are in the range of 10 to 20 GeV when they are in the acceptance of the detector. Each calorimeter consists of 12 $NaBi(WO_4)_2$ crystals which have a size of $22 \times 22 \times 200$mm^3. They are Cherenkov radiators, are insensitive to low energy background and have a good time resolution. To reduce radiation damage, the counter can be horizontally moved away from the positron (electron) beam pipe during injection time of the beam.

4.5 Gain Monitoring System

Stability of the PID detectors, calorimeter and preshower counter etc. are monitored by the Gain Monitoring System (GMS). The GMS monitors not only the PID detectors but also the luminosity monitor, the H0 hodoscope, and the longitudinal polarimeter (LPol). In total more than 900 Photo-Multiplyer Tubes (PMT) are used for the detectors. The main aim is to measure the stability of PMTs of those detectors. The GMS is operating since the start-up of the HERMES experiment in 1995. Various improvements were made recently as described in the reference [69].

The GMS operation includes the light transmission to the detector, the production of electrical signals by photo-sensitive detectors, signal processing (amplification, shaping), and digitization. The GMS injects a Laser light to the PMTs, and at the same time, to an array of reference detectors via an optical fiber network. The light can be attenuated by means of filters mounted on a rotating wheel. The generation of a GMS event begins when one of the filters is in front of the light source with a rate of a few Hz. When the filter is in position of the light source, a Nd:YAG laser, is triggered to generate an intense pulse of light. The data which are tagged with the current filter number are included in the event data stream in a special GMS event. Comparing the initial response of a detector to the response later in the experiment the stability of the detector response is monitored.

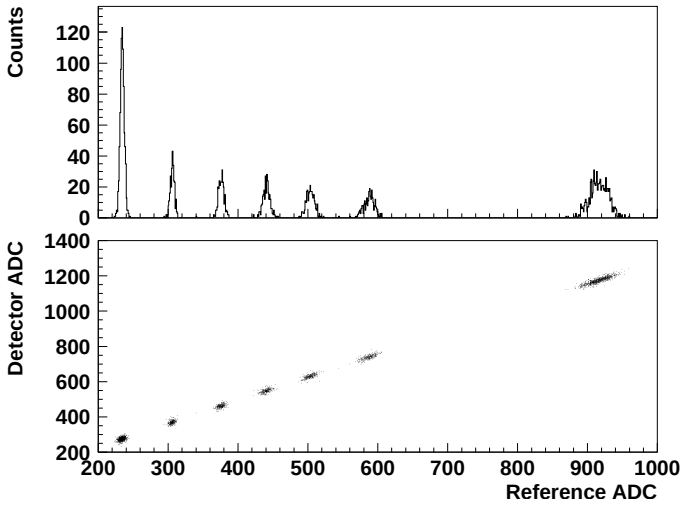

Figure 4.9: The upper panel shows a typical ADC histogram recorded by one of the reference detectors. The lower panel shows the typical correlation between the responses of a monitored detector and a reference detector.

Chapter 5

Extraction of Single Target-Spin Asymmetries

In this chapter, the determination of the single-spin azimuthal asymmetry is described. In the first part, definition and formalism of the asymmetry are explained. Several tests to extract the asymmetry are described. The results of extracted asymmetries are shown with a discussion of various systematic studies. The chapter concludes with comparison with results from other experiments. The asymmetries shown in this chapter is not corrected for detector instrumental and QED radiative effects. The correction is discussed in the following chapter.

5.1 Formalism of Asymmetry

5.1.1 Angle Definition

In deep inelastic scattering (DIS) off a target with a transverse polarization component, two azimuthal angles can be defined. Those play an important role to disentangle two effects, Sivers effect and Collins effect. These angles are defined between the lepton scattering plane and either the transverse momentum of the produced hadron or the transverse component of the polarization vector of the target as shown in Fig. 5.1.

As already explained in Section 2.4.2, depending on the coordinate system, especially direction of z-axis, azimuthal angles become opposite sign. In this thesis, the coordinate system shown in Fig. 5.1 is used according to [46].

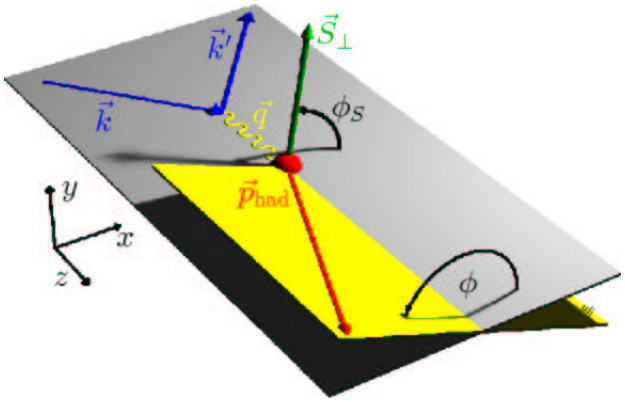

Figure 5.1: Definition of the azimuthal angles.

Those angles can be computed according to the definition as,

$$\phi_S = \frac{(\boldsymbol{q}\times\boldsymbol{k})\cdot\boldsymbol{S}}{|(\boldsymbol{q}\times\boldsymbol{k})\cdot\boldsymbol{S}|}\cdot\cos^{-1}\left(\frac{(\boldsymbol{q}\times\boldsymbol{k})}{|\boldsymbol{q}\times\boldsymbol{k}|}\cdot\frac{(\boldsymbol{q}\times\boldsymbol{S})}{|\boldsymbol{q}\times\boldsymbol{S}|}\right), \tag{5.1}$$

$$\phi = \frac{(\boldsymbol{q}\times\boldsymbol{k})\cdot\boldsymbol{P}_h}{|(\boldsymbol{q}\times\boldsymbol{k})\cdot\boldsymbol{P}_h|}\cdot\cos^{-1}\left(\frac{(\boldsymbol{q}\times\boldsymbol{k})}{|\boldsymbol{q}\times\boldsymbol{k}|}\cdot\frac{(\boldsymbol{q}\times\boldsymbol{P}_h)}{|\boldsymbol{q}\times\boldsymbol{P}_h|}\right), \tag{5.2}$$

where $\boldsymbol{q}$, $\boldsymbol{k}$ are 3-vectors of the virtual photon and incoming lepton momenta, $\boldsymbol{P}_h$ is also 3-vectors of momentum of the produced hadron in lab frame, and $\boldsymbol{S}$ is 3-vectors of the polarization vector of the target nucleon.

5.1.2 Cross Section Asymmetry

As defined in the previous chapter, the differential cross section $d\sigma_{UT}$ contains Sivers function, transversity and Collins fragmentation fucntion. In principle, the cross section σ_{UT} can be measured keeping the target in one spin states. However in experiment, we use two target spin states, so-called *up* and *down* which are defined in HERMES coordinate system. Several experimental ambiguities are minimized using the two spin states.

The observable is the cross section asymmetry A^h_{UT} which is defined as follows,

$$A^h_{UT}(\phi,\phi_S) = \frac{d\sigma^{\uparrow}_h(\phi,\phi_S) - d\sigma^{\downarrow}_h(\phi,\phi_S)}{d\sigma^{\uparrow}_h(\phi,\phi_S) + d\sigma^{\downarrow}_h(\phi,\phi_S)} \tag{5.3}$$

$$= \frac{1}{|S_T|}\frac{N^{\uparrow}_h(\phi,\phi_S) - N^{\downarrow}_h(\phi,\phi_S)}{N^{\uparrow}_h(\phi,\phi_S) + N^{\downarrow}_h(\phi,\phi_S)} \tag{5.4}$$

where $d\sigma^{\uparrow(\downarrow)}$ is the differential cross section for hadron production in DIS, and $N^{\uparrow(\downarrow)}$ is semi-inclusive luminosity-normalized hadron yield in target spin up (down) states. The differencial cross section $d\sigma^{\uparrow,\downarrow}$ in each target spin state is related to $d\sigma_{UT}$ via,

$$\begin{aligned} d\sigma^{\uparrow}(\phi,\phi_S) &= d\sigma_{UU} + d\sigma_{UT}(\phi,\phi_S), & (5.5)\\ d\sigma^{\downarrow}(\phi,\phi_S) &= d\sigma_{UU} + d\sigma_{UT}(\phi,\phi_S+\pi). & (5.6) \end{aligned}$$

where the $d\sigma_{UU}$ is the unpolarized cross section, and $d\sigma_{UT}$ is spin-dependent cross section.

At leading order of $1/Q$, the corss section $d\sigma_{UT}$ has azimuthal angle dependence [35, 36] as,

$$\begin{aligned} d\sigma_{UT}(\phi,\phi_S) \propto\ & d\sigma_{\mathcal{S}} \cdot \sin(\phi-\phi_S) \\ +\ & d\sigma_{\mathcal{C}} \cdot \sin(\phi+\phi_S) \\ +\ & d\sigma_{\mathcal{O}1} \cdot \sin(3\phi-\phi_S) \\ +\ & d\sigma_{\mathcal{O}2} \cdot \sin(\phi_S) \\ +\ & d\sigma_{\mathcal{O}3} \cdot \sin(2\phi-\phi_S) \end{aligned} \quad (5.7)$$

where $d\sigma_{\mathcal{S}}$ and $d\sigma_{\mathcal{C}}$ are cross sections which include Sivers and Collins functions respectively, $d\sigma_{\mathcal{O}1}$ is other leading twist cross section as presented in Eq. (2.69), $d\sigma_{\mathcal{O}i}$ $(i=2,3)$ indicates twist-three corss sections.

In addition to the $d\sigma_{UT}$, the unpolarized cross section $d\sigma_{UU}$ also has azimuthal dependence [35, 36],

$$d\sigma_{UU}(\phi) = d\sigma_{\mathcal{U}} + d\sigma_{\mathcal{O}0} \cdot \cos(2\phi). \quad (5.8)$$

where $d\sigma_{\mathcal{U}}$ is the usual unpolarized corss section which involves unpolarized parton distribution $f_1(x)$ and fragmentaion functions $D_1(z)$, $d\sigma_{\mathcal{O}0}$ is also leading-twist corss section as introduced in Eq. (2.67). This unpolarized *asymmetry* could create a complication when the Sivers and Collins asymmetries are extracted, but we ignore this contribution at least for a while, and discuss it later specially.

From the azimuthal dependence of the spin-dependent part, in Eq. (5.7), we obtain $d\sigma_{UT}(\phi,\phi_S) = -d\sigma_{UT}(\phi,\phi_S+\pi)$. Consequently the asymmetry A^h_{UT} can be rewritten in terms of $d\sigma_{UT}$ and $d\sigma_{UU}$,

$$
\begin{aligned}
A_{UT}^{h} &= \frac{d\sigma^{\uparrow} - d\sigma^{\downarrow}}{d\sigma^{\uparrow} + d\sigma^{\downarrow}} \\
&= \frac{d\sigma_{UU}(\phi,\phi_S) + d\sigma_{UT}(\phi,\phi_S) - \{d\sigma_{UU}(\phi,\phi_S+\pi) + d\sigma_{UT}(\phi,\phi_S+\pi)\}}{d\sigma_{UU}(\phi,\phi_S) + d\sigma_{UT}(\phi,\phi_S) + \{d\sigma_{UU}(\phi,\phi_S+\pi) + d\sigma_{UT}(\phi,\phi_S+\pi)\}} \\
&= \frac{d\sigma_{UT}}{d\sigma_{UU}} \\
&= \left(\frac{d\sigma_{\mathcal{S}}}{d\sigma_{UU}}\right)\sin(\phi-\phi_S) + \left(\frac{d\sigma_{\mathcal{C}}}{d\sigma_{UU}}\right)\sin(\phi+\phi_S) \\
&+ \left(\frac{d\sigma_{\mathcal{O}1}}{d\sigma_{UU}}\right)\sin(3\phi-\phi_S) + \left(\frac{d\sigma_{\mathcal{O}2}}{d\sigma_{UU}}\right)\sin(\phi_S) + \left(\frac{d\sigma_{\mathcal{O}3}}{d\sigma_{UU}}\right)\sin(2\phi-\phi_S)
\end{aligned}
\tag{5.9}
$$

Therefore it is possible to disentangle between Sivers, Collins and other terms of $d\sigma_{UT}$ by looking at the dependence on two independent variables, ϕ and ϕ_S using the corss section asymmetry. In principle, these terms can be extracted separately as they are terms of a Fourier expansion of the polarized semi-inclusive DIS corss section. In practice, one leads to extract them by applying a fit with respective sinusoidal function to avoid cross contamination due to a limited spectrometer acceptance as will be discussed later.

5.2 Monte Carlo Studies

In this section, we discuss the method to extract Sivers and Collins asymmetries. It corresponds to the extraction of $d\sigma_{\mathcal{S}}$ and $d\sigma_{\mathcal{C}}$ from the cross section asymmetry.

For a test of the extraction method, a Monte Carlo simulation program which generates the asymmetries is needed. However up to now no Monte Carlo generator is available for those purpose, since the nucleon structure of the transversely polarized nucleon is completely unknown. Therefore, how to prepare Monte Carlo dataset is discussed stepwise below.

5.2.1 Generating Azimuthal Asymmetry in a Monte Carlo Simulation

All Monte Carlo studies were done with a Monte Carlo event generator for unpolarized DIS. As presented in Eq. (5.7), the total cross section which is integrated over $P_{h\perp}$, ϕ and ϕ_S is consistent with unpolarized cross section.

Thus we do not need to change total number of generated hadrons. The issue is just to produce a ϕ- and ϕ_S-dependence of hadron distribution.

The polarized cross section can be generated with an unpolarized Monte Carlo event generator (generated in 4π geometry) by weighting all events with various azimuthal angle dependences. The weight is given as follows,

$$w^{\pm} = w_u(1 \pm w_{UT}(x, \phi, \phi_S)), \tag{5.10}$$

$$\begin{aligned} w_{UT}(x, \phi, \phi_S) &= w_S(x) \cdot \sin(\phi - \phi_S) + w_C(x) \cdot \sin(\phi + \phi_S) \\ &\quad + w_{O1}(x) \cdot \sin(3\phi - \phi_S) + w_{O2}(x) \cdot \sin(\phi) \\ &\quad + w_{O1}(x) \cdot \sin(2\phi - \phi_S) + ... \end{aligned} \tag{5.11}$$

where w_u is unpolarized weight which corresponds to usual unpolarized corss section, $\pm$ depends on target spin state. The generated hadron yield and asymmetries can be expressed as,

$$N^{\uparrow\downarrow}(x, \phi, \phi_S) = N^u(x) \pm \sum_i^{N^{\uparrow\downarrow}} w^i_{UT}(x, \phi, \phi_S) \tag{5.12}$$

$$A_{UT}(x, \phi, \phi_S) = \frac{N^{\uparrow}(x, \phi, \phi_S) - N^{\downarrow}(x, \phi, \phi_S)}{N^{\uparrow}(x, \phi, \phi_S) + N^{\downarrow}(x, \phi, \phi_S)} \tag{5.13}$$

$$= \frac{1}{N^u} \left[\sum_i^{N^u} w^i_{UT}(x, \phi, \phi_S) \right] \tag{5.14}$$

where N^u indicates unpolarized hadron yield. Finally the same form as Eq. (5.9) is obtained.

5.2.2 Asymmetry Reconstruction Method

As shown in the previous section, the cross section asymmetry allows us to access the Sivers and Collins cross sections: $d\sigma_S$ and $d\sigma_C$, which appear as amplitudes of the different sine modulations. In order to to extract the Sivers and Collins asymmetries, two method can be considered: one is projection-method, another is fit-method. In this section, the two methods will be tested.

Projection method

In most of all theory papers, the $\sin\Phi$ moment (e.g. $\Phi = \phi \pm \phi_S$, for Collins and Sivers type) is obtained by weighting the cross section asymmetry with

the corresponding sine modulations,

$$\Big\langle \mathcal{W} \sin\Phi \Big\rangle_{UT} = \frac{\displaystyle\int d\phi_S \; d^2\boldsymbol{P}_{h\perp} \; \Big[\mathcal{W}\sin\Phi\Big] d\sigma_{UT}}{\displaystyle\int d\phi_S \; d^2\boldsymbol{P}_{h\perp} \; d\sigma_{UU}}, \tag{5.15}$$

where the integration over ϕ arises from $d^2\boldsymbol{P}_{h\perp} = |\boldsymbol{P}_{h\perp}| \; d|\boldsymbol{P}_{h\perp}| \; d\phi$, and $\mathcal{W}$ is the weight function of event kinematics, e.g. $P_{h\perp}$, z. This weight function is needed for the deconvolution of parton distribution and fragmentation functions (see Section 3.1.1). To obtain an unweighted asymmetry, just set $\mathcal{W}$ to 1. In this approach, only one sine modulation is projected out leaving all other terms in the polarized cross section.

This projection method gives the cleanest way to extract each effect separately. This is motivated by the fact that the azimuthal asymmetry Eq. (5.7) is expressed as a Fourier expansion in ϕ and ϕ_S. So, if we look at Sivers asymmetry, the projection-method gives,

$$\begin{aligned}
[\text{numerator of Eq. (5.15)}] \;\; &\propto \;\; d\sigma_{\mathcal{S}} \int_0^{2\pi} d\phi \int_0^{2\pi} d\phi_S \;\; \underbrace{\sin^2(\phi-\phi_S)}_{=\frac{1}{2}(1-\cos 2(\phi-\phi_S))} && (5.16)\\
&+ \;\; d\sigma_{\mathcal{C}} \int d\phi \; d\phi_S \; \underbrace{\sin(\phi+\phi_S)\sin(\phi-\phi_S)}_{=-\frac{1}{2}(\cos\phi-\cos\phi_S)} && (5.17)\\
&+ \;\; \ldots \\
&= \;\; d\sigma_{\mathcal{S}} \frac{1}{2}(2\pi)^2.
\end{aligned}$$

Thus only the Sivers term survives. In addition, $(2\pi)^2$ factor in the equation above is canceled out by unpolarized part in asymmetry,

$$[\text{denominator of Eq. (5.15)}] \;\; \propto \;\; d\sigma_{UU} \cdot \int d\phi \; d\phi_S \;\; = d\sigma_{UU} \cdot (2\pi)^2.$$

Combining these two, the Sivers asymmetry is obtained,

$$\big\langle \sin(\phi-\phi_S) \big\rangle_{UT} = \frac{1}{2}\left(\frac{d\sigma_{\mathcal{S}}}{d\sigma_{UU}}\right). \tag{5.18}$$

It should be noted that this projection method gives a half of the amplitude presented in Eq. (5.9).

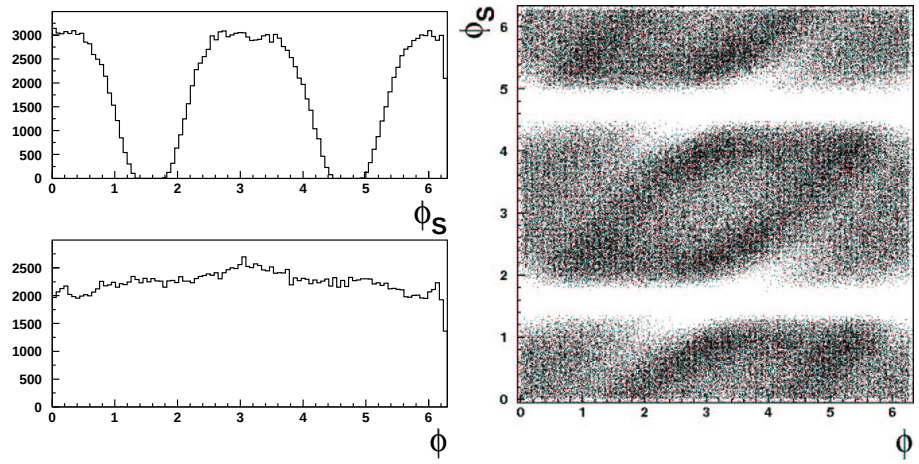

Figure 5.2: ϕ_S and ϕ distribution for detected hadrons.

In principle, this projection method can be applied to experimental data as well. The asymmetry can be obtained by counting up the detected hadrons with the weight "$\mathcal{W}\sin(\Phi)$",

$$\left\langle \mathcal{W}\sin\Phi \right\rangle_{UT} = \frac{\sum_i^{N_h^\uparrow} \mathcal{W}_i \sin\Phi - \sum_i^{N_h^\downarrow} \mathcal{W}_i \sin\Phi}{N_h^\uparrow + N_h^\downarrow}. \tag{5.19}$$

However, in experiment one usually does not have 4π coverage. This is true also for HERMES since the HERMES detector consists of two detector parts, top and bottom halves. As the result, the azimuthal angle distribution of detected hadrons contains the geometrical effect of the detector as shown in Fig. 5.2. The ϕ_S distribution shows a cosine-distribution because the spin direction of the target always points upward or downward in HERMES coordinate system and the scattered lepton is not detected in $\phi_S = \pi/2, 3\pi/2$ region.

For instance, let us consider only Sivers and Collins asymmetries. In this case, the asymmetry in 4π geometry is

$$A_{UT}^{(4\pi)} = a_{\mathcal{S}} \cdot \sin(\phi - \phi_S) + a_{\mathcal{C}} \cdot \sin(\phi + \phi_S), \tag{5.20}$$

where $a_{\mathcal{S}}$ and $a_{\mathcal{C}}$ are the Sivers and Collins asymmetries. Here, for the purpose of explanation, we introduce an acceptance function $\varepsilon(\phi, \phi_S)$ [1]. Using

[1]The acceptance function should be described in yield level not in asymmetry level, because the acceptance effect modifies the number of hadrons produced in 4π geometry depending on various kinematic.

this acceptance function, the measured asymmetries is expressed as

$$A_{UT}^{(Acc)} = a_{\mathcal{S}} \cdot \sin(\phi - \phi_S) \cdot \varepsilon(\phi, \phi_S) + a_{\mathcal{C}} \cdot \sin(\phi + \phi_S) \cdot \varepsilon(\phi, \phi_S). \quad (5.21)$$

From Fig. 5.2, the acceptance function can be expressed as follows,

$$\varepsilon(\phi, \phi_S) = \varepsilon^{\phi}(\phi)\varepsilon^{\phi_S}(\phi_S), \quad (5.22)$$

$$\varepsilon^{\alpha}(\alpha) = \left(\sum_{k=0} \varepsilon_k^{\alpha} \cos(k\alpha) + \sum_{l=0} \varepsilon_l^{\alpha} \sin(l\alpha) \right), \quad \alpha = \phi, \phi_S. \quad (5.23)$$

From this acceptance function, some additional non-vanishing factors appear in projected asymmetries. In case of $a_{\mathcal{S}} = 0$ (no Sivers asymmetry) in Eqs. (5.20) and (5.21), the $\sin(\phi - \phi_S)$ projected Sivers asymmetry can be non-zero because the Collins term Eq. (5.17) is modified by the acceptance function and makes non-zero terms,

$$\begin{aligned}
[\text{Eq. (5.17)}] \quad \times \quad & \varepsilon(\phi, \phi_S) \\
= \quad & d\sigma_{\mathcal{C}} \int d\phi \; d\phi_S \left[-\frac{1}{2}(\cos\phi - \cos\phi_S) \right] \\
& \times \left(\sum_{k=0} \varepsilon_k^{\phi} \cos(k\phi) + \sum_{l=0} \varepsilon_l^{\phi} \sin(l\phi) \right) \\
& \times \left(\sum_{m=0} \varepsilon_m^{\phi_S} \cos(m\phi_S) + \sum_{n=0} \varepsilon_n^{\phi_S} \sin(n\phi_S) \right) \\
= \quad & -\frac{1}{2} d\sigma_{\mathcal{C}} \int d\phi \; d\phi_S \left(\varepsilon_0^{\phi}\varepsilon_0^{\phi_S} + \varepsilon_1^{\phi}\varepsilon_0^{\phi_S} \cos^2\phi \; + \cdots \right)
\end{aligned}$$

Hence, even if there is no Sivers effect, the projection method can give non-zero Sivers asymmetries.

Indeed, we have generated asymmetry with weight for a test; $w_{UT} = 0.0 \sin(\phi - \phi_S) + 0.5x \sin(\phi + \phi_S)$, where other terms are set to $w_{O1,2,3} = 0$. Using the detected hadrons in the HERMES acceptance, the reconstructed Sivers asymmetry according to the projection-method Eq. (5.19) becomes non-zero value as shown in Fig. 5.3.

This acceptance effect can be corrected for if complete knowledge on the acceptance function is available. However the acceptance function is not as simple as presented in Eq. (5.23). For example the kinematical coverage in the azimuthal angles can depend on the scattering angle θ, thus the acceptance function is not only a function of ϕ and ϕ_S, but also of x and other kinematic variables.

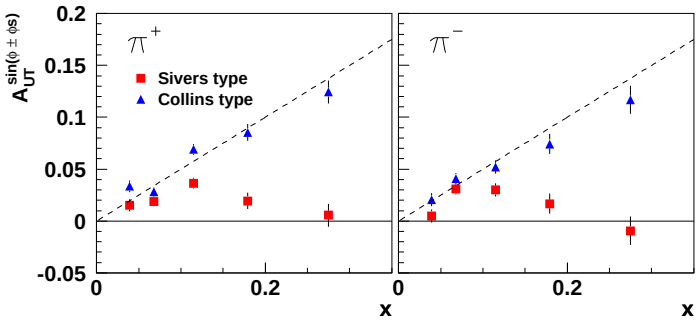

Figure 5.3: Reconstructed Collins (triangle) and Sivers (square) asymmetries of π^+ (left panel) and π^- (right panel) with projection method using Monte Carlo dataset. The asymmetries are obtained with the weight (Eq. (5.11)) $w_C(x) = 0.5 \cdot x$ for Collins asymmetry and no Sivers asymmetry $w_S(x) = 0.0$. In the plot, the dashed line indicates generated asymmetry.

Two dimensional fit-method

The two azimuthal angles, ϕ and ϕ_S, are independent kinematic variables. However due to the limited acceptance, they are not independent as mentioned above. To avoid the complication of the acceptance effect, there is an alternative method, *fit-method*. In this section, a test of the fit-method using Monte Carlo dataset is described.

For the fit-method, detected hadrons are accumulated in ϕ and ϕ_S bins with the relevant kinematic weigh $\mathcal{W}$. Then the asymmetries are obtained as follows,

$$A_{UT}^h(\phi, \phi_S) = \frac{\sum_i^{N_h^\uparrow(\phi,\phi_S)} \mathcal{W}_i(\phi, \phi_S) - \sum_i^{N_h^\downarrow(\phi,\phi_S)} \mathcal{W}_i(\phi, \phi_S)}{N_h^\uparrow(\phi, \phi_S) + N_h^\downarrow(\phi, \phi_S)} \tag{5.24}$$

$$= \frac{d\sigma_{UT}(\phi, \phi_S)}{d\sigma_{UU}(\phi, \phi_S)} \tag{5.25}$$

The asymmetries are obtained in two-dimensional distribution in ϕ and ϕ_S as shown in Fig. 5.4. This fit-method gives the *amplitude* of the each azimuthal dependence.

The obtained two dimensional asymmetries are fitted with respective sine-functions. The asymmetry as function of x is then obtained by searching

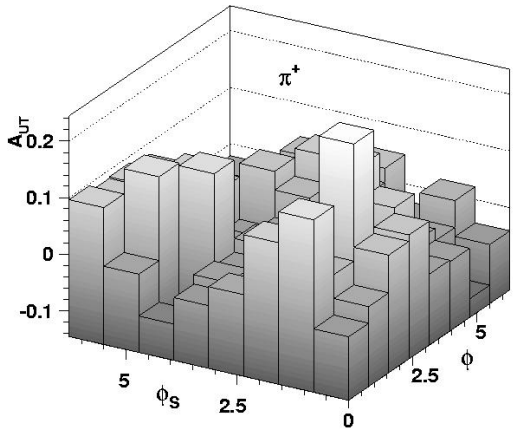

Figure 5.4: Two dimensional asymmetry for a x-bin.

minimum chi-square value defined as,

$$\chi^2(x_k) \equiv \sum_{i,j=1}^{i,j=N_{\phi,\phi_S}} \left(\left[A^h_{UT}(x_k,\phi_i,\phi_{S,j}) - \mathcal{F}(x_k,\phi_i,\phi_{S,j}) \right] \frac{1}{\delta A^h_{UT}(x_k,\phi_i,\phi_{S,j})} \right)^2 \tag{5.26}$$

where δA^h_{UT} is statistical uncertainties of two dimensional asymmetry. $\mathcal{F}$ is the fit function which is defined as follows,

$$\begin{aligned} \mathcal{F}(x_k,\phi_i,\phi_{S,j}) \equiv & A_{\mathcal{S}}(x_k)\cdot\sin(\phi_i-\phi_{S,j}) \\ & +A_{\mathcal{C}}(x_k)\sin(\phi_i+\phi_{S,j}) \\ & +A_{\mathcal{O}1}(x_k)\sin(3\phi_i-\phi_{S,j}) \\ & +A_{\mathcal{O}2}(x_k)\sin(2\phi_i-\phi_{S,j}) \\ & +A_{\mathcal{O}3}(x_k)\sin(\phi_i) \\ & +\text{const.} \end{aligned} \tag{5.27}$$

where $A_{\mathcal{T}}$ ($\mathcal{T}=\mathcal{S},\mathcal{C},\mathcal{O}1,\mathcal{O}2,...$) are the fit parameters, N_{ϕ,ϕ_S} indicates the number of bins in ϕ and ϕ_S.

Fig. 5.5 shows results of the same test as Fig. 5.3. For this test, the fit parameters $A_{\mathcal{O}i}$ ($i=1\sim3$) are not used. As one can see in Fig. 5.5, the acceptance effect is clearly suppressed and zero Sivers asymmetries are well reconstructed even in presence of large Collins type asymmetries. As a similar test, several types of x dependence for each asymmetries are tested in Fig. 5.6.

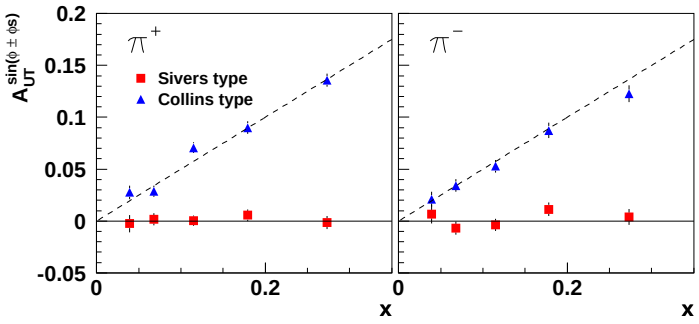

Figure 5.5: Comparison of reconstructed asymmetries with fit-method using Monte Carlo dataset. Monte Carlo dataset was obtained with $w_{\mathcal{C}} = 0.5 \cdot x$ for Collins asymmetry (triangle) and no Sivers asymmetry (square). In the plot, the dashed line indicates generated asymmetry.

From the above tests, it is concluded that the fit method works well to reconstruct true asymmetries as far as mixing of two types of asymmetries, Collins and Sivers asymmetries, is concerned.

5.2.3 Higher Twist Contributions

As presented in Eq. (5.7), other sine- and cosine-dependent terms, including higher twist terms, appear in the measured asymmetry. But up to now there are no reliable data available about size and sign of the terms. Therefore it is needed to test and confirm that the reconstruction method can eliminate those terms.

For the test, asymmetries are generated with

$$\begin{aligned} w_{UT} = {} & 0.5 \cdot x \cdot \sin(\phi - \phi_S) && \text{Sivers} \\ & -0.5 \cdot x \cdot \sin(\phi + \phi_S) && \text{Collins} \\ & +0.3 \cdot x \cdot \sin(3\phi - \phi_S) && \text{Other leading twist term} \\ & +0.2 \cdot x \cdot \sin(2\phi - \phi_S) \\ & -0.1 \cdot x \cdot \sin(\phi) && \text{Higher twist terms.} \end{aligned} \tag{5.28}$$

Fig. 5.7 shows results obtained with the fit-method using fit parameter of only the Sivers and Collins terms, neglecting the others. The results show some discrepancies especialy in the highest x bin. However, if we perform the fit with complete parameter set, the discrepancies vanish as shown in Fig. 5.8. The fit results of other sine terms are also shown in lower panel of Fig. 5.8.

The generated other sine modulations than the Sivers and Collins terms

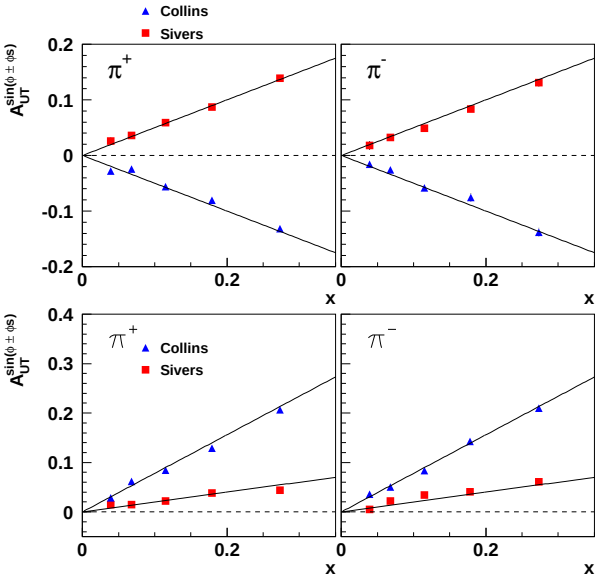

Figure 5.6: Upper plots show the extracted Collins (triangle) and Sivers (square) asymmetries from the Monte Carlo data generated with weight $w_{UT} = 0.5x\sin(\phi - \phi_S) - 0.5x\sin(\phi + \phi_S)$. Lower plots are similar but the Monte Carlo data obtained with different x dependence, $w_{UT} = 0.2x\sin(\phi - \phi_S) + 0.8x\sin(\phi + \phi_S)$. In the plot, the solid line indicates the generated asymmetry. Monte Carlo dataset was used.

are not reproduced as shown in lower panel of Fig. 5.8. But the Sivers and Collins asymmetries are well reproduced.

Unpolarized azimuthal angle dependence

In addition to the sine modulations as discussed above, another azimuthal angle dependence can be considered [35, 36]. The terms appear in unpolarized cross section as $\cos(n\phi)$.

Even if we neglect the higher twist terms, there is $\cos(2\phi)$ term at leading twist as mentioned in Section 2.4.2. From recent theoretical prediction in [70], the magnitude of unpolarized $\cos(2\phi)$ is small compared to Sivers asymmetry. However, the unpolarized azimuthal dependence could make unexpected behavior because this appears in denominator of the asymmetry.

In this section, as an example, $\cos(2\phi)$ ($n = 2$) dependence will be tested. To test the unpolarized azimuthal dependence, the asymmetry is generated

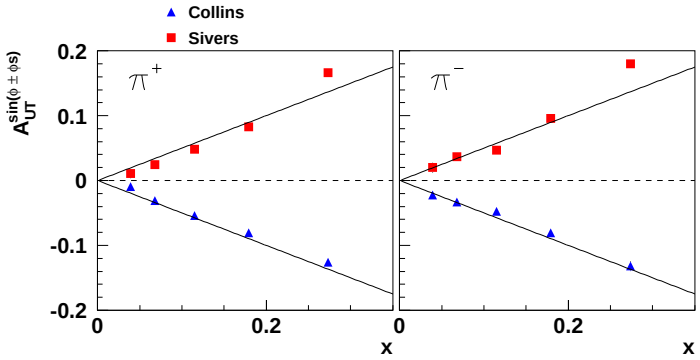

Figure 5.7: Extracted Sivers (square) and Collins (circle) asymmetries neglecting other sine terms. The Monte Carlo dataset generated with the weight Eq. (5.28) was used. The solid lines indicate the generated asymmetries.

with the weight,

$$w^{\pm} = w_u(1 + w_{UU}(x,\phi) \pm w(x,\phi,\phi_S)), \tag{5.29}$$

$$w_{UU}(x,\phi) \equiv w_U(x) \cdot \cos(2\phi). \tag{5.30}$$

The asymmetry is then (cf. Eq. (5.14)),

$$A_{UT}(x,\phi,\phi_S) = \frac{\sum_i^{N^u} w_{UT}^i(x,\phi,\phi_S)}{N^u + \sum_i w_U^i \cos(2\phi)}. \tag{5.31}$$

Hence the $\cos(2\phi)$ appears only in denominator of the asymmetry. The fit function $\mathcal{F}$ is no longer a linear function,

$$\begin{aligned}\mathcal{F}(x_k,\phi_i,\phi_{S,j}) = \frac{1}{1 + A_{\mathcal{O}0}(x_k)\cos(2\phi_i)} \\ \times \{A_{\mathcal{S}}(x_k) \cdot \sin(\phi_i - \phi_{S,j}) \\ + A_{\mathcal{C}}(x_k)\sin(\phi_i + \phi_{S,j}) \\ + \text{const.}\}\,.\end{aligned} \tag{5.32}$$

As mentioned above, it is expected that the magnitude of $\cos(2\phi)$ term is smaller than the Sivers asymmetry [70]. For this test, the asymmetries are generated with the following weights,

$$w_{UU}(x,\phi) = -0.2x\cos(2\phi) \tag{5.33}$$

$$\begin{aligned}w_{UT}(x,\phi) = 0.5x\sin(\phi - \phi_S) \\ -0.5x\sin(\phi + \phi_S).\end{aligned} \tag{5.34}$$

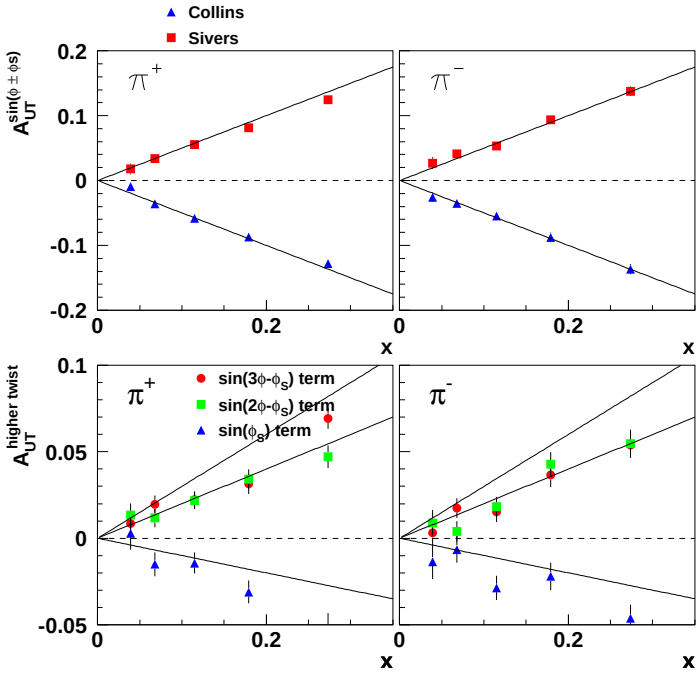

Figure 5.8: Extracted asymmetries. These results are obtained using full parameter sets given in Eq. (5.27). In the top plots, the Sivers (square) and Collins (circle) asymmetries are displayed together with generated asymmetry (solid line). In the lower plots, extracted higher twist asymmetries are shown with respective marks; $\sin(3\phi - \phi_S)$ (circle), $\sin(2\phi - \phi_S)$ (square) and $\sin(\phi)$ (triangle).

The results obtained with fit function Eq. (5.32) are shown in Fig. 5.9. As shown in Fig. 5.9, the unpolarized cosine term cannot be reproduced But the Sivers and Collins asymmetries are well reconstructed.

Here one more test has to be performed; if there is NO real Sivers and/or Collins effect, they could be transferred from the unpolarized azimuthal dependence. It is then possible that the extracted Sivers and Collins asymmetries are non-zero. For this test, the asymmetries are generated with

$$w_{UT} = 0.0 \sin(\phi + \phi_S) - 0.5x \sin(\phi + \phi_S), \tag{5.35}$$

$$w_{UU} = 0.2x \cos(2\phi). \tag{5.36}$$

The results obtained with fit function of Eq. (5.32) are presented in Fig. 5.10. It is confirmed that the Sivers asymmetry is zero: no transfer from the unpolarized azimuthal dependence is observed.

As a conclusion, the two dimensional fit-method is reliable method to

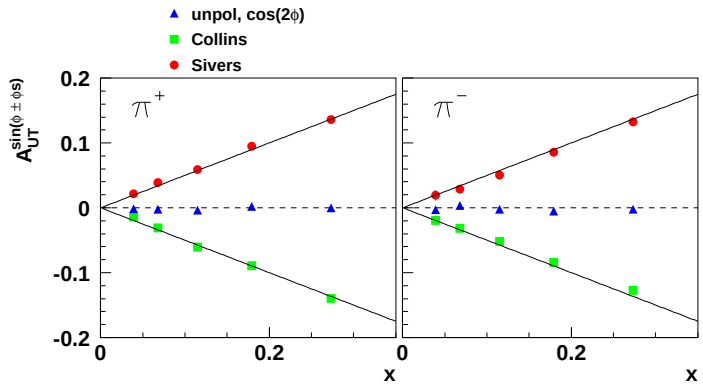

Figure 5.9: Extracted asymmetries with fit-method including unpolarized azimuthal dependence; $\cos(2\phi)$. Monte Carlo asymmetry dataset generated with weight Eqs. (5.33) and (5.34) are used.

reconstruct the asymmetries. So this method will be adopted in the data analysis. However from the above tests, the higher twist terms can influence the extracted Siver and Collins asymmetries. Thus similar test in the data analysis has to be performed.

5.2.4 Binning Effect

There is uncertainty of extracted asymmetries due to finite bin-size, so-called binning effect. In the above tests, 8 bins of ϕ and ϕ_S are used. This is basically determined to match the statistics of the experimental data as we will see in Section 5.3.

In any analyses using finite bin size, the binning effect is involved. For example, when the data sample has $\sin(\phi)$ dependence, the evaluated *height* of $\sin(\phi)$ in a finite bin, $[\phi_i, \phi_{i+1}]$, corresponds to an averaged value $\langle \sin(\phi) \rangle_{i,i+1}$,

$$\langle \sin(\phi) \rangle_{i,i+1} \equiv \frac{\int_{\phi_i}^{\phi_{i+1}} d\phi \ \sin(\phi)}{|\phi_i - \phi_{i+1}|}. \tag{5.37}$$

The true *height* of the $\sin(\phi)$ at the center of the bin $[\phi_i, \phi_{i+1}]$ is given by $\sin(\{\phi_i + \phi_{i+1}\}/2)$. As the results, $\langle \sin(\phi) \rangle_{i,i+1}$ and $\sin(\{\phi_i + \phi_{i+1}\}/2)$ are not consistent value depending on the bin-size $[\phi_i, \phi_{i+1}]$. The difference between $\langle \sin(\phi) \rangle_{i,i+1}$ and $\sin(\{\phi_i + \phi_{i+1}\}/2)$ can be computed mathematically, and 8 bins used in this analysis give about 5% uncertainty. We call it scale uncertainty. The scale uncertainty decreases of course as the size of $[\phi_i, \phi_{i+1}]$ decreases. If we take 10 bins, it is $\sim 3\%$.

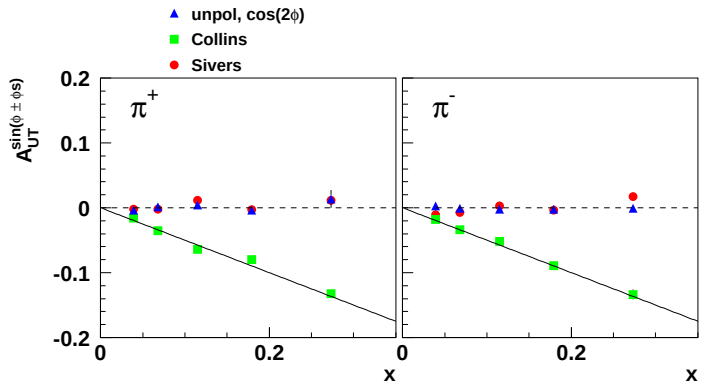

Figure 5.10: Extracted asymmetries with fit-method including $\cos(2\phi)$ unpolarized azimuthal dependence with no Sivers asymmetry. Monte Carlo asymmetry dataset generated with weight given by Eqs. (5.35) and (5.36) is used.

However this simple discussion assumes the infinite statistics, so that we will test the binning effect in the real data analysis.

5.2.5 Neutral Pion Asymmetry

In addition to charged pions, the neutral pion, π^0, is useful for interpretation of the observed asymmetry in quark parton model. In this section some tests for extracting π^0 asymmetry will be described.

The neutral pions are identified by the detection of two photons in the electromagnetic calorimeter. The reconstructed energy for each photon is required to be at least 1.0 GeV. Also the hit position on the calorimeter is looked at, since incoming photon makes a cluster which typically spreads to 9 calorimeter blocks. The hit has to be well inside the calorimeter blocks. Finding the cluster with no track in the tracking detectors eliminates charged track contributions. The reconstructed photon-pair invariant mass $M_{\gamma\gamma}$ distribution, Fig. 5.11, shows a clear π^0 mass peak with mass resolution of about 0.012 GeV (*cf.* [71, 72]). Neutral pion candidates are selected in the range of invariant mass of 0.10 GeV $< M_{\gamma\gamma} <$ 0.17 GeV.

To determine the number of neutral pions, a fit to the data with a Gaussian and a second order polynomial was applied.

In order to test the π^0 reconstruction, the number of *true* π^0 in reconstructed π^0 data sample is evaluated using Monte Carlo simulation including detector simulation. The results are presented in Fig. 5.12. The upper panel of Fig. 5.12 shows the number of *true* π^0 and that of π^0 evaluated with Gaus-

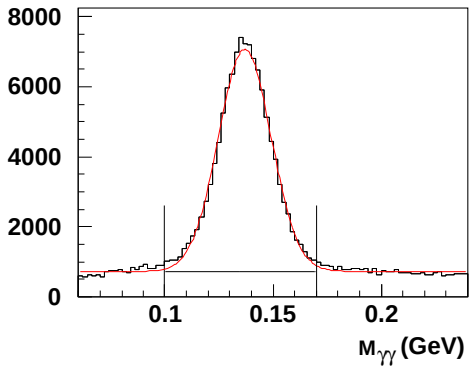

Figure 5.11: Invariant mass distribution of 2γ in a x-bin. Result of a fit using Gaussian function plus a second order polynomial (red line) is superimposed.

sian fit using the same dataset. In the lower panel of Fig. 5.12, the ratio of them is presented. From these results, the neutral pions can be identified with more than 97% efficiency.

In principle, the π^0 asymmetry can be determined from the number of π^0 evaluated with Gaussian fit. It is however more complicated, since background of π^0 can also make non-zero asymmetry. There are some possible sources to make an asymmetry of the background, e.g. photons from QED radiative processes. However, at the moment, no reliable information is available on the background asymmetry. Thus we make one assumption that the background asymmetry outside of π^0 window and inside of π^0 window are the same.

In order to evaluate background asymmetry, background window is defined taking the 25 MeV sidebands of π^0 window, 0.075 GeV $< M_{\gamma\gamma} <$ 0.1 GeV and 0.17 GeV $< M_{\gamma\gamma} <$ 0.195 GeV. The asymmetry of the background $A_{bg}^{\sin(\phi\pm\phi_S)}$ is first determined using the events in background window. The π^0 asymmetry $A_{corr}^{\sin(\phi\pm\phi_S)}$ is obtained after correcting for this backgroung asymmetry using the following relation,

$$A_{corr}^{\sin(\phi\pm\phi_S)} = A_{\pi_c^0}^{\sin(\phi\pm\phi_S)} \cdot \left(\frac{N_{tot}}{N_{\pi^0}}\right) - A_{bg}^{\sin(\phi\pm\phi_S)} \cdot \left(\frac{N_{bg}}{N_{\pi^0}}\right) \qquad (5.38)$$

$$N_{tot} = N_{bg} + N_{\pi^0},$$

where $A_{\pi_c^0}^{\sin(\phi\pm\phi_S)}$ is the asymmetry evaluated with π^0 candidates in the π^0 window, and N_{π^0} is the evaluated number of π^0 using a Gaussian fit, N_{tot} is

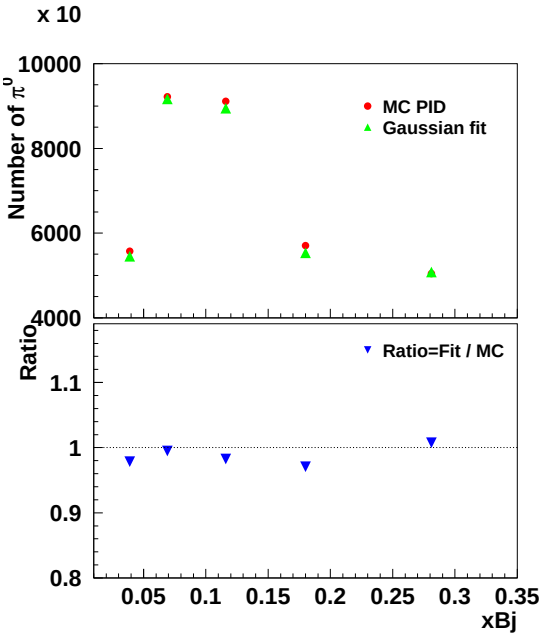

Figure 5.12: Comparison of a number of π^0 evaluated in each x-bin with a Gaussian fit and true particle type given by Monte Carlo (MC PID). The identical Monte Carlo dataset was used in both cases. In the upper panel, the triangle (circle) is the results evaluated with fit (MC PID). The lower panel shows ratio of the number of reconstructed and true π^0s.

the total number of events in the π^0 window.

5.3 Data Analysis

In this section analyses of real data are described. The data used in this analysis were taken between August of 2002 to February of 2003, with the transversely polarized hydrogen target and the unpolarized positron beam.

5.3.1 Event Selection

All geometrical and kinematical cuts used for track and event selection are listed in Table 5.1. Most of the geometrical constraints are to avoid systematic effects at the edge of spectrometer. Especially criteria of hit position on the calorimeter requires that a whole electromagnetic shower is contained within the calorimeter. The sum of signals in the neighboring lead glass

Table 5.1: Summary of the criteria used in this analysis.

PID Cuts		
- Leptons:	$(\mathrm{PID}_3+\mathrm{PID}_5) > +1.0$	
- Hadrons:	$(\mathrm{PID}_3+\mathrm{PID}_5) < -1.0$	
- Neutral pions:	$1.0 < E_{cluster}$	[GeV]
	$0.1 < M_{\gamma\gamma} < 0.17$	[GeV/c^2]
Fiducial Volume Cuts		
Geometry cuts	$-18 \leq z_{vert} \leq 18$	[cm]
for charged	$d_{vert} \leq 0.75$	[cm]
tracks	$-175 \leq x_{Calo} \leq 175$	[cm]
	$30 \leq \lvert y_{Calo}\rvert \leq 108$	[cm]
Geometry cuts	$-125 \leq x_{Calo} \leq 125$	[cm]
for clusters	$33 \leq \lvert y_{Calo}\rvert \leq 105$	[cm]
Kinematic Cuts		
	$3.5 \leq E_{Calo}$	[GeV]
DIS	$1.0 \leq Q^2$	[(GeV/c)^2]
lepton kinematic	$0.1 \leq y \leq 0.85$	
cuts	$10.0 \leq W^2$	[GeV^2]
	$0.023 \leq x \leq 0.4$	
Hadron kinematic	$0.02 < \theta_{\gamma h}$	[rad]
cuts	$2 < P_h < 15$	[GeV/c]
	$0.2 < z < 0.7$	

blocks in the calorimeter has to be above 3.5 GeV-equivalent electromagnetic shower signal.

The first event selection is done by the physics trigger, which we called Trigger 21. It requires the detection of a scattered lepton. The leptons are identified with PID value, $\mathrm{PID}_3+\mathrm{PID}_5 > 1$. To identify the lepton originating from DIS, at the first level, it is required that the lepton track with the highest reconstructed momentum has the same charge as the beam lepton. After finding out the scattered lepton, kinematic variables, x, y, Q^2 and W^2, are computed, and DIS cuts are applied. The DIS event is defined as an event which satisfies a series of the DIS-specific criteria. The criteria on x and y are determined basically by limitation of kinematical acceptance. Upper limit of the fractional lepton energy transfer $y < 0.85$ reduces significantly the contribution by higher order QED radiative effect. A cut on squared four momentum of the virtual photon, $Q^2 \geq 1.0$ GeV^2 sets the scale for DIS. A large invariant mass of hadronic final state $W^2 \geq 10$ GeV^2 rejects events in a resonance region and improves the separation of the target and current fragmentations for semi-inclusive hadrons.

In the sample of tracks in coincidence with the DIS positron, the hadrons are identified with PID value $\mathrm{PID}_3 + \mathrm{PID}_5 < -1$. In the required hadron momentum range, the efficiency of particle identification with RICH detector for a charged pion reaches around 90%. The hadrons which passed the lower limit of hadron energy fraction $z \geq 0.2$ are further selected in the current fragmentation region with the W^2 cut. Upper limit of z eliminates non semi-inclusive DIS events, such as exclusive events since the exclusive events also generate asymmetry depending on azimuthal angle. $\theta_{\gamma^* h}$ is the angle between the direction of virtual photon and hadron. The requirement on $\theta_{\gamma^* h}$ is based on ϕ determination, since $\theta_{\gamma^* h} \sim 0$ means that the produced hadron is almost in the lepton scattering plane, in this case ϕ cannot be determined.

Finally, number of events which passed the criteria is summarized in Table 5.2.

5.3.2 Time Dependence of Data Sample

For the study of the azimuthal asymmetries, it is important to confirm experimental stability during the data taking. To see the stability of the experiment, time dependence of the data sample of semi-inclusive DIS events for each target spin state will be seen.

Ratio of number of π^+'s and semi-inclusive positrons as function of time is presented in Fig. 5.13. The semi-inclusive DIS positron requires at least one hadron in the HERMES acceptance. In the figure, unit of the time is

Table 5.2: Number of events used in this analysis.

	Number of events
DIS events	590,747
π^+	57,011
π^-	40,196
π^0	16,235

"fill" which is typically about 8 hours. As shown in Fig. 5.13, the ratio is basically constant, and the ratio for up and down target spin states are almost consistent within the statistical uncertainties in whole period of the data taking. No significant time dependence of the ratio is seen in whole period of the the data taking.

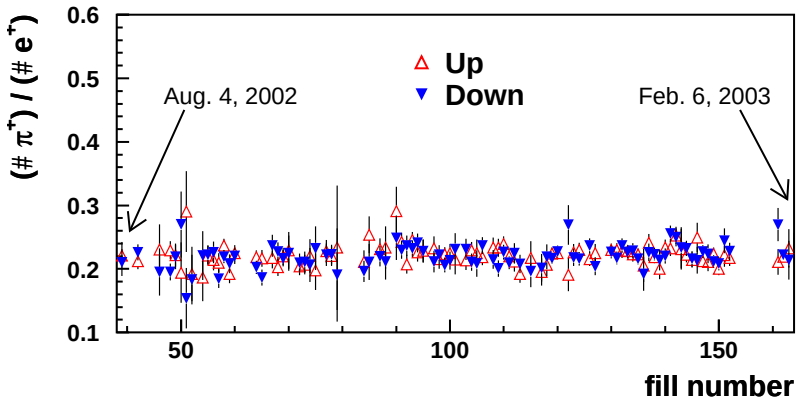

Figure 5.13: Ratio of semi-inclusive DIS π^+ and positron yields for up and down target spin states is shown as a function of fill.

As already mentioned in the previous section, the asymmetry $A_{UT}(\phi, \phi_S)$ is defined in Eq. (5.4). By looking at the azimuthal angle dependence as sine modulations, the Sivers and Collins asymmetries can be obtained. For the evaluation of the Sivers and Collins asymmetries, a large amount of statistics is required, so it is difficult to evaluate the time dependence of the asymmetries. However there is useful characteristic of the single azimuthal asymmetry. The cross section $\sigma^{\uparrow/\downarrow}$ integrated over azimuthal angles equals

to the unpolarized cross section $\sigma_{\mathcal{U}}$,

$$\begin{aligned}
\sigma^{\uparrow} &\equiv \int d\phi\ d\phi_S\ d\sigma^{\uparrow}(\phi,\phi_S) \\
&= \int d\phi\ d\phi_S\ \left[d\sigma_{UU}(\phi) + \sigma_{UT}(\phi,\phi_S)\right] \\
&= \sigma_{\mathcal{U}} + \int d\phi\ d\phi_S \left[d\sigma_{\mathcal{O}0}\cos(\phi) + d\sigma_{\mathcal{S}}\sin(\phi-\phi_S) + d\sigma_{\mathcal{C}}\sin(\phi+\phi_S) + ...\right] \\
&= \sigma_{\mathcal{U}}
\end{aligned}$$

Therefore the integrated asymmetry over the azimuthal angles should be zero,

$$\begin{aligned}
A_{UT} &\equiv \frac{1}{P}\frac{\int d\phi\ d\phi_S\ \left[N^{\uparrow}(\phi,\phi_S) - N^{\downarrow}(\phi,\phi_S)\right]}{\int d\phi\ d\phi_S\ \left[N^{\uparrow}(\phi,\phi_S) + N^{\downarrow}(\phi,\phi_S)\right]} && (5.39) \\
&= \frac{\sigma^{\uparrow} - \sigma^{\downarrow}}{\sigma^{\uparrow} + \sigma^{\downarrow}} = \frac{\sigma_{\mathcal{U}} - \sigma_{\mathcal{U}}}{\sigma_{\mathcal{U}} + \sigma_{\mathcal{U}}} && (5.40) \\
&= 0, && (5.41)
\end{aligned}$$

where P is the target polarization, N is the luminosity normalized particle yield. This integrated asymmetry corresponds to "false asymmetry" for azimuthal single spin asymmetry. If there is an asymmetry in the integrated asymmetry, it propagates to the Sivers and Collins asymmetry. So the integrated asymmetry is useful to check the time dependence of the asymmetry. Additionally, since the integrated asymmetry corresponds to simple yield asymmetry, the integrated asymmetry can be evaluated also for the scattered positron. Fig. 5.14 shows the integrated asymmetries A_{UT} for semi-inclusive DIS positron and π^+ as a function of fill. A constant fit was applied to the asymmetries, and the fit results are also shown in the plots. The integrated asymmetries for positron and π^+ are almost consistent with zero. Even if a linear fit is applied, the slope of the fit result is of the order of 10^{-4} per fill, so there is no significant time dependence.

5.3.3 Background Correction for Neutral Pions

The observed spectrum of invariant mass of 2γ is presented in Fig. 5.15 for each kinematical bin of x and z. The signal-to-noise (SN) ratio is almost constant at ~ 4 in every x-bins. In contrast to the x-dependence, the SN ratio decreases as z increases. Especially in the highest bin no background tail was found.

The background correction of π^0 asymmetry is evaluated from definition in Eq. (5.39). The background asymmetry was evaluated, and the results are

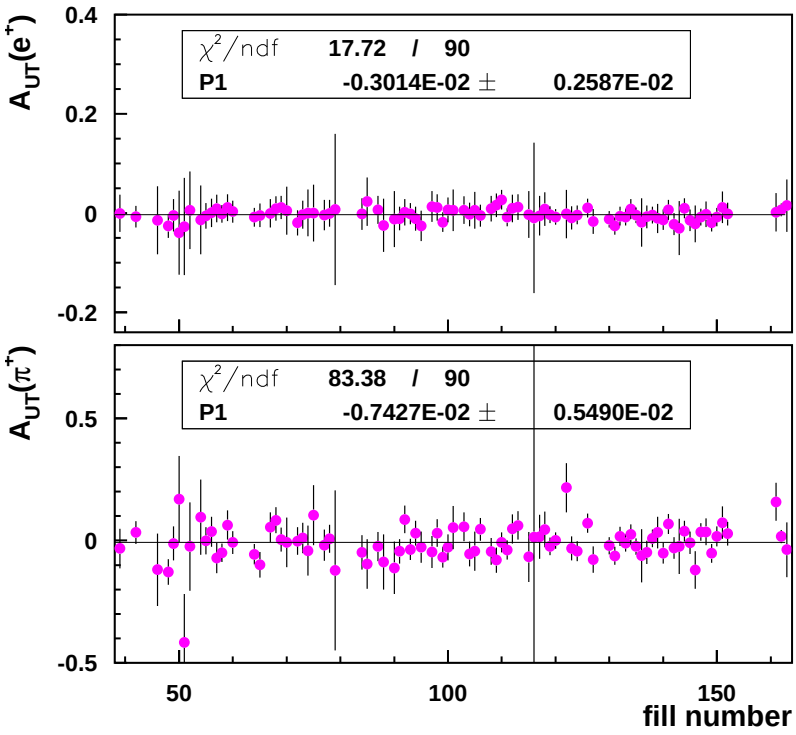

Figure 5.14: Integrated asymmetries for semi-inclusive DIS positron (upper plot) and π^+ (lower plot). In the plot, fit results are also shown.

shown in Fig. 5.16. As show in Fig. 5.16, the background asymmetries are compatible with zero within the statistical uncertainties.

5.3.4 Target Polarization

During the data taking period of 2002 and 2003, the average transverse polarization of target proton for up and down spin state is evaluated from detailed study with target polarimetry [73] to be $\langle P \rangle = 0.783 \pm 0.041$. This transverse polarization is defined in HERMES coordinate system, so the spin direction of the target is perpendicular to the beam direction. Thus the necessary information, in addition to the polarization, is the transverse spin component of the target with respect to the virtual photon direction. The transverse spin component S_T (see Fig. 5.1) can be computed with,

$$S_T = \frac{| \vec{S} \times \vec{q} |}{| \vec{q} |}$$

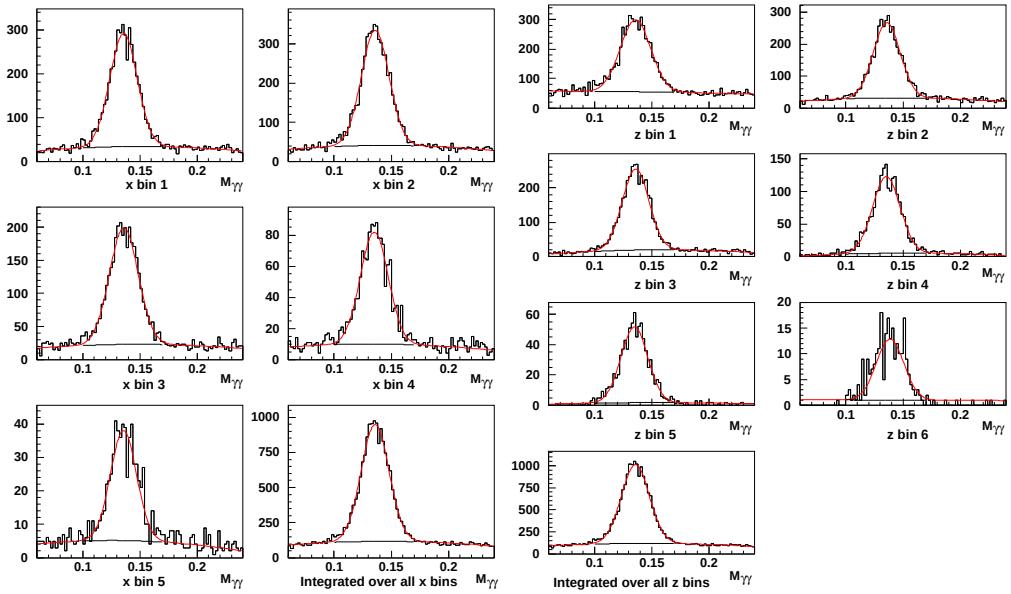

Figure 5.15: Observed 2γ invariant mass distributions for each x-bin (left) and z-bin (right). The bin edges are $x = 0.023, 0.05, 0.09, 0.15, 0.22, 0.4$ and $z = 0.2, 0.3, 0.4, 0.55, 0.7, 0.85, 1.0$.

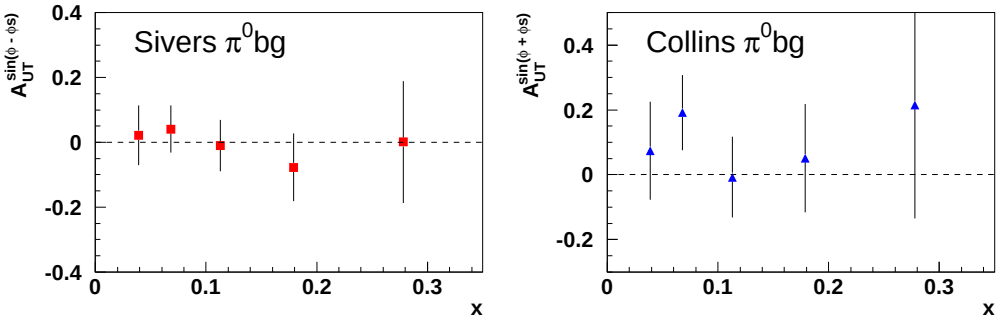

Figure 5.16: π^0 background asymmetries as function of x for Sivers type (left) and Collins type (right).

where $\vec{S}$ is polarization vector of the target, which is unit vector pointed out y direction in HERMES coordinate system. Figure 5.17 shows S_T evaluated on event-by-event basis. From Fig. 5.17, average transverse component is $\langle S_T \rangle = 0.997 \pm 0.034$. This means that the virtual photon is emitted almost perpendicular to the target polarization vector $\vec{S}$. Using $\langle S_T \rangle$, average transverse polarization with respect to the virtual photon, $\langle P \rangle \cdot \langle S_T \rangle$ is,

$$\langle P \rangle \cdot \langle S_T \rangle \quad = \quad 0.781 \pm 0.049 \tag{5.42}$$

As a conclusion, the transverse spin component and transverse polarization evaluated in HERMES coordinate are consistent within systematic uncertainties.

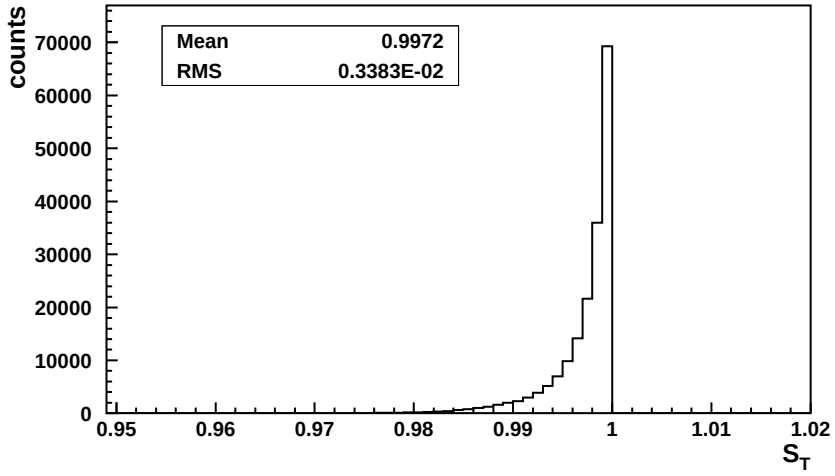

Figure 5.17: Transverse spin component S_T of the target with respect to the virtual photon direction.

5.4 Observed Sivers and Collins Asymmetries

The measured Sivers and Collins asymmetries with regard to virtual photon are presented in Fig. 5.19-5.22. The π^0 asymmetries are already corrected for the background with definition of Eq. (5.39). In each plot, error bars indicate statistical uncertainties, and the error band denotes systematic uncertainties which take into account the systematic uncertainties of target polarization.

The asymmetries are shown as a function of x and z, each kinematical binning is listed in Table 5.3.

Table 5.3: Binning definition of x and z.

x-bin	1	2	3	4	5
Upper limit	0.023	0.05	0.09	0.15	0.22
Lower limit	0.05	0.09	0.15	0.22	0.4
z-bin	1	2	3	4	
Upper limit	0.2	0.3	0.4	0.55	
Lower limit	0.3	0.4	0.55	0.7	

In this study the fit-method is employed to extract asymmetries, as has already been described in Section 5.1 and 5.2. Theoretical definition of the asymmetries, $\langle \mathcal{W} \sin\Phi \rangle_{UT}$, is presented in Eq. (5.15), and the extracted asymmetries with fit-method, i.e. amplitude of sinusoidal $A_{UT}^{\mathcal{W}\sin\Phi}$ are related to

$$\frac{1}{2} A_{UT}^{\mathcal{W}\sin(\phi\pm\phi_S)} = \Big\langle \mathcal{W} \sin(\phi \pm \phi_S) \Big\rangle_{UT}. \tag{5.43}$$

Hence the both unweighted and weighted asymmetries shown in Fig. 5.19-5.21 are divided by 2 for a later quark level interpretation.

Weighted Asymmetry

As mentioned in the previous section, to obtain the asymmetry which resolves the convolution integral on p_T and k_T, the weighted asymmetries are also extracted. For the purpose of resolving the convolution integral the *weight function*, $\mathcal{W}$, defined in Eq. (3.10) can be used. On the other hand in the experiment, we do not need z dependence of the asymmetries though it appears in Eqs. (3.11) and (3.15). Therefore in this analysis, the following weight functions are used instead of Eq. (3.10),

$$\mathcal{W} = \begin{cases} \dfrac{|\boldsymbol{P}_{h\perp}|}{zM_p} & : \text{Sivers} \\ \dfrac{|\boldsymbol{P}_{h\perp}|}{zM_h} & : \text{Collins} \end{cases} \tag{5.44}$$

In the later section of this chapter, we compare the weighted asymmetries obtained with the weight functions of Eq. (5.44) and with Eq. (3.10).

5.4.1 Collins Asymmetries

The observed virtual photon asymmetries of Collins type are shown in Fig. 5.18, 5.20 and Fig. 5.22. In Fig. 5.18, the asymmetries are displayed as a function of x. Unweighted and $(P_{h\perp}/zM_h)$-weighted asymmetries are presented separately.

As shown in Fig. 5.18 and 5.20, the Collins type asymmetries for charged pions are non-zero: π^+ asymmetry is positive and π^- asymmetry is negative. In contrast to charged pions, the π^0 asymmetry is small and slightly negative. Comparing unweighted and weighted Collins type asymmetries, we find that their shapes are similar. It should be noted that the magnitude of the weighted asymmetries are largely different from that of unweighted asymmetry due to the weight which contains the pion mass in the denominator.

The Collins asymmetries as a function of z and Q^2 are shown in Figs. 5.20, 5.22. They show no significant z- and Q^2-dependence.

5.4.2 Sivers Asymmetries

HERMES has measured for the first time Sivers type asymmetries in semi-inclusive DIS measurements. Figure 5.19 shows the results of Sivers type unweighted and $(P_{h\perp}/zM_p)$-weighted asymmetries for charged and neutral pions as a function of x. Figure 5.21 and 5.22 show the Sivers asymmetries as function of z and Q^2.

Compared to Collins asymmetries presented above, the statistical uncertainties on the Sivers asymmetries are smaller because in Sivers asymmetry the depolarization factor of the target with respect to virtual photon cancels out.

As presented in the figures, the observed Sivers type asymmetries for all types of pions are small. However especially π^+ and π^0 contain non-zero and positive asymmetry. Its statistical significance will be explained in deltails in a later section. In contrast, the asymmetry of π^- is compatible with zero within the statistical uncertainties.

The weighted asymmetries show almost consistent magnitude. As already mentioned before, these weighted asymmetries are theoretically clear objects since the parton distribution and fragmentation function are deconvoluted on transverse momentum p_T and k_T.

The asymmetries as a function of z and Q^2 are presented in Figs. 5.21 and 5.22. As shown in the figures, no significant z- and Q^2-dependence of asymmetries were found.

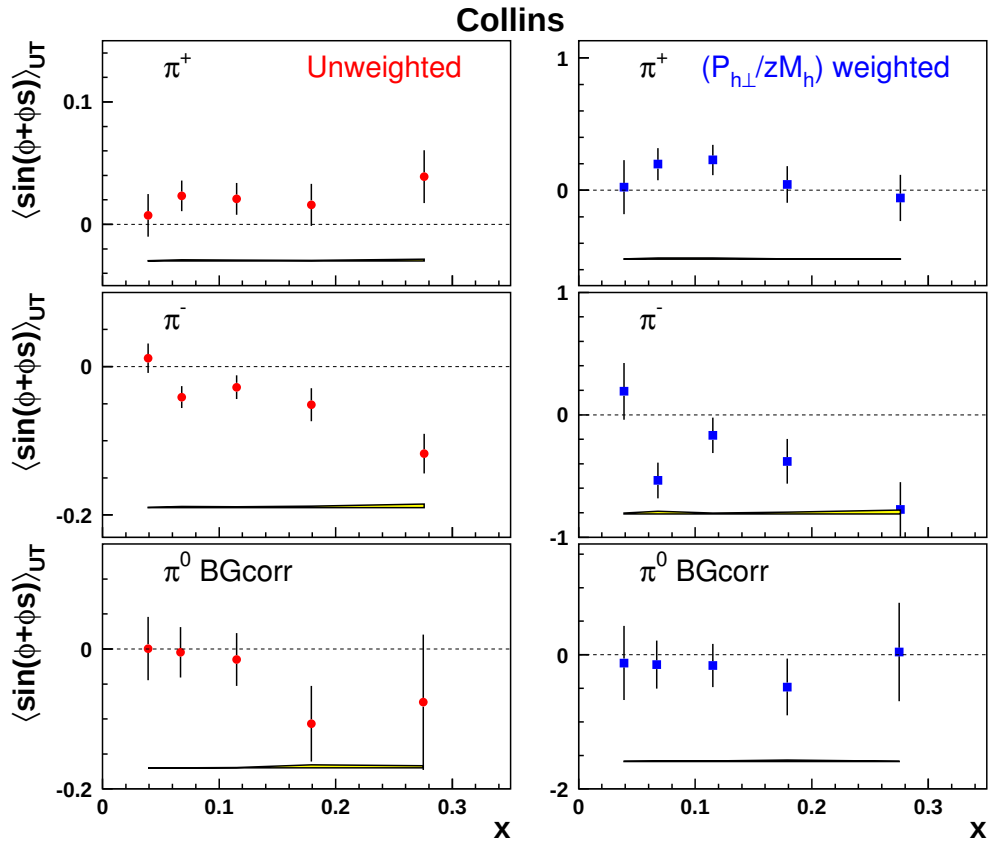

Figure 5.18: Observed Collins asymmetry. In left panels, the unweighted asymmetries are displayed as function of x. In right panels, the $(P_{h\perp}/zM_p)$-weighted asymmetries as function of x. The error bars indicate statistical uncertainties, and the error band denotes systematic uncertainties which take into account the systematic uncertainties of the target polarization.

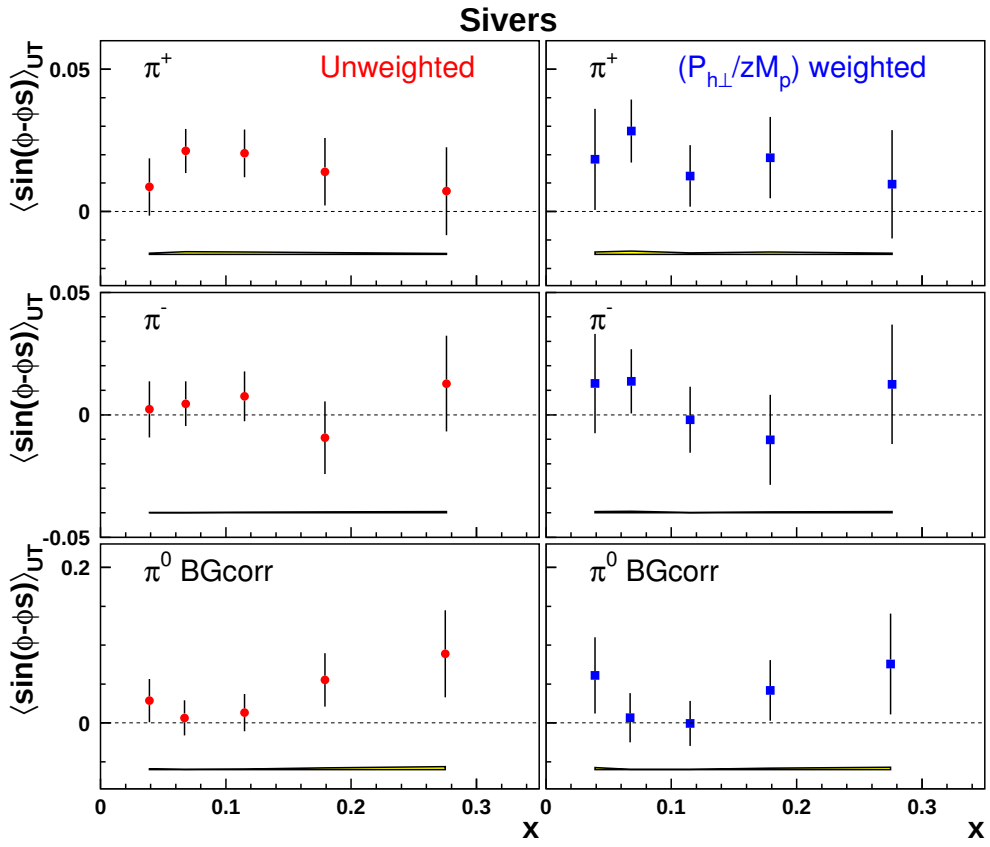

Figure 5.19: Observed Sivers asymmetry. In left panels, the unweighted asymmetries are displayed as function of x. In right panel, the $(P_{h\perp}/zM_p)$-weighted asymmetries as function of x. The error bars indicate statistical uncertainties, and the error band denotes systematic uncertainties which take into account the systematic uncertainties of the target polarization.

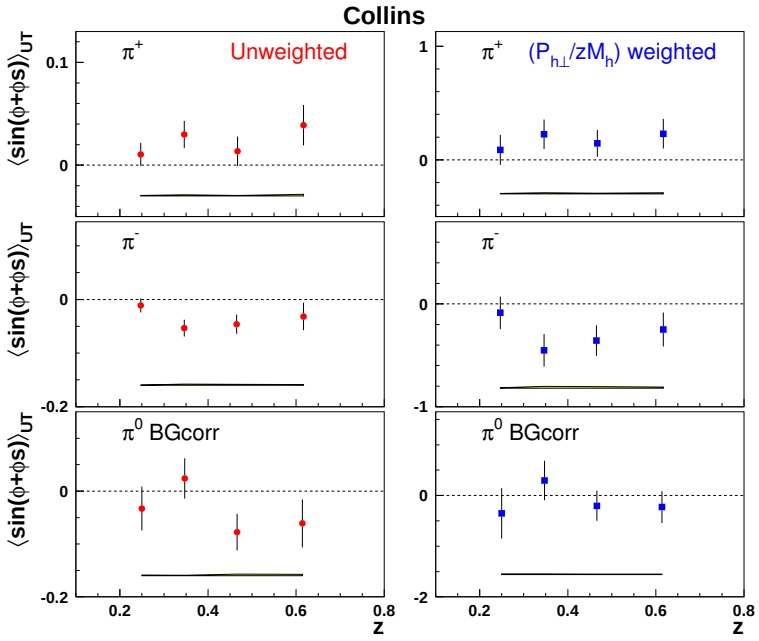

Figure 5.20: Observed Collins asymmetry. In left panels, the unweighted asymmetries are displayed as function of z. In right panels, the $(P_{h\perp}/zM_p)$-weighted asymmetries as function of z. The error bars indicate statistical uncertainties, and the error band denotes systematic uncertainties which take into account the systematic uncertainties of the target polarization.

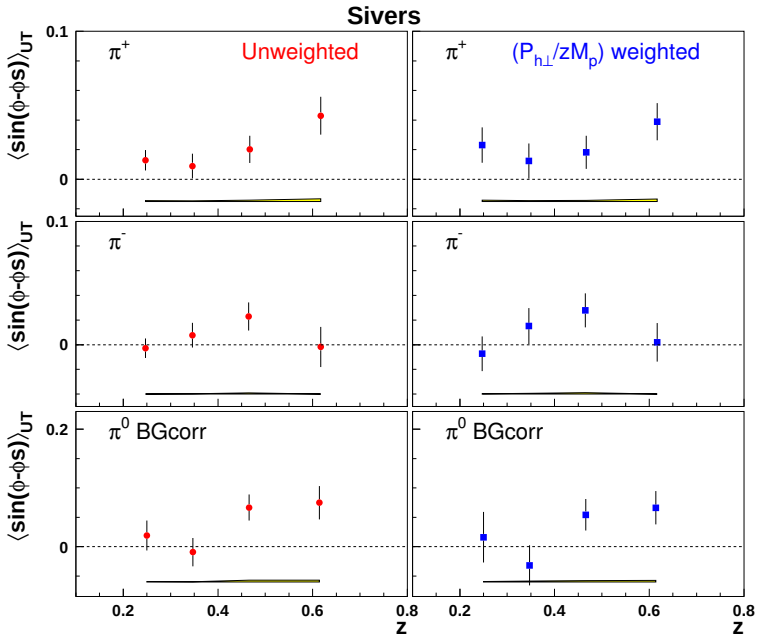

Figure 5.21: Observed Sivers asymmetry. In left panels, the unweighted asymmetries are displayed as function of z. In right panels the $(P_{h\perp}/zM_p)$ weighted asymmetries as function of z are shown. The error bars indicate statistical uncertainties, and the error band denotes systematic uncertainties which take into account the systematic uncertainties of the target polarization.

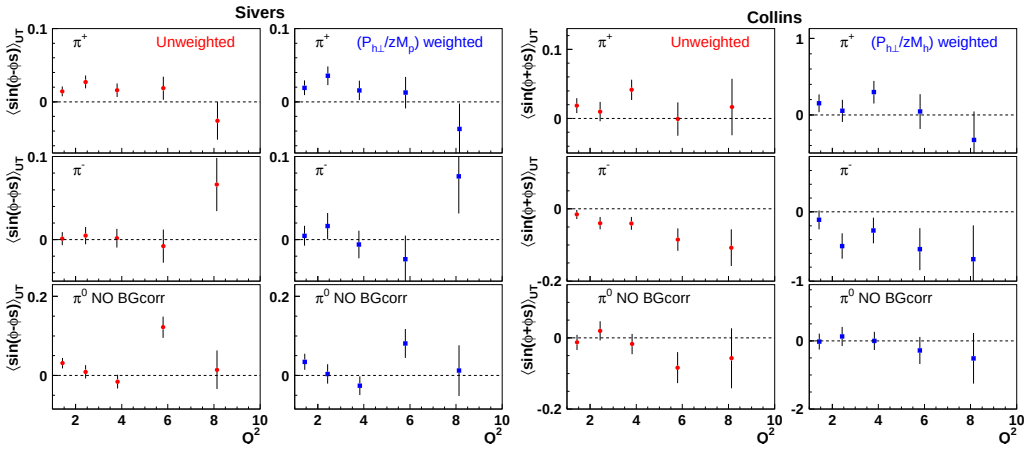

Figure 5.22: The observed Sivers and Collins type asymmetries as a function of Q^2.

5.5 Systematic Studies

In the following tests, only the results of the unweighted asymmetries are shown since the same results are obtained also for the weighted asymmetries. But in the Section 5.5.3, a specific test is given to the weighted asymmetry.

It has to be noted that the asymmetries shown in the following are $A_{UT}^{\sin(\phi\pm\phi_S)}$ so that the results of the asymmetries are twice larger than the asymmetries presented in the previous sections (see Eq. (5.43)).

5.5.1 Binning Effect

In this study, the fit method is employed. Roughly speaking, this method corresponds to searching for the maximum point of sinusoidal shape asymmetry. As already mentioned in Section 5.2.4, there is a binning effect due to the finite bin-size of ϕ and ϕ_S.

For a test of binning effect, the asymmetries were extracted using 10 bins in ϕ and ϕ_S instead of 8 bins. The results are shown in Fig. 5.23.

The mean values themselves are not largely changed but the statistical uncertainties are slightly enlarged. The 10 bins requires the two-dimensional asymmetries with $5 \times (10 \times 10) = 500$ elements including x bins. As the results, no-entry or entries only in one spin state bins appear especially at lowest and highest x bins. Such bins are eliminated in the χ^2 minimization. Nevertheless the two asymmetries obtained with the different binning are consistent within the statistical uncertainties.

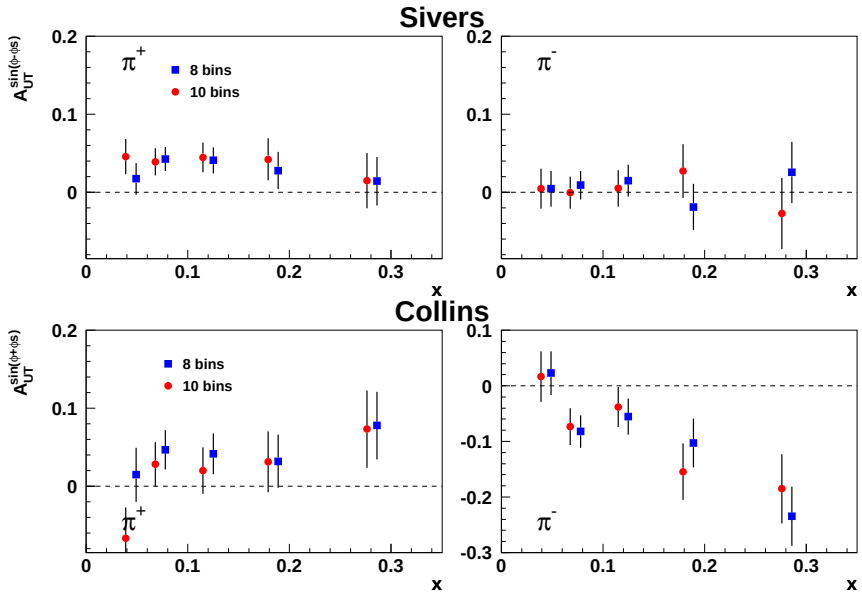

Figure 5.23: Extracted Sivers (top panel) and Collins (lower panel) asymmetries with different ϕ and ϕ_S binning, 10 bins (square) or 8 bins (circle).

5.5.2 Higher Twist Contributions

As described in Section 5.3, there is a possibility that the extracted Sivers and Collins asymmetries are influenced by higher twist terms due to limitation of detector acceptance. For the test, full parameter set of the fit function defined in Eq. (5.27) is used. The results are shown in Fig. 5.24 comparing the three parameter fit. As shown in Fig. 5.24, the extracted Sivers and Collins asymmetries with the different parameter sets are fully consistent within the statistical uncertainties. There is no significant differences between the different sets of parameters.

Unpolarized azimuthal dependence

A similar test to the above but a test for the unpolarized azimuthal dependence which appears in denominator was also carried out. As shown in Fig. 5.25, the results are fully consistent with those obtained without taking into account the unpolarized azimuthal dependence.

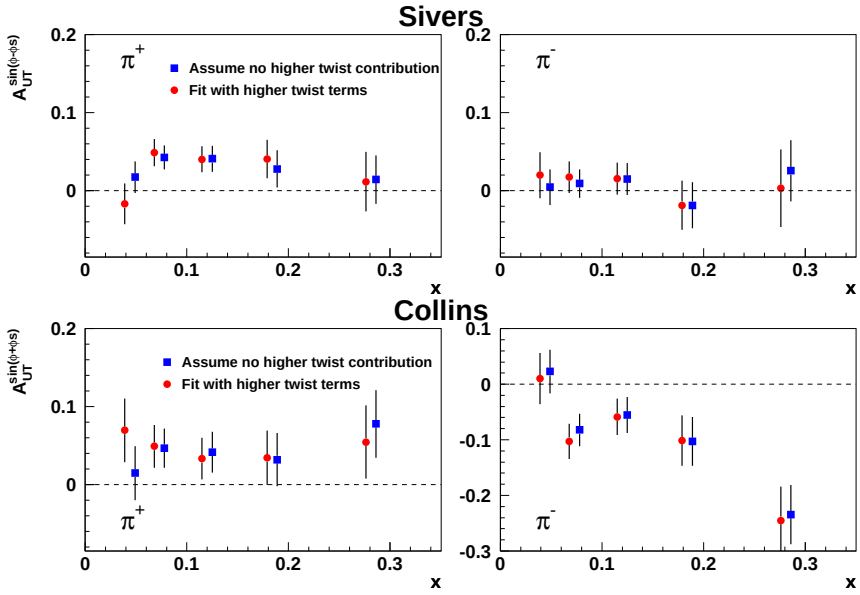

Figure 5.24: Extracted Sivers (top panel) and Collins (lower panel) asymmetries with different parameter sets, not taking into account the higher twist contributions (square), and taking into account the higher twist terms (circle) in Eq. (5.27).

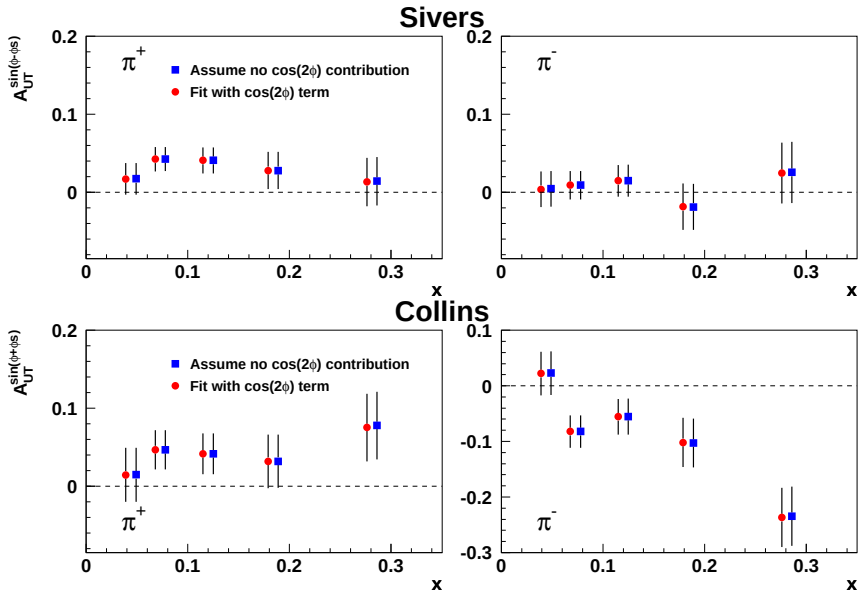

Figure 5.25: Extracted Sivers (top panel) and Collins (lower panel) asymmetries taking into account the unpolarized azimuthal dependence $\cos(2\phi)$ (circle) and without the term (square).

5.5.3 Weighted Asymmetries

As mentioned in the beginning of Section 5.4, the weighted asymmetries can be obtained with the different weight functions defined in Eq. (5.44) and Eq. (3.10). The difference between them is the z factor in the denominator.

The $(P_{h\perp}/zM)$-weighted and $(P_{h\perp}/M)$-weighted asymmetries should give consistent result,

$$A^{\frac{P_{h\perp}}{zM}\sin(\phi\pm\phi_S)} = \frac{1}{\langle z\rangle}\cdot A^{\frac{P_{h\perp}}{M}\sin(\phi\pm\phi_S)}. \tag{5.45}$$

Figure 5.26 shows the results. They give fully consistent results within the statistical uncertainties.

5.5.4 Diffractive Vector Meson Contribution

As theoretically pointed out in reference [74], "diffractive" processes, such as vector meson production, could affect the DIS cross section. The diffractive event involves a final state interaction. Such final state interaction (rescattering) leads to a shadowing effect and can affect the *measured* cross section. In the cross section of γp reaction, the major part of diffractive contribution

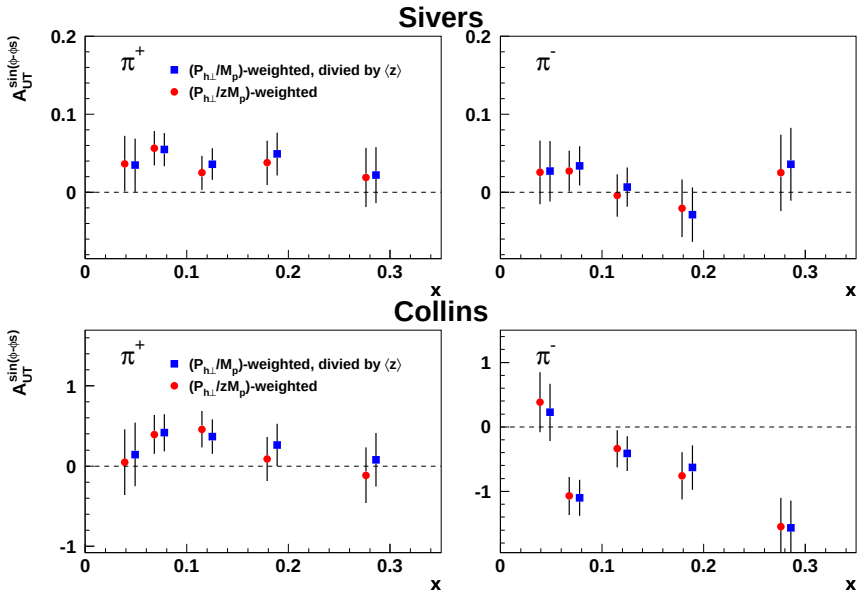

Figure 5.26: Comparison of weighted asymmetries using two types of weight functions, Eq. (5.44) : $P_{h\perp}/zM$ (circle) and Eq. (3.10) : $P_{h\perp}/M$ (square). The asymmetries evaluated with weight of Eq. (3.10) is divided by the mean values, $\langle z \rangle$, evaluated in each x-bin. Upper panel shows the Sivers type, and lower panel the Collins type.

comes from fluctuations of γ into a vector meson (ρ^0, ω). The vector meson can then proceeds to interact as a hadron with the target nucleon. This is not *real* DIS event.

The vector mesons decay into mainly two or more hadrons, e.g. $\rho^0 \rightarrow \pi^+\pi^-$, $\omega \rightarrow \pi^+\pi^-\pi^0$. If one has full geometrical coverage of detector, all pion decays from vector mesons can be identified by evaluating the invariant mass with two or more pions. However, in experiment one usually does not have 4π coverage. This is true also for HERMES. Due to the limitation of the geometrical coverage, only a single pion from many body decay of the vector meson is in acceptance in some cases. In this case, the pion cannot be identified as a diffractive event and it can influence the semi-inclusive data sample.

To evaluate the contamination in semi-inclusive data sample from the diffractive events, the PYTHIA Monte Carlo simulation [75] tuned for the HERMES experiment was used. In the simulation, the types of diffractive event processes can be identified, and the type of event is classified with process IDs:

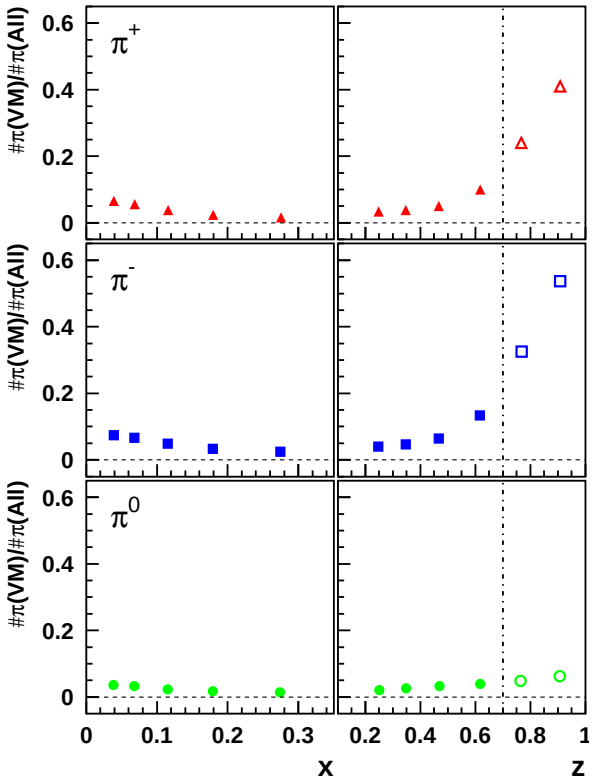

Figure 5.27: Ratio of exclusive vector meson in collected pion data sample which pass all kinematical and geometrical cuts. The ratios show for $\pi^{\pm}$ and π^{-} as labeled. Left plots present the ratio as a function of x, right plots present the ratio as function of z. For the extraction of the Sivers and Collins asymmetries, pions in highest two z-bins (open marks; $z > 0.7$) were not used. For x distribution, kinematical cut $z < 0.7$ was applied.

`91` : elastic $\gamma^* + p \to V + p$,

`92` : single diffractive $\gamma^* + p \to V + p$
(vector meson decay into hadrons $V \to h_1 + h_2 + ...$),

`93` : single diffractive $\gamma^* + p \to V + X$ (broken up proton).

Figure 5.27 shows the number of pions (#π(All)) which pass all kinematical and geometrical cuts and the number of pions originated from diffractive vector mesons (#π(VM)) in the same data sample. In this evaluation, diffractive vector mesons ρ^0 and ω are taken into account. As shown in the figure, the vector meson contamination is larger at higher z. From this reason, the kinematic cut of $z < 0.7$ is used for extraction of the Sivers and Collins

asymmetries. Looking at the pions originated from vector mesons, charged pions from ρ^0 and neutral pions from ω are dominant (*cf.* BR($\rho^0 \to \pi^+\pi^-$) $\sim$100%, BR($\omega \to \pi^+\pi^-\pi^0$) $\sim$89% [7]). From the results, contamination from the vector mesons in semi-inclusive data sample for charged pions is around 7% at maximum at lowest x bin. It is less than 4% for neutral pions.

In above discussion, spin dependence of the diffractive vector was not considered. There are theoretical predictions which suggest spin dependent diffractive vector meson. In particular reference [76] predicts non-zero and quite sizable "azimuthal asymmetry" for vector meson. The azimuthal asymmetry of the vector mesons can affect the semi-inclusive pion azimuthal asymmetries, such as Sivers and Collins asymmetry. If the momentum direction of one of pions from vector meson is the same as that of the parent vector meson, the pion can also make azimuthal asymmetry. If we know such azimuthal asymmetry A^{π}_{VM} of pions from the vector mesons, the background corrected semi-inclusive asymmetry A^{π}_{corr} can be evaluated as,

$$\begin{aligned} A^{\pi}_{corr} &= \frac{1}{1-d}A^{\pi}_{obs} - \frac{d}{1-d}A^{\pi}_{VM} \\ d &\equiv \frac{N_{VM}}{N_{All}}. \end{aligned} \tag{5.46}$$

where d corresponds to the ratio shown in Fig. 5.27. This way is similar to the π^0 background correction. As mentioned above, if we can reconstruct the invariant mass of the vector meson from two or more detected hadrons, we can correct the asymmetry according to Eq. (5.46). However, statistics of the present data sample is not sufficient to identify and evaluate Sivers and Collins like asymmetries of the vector meson.

There is some studies (e.g. reference [77]) of contribution to the single-spin asymmetry of semi-inclusive hadrons[2]. However theoretical study is not enough to give constraint on the vector meson contributions to the azimuthal asymmetries. How and how much the diffractive event affects the Sivers and Collins asymmetry is a theoretical open question at the present stage. Therefore, systematic errors which could arise due to these effects are not included in the following data analysis.

5.6 Comparison with Other Experiments

For a comparison of the observed asymmetries with results from other experiments, it is useful to use the unweighted asymmetry, since $A_{UT}^{\sin(\phi\pm\phi_S)}$ have

[2]Reference [77] shows an evaluation of diffractive event contribution to the semi-inclusive single-spin asymmetry A_{UL}.

value between -1 to 1 as usual asymmetry. Furthermore, in order to see the sign of the observed asymmetries explicitly, we evaluate *average* asymmetry over whole measured kinematic range. The results of averaged unweighted asymmetries are summarized in Table 5.4.

Table 5.4: Sivers and Collins unweighted asymmetries, $A_{UT}^{\sin(\phi\pm\phi_S)}$, averaged over the experimental acceptance, which is $0.023 < x < 0.4$ and $0.2 < z < 0.7$. The uncertainty given for each value is statistical uncertainty. Average value of kinematics in the range are: $\langle P_{h\perp}\rangle$=0.4 GeV/c, $\langle Q^2\rangle$=2.4 GeV^2, $\langle x\rangle$=0.09, $\langle z\rangle$=0.36, $\langle x_F\rangle$=0.35.

	$A_{UT}^{\sin(\phi-\phi_S)}$ (Sivers)	$A_{UT}^{\sin(\phi+\phi_S)}$ (Collins)
π^+	0.033 ± 0.009	0.040 ± 0.014
π^-	0.01 ± 0.01	-0.063 ± 0.017
π^0	0.052 ± 0.026	-0.046 ± 0.041

As shown in Table 5.4, the Sivers and Collins asymmetry for π^+ is positive, and in particular the Sivers asymmetry is 3σ away from zero. Collins asymmetry for π^- is large negative. In contrast, the Sivers asymmetry for π^- is consistent with zero within the statistical uncertainties. For π^0 the Sivers asymmetry is positive at 2σ level, while the Collins asymmetry is negative only at 1σ level.

The positive asymmetry, $A_{UT}^{\sin(\phi\pm\phi_S)} > 0$, means more hadrons can be found at "left" side with respect to the nucleon spin direction viewed from the nucleon momentum direction. The negative symmetry is vice versa.

Recently, several experiments, STAR and PHENIX at BNL and COMPASS at CERN, are running to measure the transverse single-spin asymmetry. At this moment, published results of the asymmetries are available from STAR experiment [33] at BNL and E704 experiment [32] at Fermilab. The results of the single-spin asymmetry A_N measured by E704 (left plot) and STAR (right plot) experiments were already shown in Fig. 2.1. Those asymmetries were obtained in inclusive measurement of pion production in proton-proton collisions. At this moment, STAR result is available only for π^0. A_N is a left-right asymmetry with respect to spin direction of the nucleon.

Normally A_N is defined as,

$$A_N = \frac{1}{P}\frac{N^{\uparrow} - RN^{\downarrow}}{N^{\uparrow} + RN^{\downarrow}} \tag{5.47}$$

where R is defined as a ratio of luminosity for each spin state $R = L^{\uparrow}/L^{\downarrow}$, P indicates the beam polarization. This asymmetry also has value between -1 to 1. The E704 experiment used transversely polarized proton beam and unpolarized proton target. The STAR experiment used transversely polarized proton beam and unpolarized proton beam in colliding mode. Thus the results of A_N were measured in very different center of mass energies: $\sqrt{s} \simeq 20$ GeV in E704, $\sqrt{s} = 200$ GeV in STAR. Two observed A_N's for π^0 production are positive. Though they were measured at very different energy, A_N's show similar magnitude and behavior: A_N increases as x_F increases. In Fig. 2.1, the kinematical region of the transverse momentum of neutral pions is similar in two experiments: $0.5 \leq p_T \leq 2.0$ GeV/c in E704, $1.0 < p_T$ ($1.0 \leq \langle p_T \rangle \leq 2.4$ GeV/c, as labeled in the plot) in STAR. Here, p_T is transverse momentum of final state hadron, this corresponds to $P_{h\perp}$ of this thesis. The positive A_N means more hadrons are detected at "left" side with respect to the proton spin direction viewed from the transversely polarized proton momentum direction. The negative A_N is vice-versa. In this sense, the asymmetries $A_{UT}^{\sin(\phi \pm \phi_S)}$ from HERMES and A_N from STAR and E704 are consistent in sign for π^0. The sign of asymmetry for $\pi^{\pm}$ is also consistent between HERMES and E704.

Figure 5.28 shows single-spin asymmetry A_N measured by E704 experiment. The figure is similar to Fig. 2.1, but the asymmetry A_N is presented for two different p_T region; above (closed mark) and below (open mark) of the transverse momentum threshold $p_T = 0.7$ GeV/c. The asymmetry for π^+ for $p_T > 0.7$ GeV/c is positive and reaches to about 40% at highest x_F bin, and for $p_T \leq 0.7$ GeV/c it is small and goes up to $\sim 10\%$. The π^- asymmetry for $p_T > 0.7$ GeV/c is negative and similar magnitude to the π^+, and for $p_T \leq 0.7$ GeV/c it is small in particular in lower x_F region. In Fig. 5.28, a dotted line is also shown, which corresponds to $x_F = 0.35$. This value corresponds to the average value of x_F for averaged asymmetry $A_{UT}^{\sin(\phi \pm \phi)}$ shown in Table 5.4 is evaluated at HERMES. Moreover the average transverse momentum obtained for the $A_{UT}^{\sin(\phi \pm \phi)}$ is $\langle P_{h\perp} \rangle$ ($= \langle p_T \rangle$) $= 0.4$ GeV/c. Therefore A_N in the corresponding kinematical region is $A_N(x_F = 0.35, p_T \leq 0.7$ GeV/c). Comparing the asymmetries $A_{UT}^{\sin(\phi \pm \phi)}$ and A_N (open marks around $x_F = 0.35$), the magnitude of the asymmetries A_N are similar to $A_{UT}^{\sin(\phi \pm \phi)}$, the value of a few percent, even they have been measured in different energy and different channel of physics process.

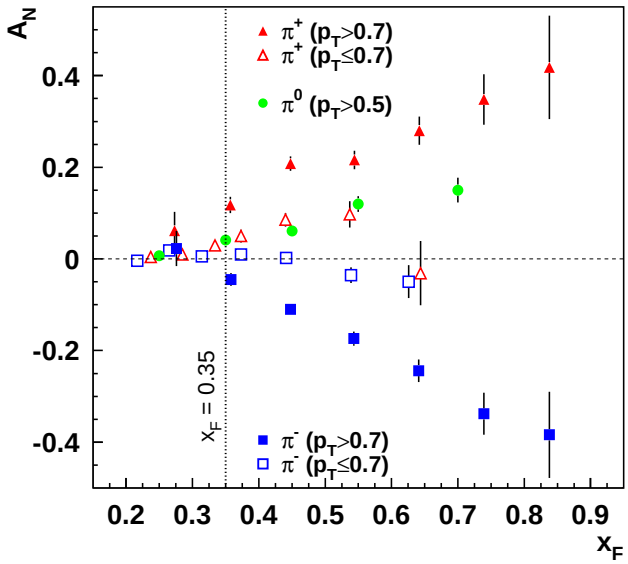

Figure 5.28: Single-spin asymmetry A_N for $\pi^{\pm}$ and π^0 measured by E704 experiment using transversely polarized proton beam and unpolarized proton target. A_N are displayed as a function of x_F for two different p_T region; above (closed mark) and below (open mark) of the transverse momentum threshold $p_T = 0.7$ GeV/c. For π^0, the transverse momentum region is $0.5 \leq p_T \leq 2.0$ GeV/c.

For exact comparison between $A_{UT}^{\sin(\phi \pm \phi)}$ and A_N, the Sivers and Collins effects have to be disentangled in A_N. However, those two effects in A_N cannot be separated at this moment[3]. Moreover A_N could involve not only Sivers and Collins effects but also other contributions. It is predicted that higher-twist contributions could be non-negligible in A_N, and these contributions can generate large single-spin asymmetry [79, 80]. Thus it is difficult to compare A_N with $A_{UT}^{\sin(\phi \pm \phi_S)}$ exactly. However it can be stated that both DIS and proton-proton collision give the same sign and similar magnitude of the asymmetries.

[3]In a recent theoretical study [78], it is proposed to measure azimuthal back-to-back correlation between hadrons in opposite hemisphere jets. This channel allows to access the Sivers effect in proton-proton collision.

Chapter 6

Smearing Correction of the Asymmetries

The measured asymmetries include some external contributions such as QED radiative effect and the effects coming from finite resolution of the detector. These effects cause a shift of several types of event kinematics: x, ϕ and ϕ_S and so on. We call them *smearing*. The azimuthal angles are determined with 3-momentum of the initial and final state lepton and the produced hadron. Those momenta are smeared by the detector instrumental and QED radiative effects.

In this chapter, these smearing effects will be discussed. Method to correct the measured asymmetries for the smearing effect are then described.

6.1 QED Radiative Effect

The measured cross section of deep inelastic scattering contains all higher order QED radiative contributions.

Figures shown in Fig. 6.1 are Feynman diagrams of the Born and the second order QED radiative processes in lepton-nucleon scattering. Figure 6.1(a) is the Born level process. Figure 6.1(b) and 6.1(c) are the initial and final state bremsstrahlung. Those processes change the kinematics of the lepton. Fig. 6.1(d) is the vertex loop correction at the lepton vertex. The vacuum polarization is shown in Fig. 6.1(e). The last two processes affect only the normalization of the cross section. Therefore those basically cancel out in the asymmetries. On the other hand, the bremsstrahlung processes directly affect the event kinematics, x, Q^2, ϕ and ϕ_S.

As presented in the previous chapter, the experimental DIS event kinematics are computed with incoming (beam) and outgoing leptons, which cor-

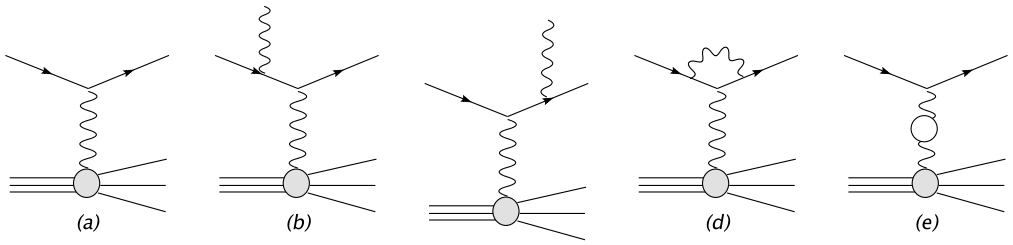

Figure 6.1: Born and second order QED radiative processes in lepton-nucleon scattering.

respond to the virtual photon 4-momentum $q^\mu = (\nu, \boldsymbol{q})$. The Born kinematics are modified with the radiative real photon 4-momentum $p_\gamma^\mu = (E_\gamma, \boldsymbol{p}_\gamma)$. Hence the Born kinematics can be expressed by the measured kinematics together with the radiative real photon energy E_γ and the angle between radiative photon and virtual photon $\theta_{\gamma^*\gamma}$,

$$\begin{aligned}
\nu_{Born} &= \nu - E_\gamma, \\
Q^2_{Born} &= Q^2 + 2E_\gamma(\nu - \sqrt{\nu^2 + Q^2}\cos\theta_{\gamma^*\gamma}), \\
x_{Born} &= \frac{Q^2_{Born}}{2M\nu_{Born}}, \\
W^2_{Born} &= W^2 - 2E_\gamma(\nu + M - \sqrt{\nu^2 + Q^2}\cos\theta_{\gamma^*\gamma}).
\end{aligned} \tag{6.1}$$

These kinematic variables do not need to be defined differently depending on whether the radiation occurred in the initial or final state, since the $Born$ (true) virtual photon four-momentum is independent of that condition, $q^\mu_{true} = (\nu - E_\gamma, \boldsymbol{q} - \boldsymbol{k}_\gamma)$.

However, other kinematics, ϕ and ϕ_S, which play important roles in this analysis, depend on a state where the radiation took place, because those angles are determined with the three-momentum of the initial (or final) state lepton.

6.1.1 Radiative Effect on ϕ and ϕ_S

The two azimuthal angles are defined in Eqs. (5.1) (5.2). The true virtual photon three-momentum, $\boldsymbol{q}_{true}$, can be written with the radiative photon

three-momentum $\boldsymbol{p}_\gamma$,

$$\boldsymbol{q}_{true} = \left\{ \begin{array}{ll} (\boldsymbol{k} - \boldsymbol{p}_\gamma) - \boldsymbol{k}' & : \text{initial state radiation} \\ \boldsymbol{k} - (\boldsymbol{k}' + \boldsymbol{p}_\gamma) & : \text{final state radiation} \end{array} \right\} = \boldsymbol{q} - \boldsymbol{p}_\gamma \tag{6.2}$$

thus the true virtual photon three-momentum is independent of initial or final state radiation. In this sense, the true hadron plane, $\overrightarrow{HP}$, is also independent of the initial or final state radiation.

$$\overrightarrow{HP} = \boldsymbol{q} \times \boldsymbol{P}_h, \tag{6.3}$$

$$\overrightarrow{HP}_{true} = \boldsymbol{q}_{true} \times \boldsymbol{P}_h. \tag{6.4}$$

In addition, the expression of the true target polarization plane which is determined by $\boldsymbol{S}$ and $\boldsymbol{q}_{true}$ (see Fig. 5.1 and Eq. (5.1)), $\overrightarrow{SP}$, can also be obtained by replacing $\boldsymbol{P}_h$ to $\boldsymbol{S}$ in Eq. (6.4).

On the other hand, the true lepton scattering plane, $\overrightarrow{LP}_{true}$, can be written as,

$$\overrightarrow{LP} = \boldsymbol{q} \times \boldsymbol{k} = \boldsymbol{k} \times \boldsymbol{k}', \tag{6.5}$$

$$\overrightarrow{LP}_{true} = \left\{ \begin{array}{ll} \overrightarrow{LP} - (\boldsymbol{p}_\gamma \times \boldsymbol{k}') & : \text{initial state radiation,} \\ \overrightarrow{LP} + (\boldsymbol{k} \times \boldsymbol{p}_\gamma) & : \text{final state radiation.} \end{array} \right. \tag{6.6}$$

Hence $\overrightarrow{LP}$ is different for the initial or final state radiation. The resulting true azimuthal angles are,

$$\phi_{S,true} = \frac{\overrightarrow{LP}_{true} \cdot \boldsymbol{S}}{|\overrightarrow{LP}_{true} \cdot \boldsymbol{S}|} \cos^{-1}\left(\frac{\overrightarrow{LP}_{true}}{|\overrightarrow{LP}_{true}|} \cdot \frac{\overrightarrow{SP}_{true}}{|\overrightarrow{SP}_{true}|} \right) \tag{6.7}$$

$$\phi_{true} = \frac{\overrightarrow{LP}_{true} \cdot \boldsymbol{P}_h}{|\overrightarrow{LP}_{true} \cdot \boldsymbol{P}_h|} \cos^{-1}\left(\frac{\overrightarrow{LP}_{true}}{|\overrightarrow{LP}_{true}|} \cdot \frac{\overrightarrow{HP}_{true}}{|\overrightarrow{HP}_{true}|} \right) \tag{6.8}$$

6.2 Detector Smearing Effect

Other source of kinematic smearing is interactions of the final state particles with detector materials. In particular light leptons, electrons and positrons, lose a part of their energy due to multiple scattering, even in small amounts of materials.

As mentioned above, radiative effect leads to larger energy transfer ν with respect to ν_{Born}. The detector smearing effects however results in a larger measured energy/momentum of the scattered lepton than real energy in some cases. Observed ν is smaller than real in such cases.

The detector effect was studied using the entire detector Monte Carlo simulation program based on the GEANT package [81].

6.3 The HERMES Monte Carlo Simulation

In order to correct for the QED radiative and detector effects, two types of dataset are needed: "tracked dataset" and "Born dataset" which can be obtained from a Monte Carlo (MC) simulation.

In this analysis the HERMES Monte Carlo simulation program is employed. The MC program consists of three parts, `GMC`, `RADGEN` and `HMC`. `GMC` generates DIS events. The generation of the higher order QED process is done with `RADGEN`. `HMC` is the detector simulation which describes several interactions of the particles with materials of spectrometers.

6.3.1 Monte Carlo Datasets

Tracked dataset

A DIS event is simulated with `LEPTO` [82]. The event is passed to `RADGEN` [83] which generates radiative photons according to bremsstrahlung cross section, and `RADGEN` provides the Born kinematics ν_{Born}, Q^2_{Born}, x_{Born} and W^2_{Born} according to Eq. (6.1). These Born kinematics are passed to `JETSET` [75] which generates hadrons in the final state. Above processes are implemented in `GMC` and `RADGEN`.

The generated particles are passed to `HMC` which is based on the `GEANT` package [81]. The program simulates several interactions between a given particle and materials in the HERMES instruments. At the end, `HRC` performs the particle track reconstruction using the same method as used in the experimental data.

By comparing these Born kinematics and tracked (reconstructed) kinematics which are kept in the resulting tracked dataset, one can obtain the QED radiative and detector smearing effects. However `RADGEN` does not provide information on where the radiation took place. Initial or final state radiations are not identified. So the *true* lepton scattering plane as given in Eq. (6.6) cannot be determined. With absence of the true lepton scattering plane, it is only possible to evaluate the detector smearing effect for azimuthal angles ϕ and ϕ_S. Radiative effects on ϕ and ϕ_S cannot be studied. But some possible tests for the radiative effect on the azimuthal angles will be discussed later.

Comparison of kinematic distributions of π^+ normalized to the total number of DIS events is shown in Fig. 6.2. The tracked dataset, which includes smearing effect, basically reproduces the data for the entire distributions. In the case of ϕ distributions, the agreement is not as good.

Also Born kinematic distributions are shown in Fig. 6.2. In Born kine-

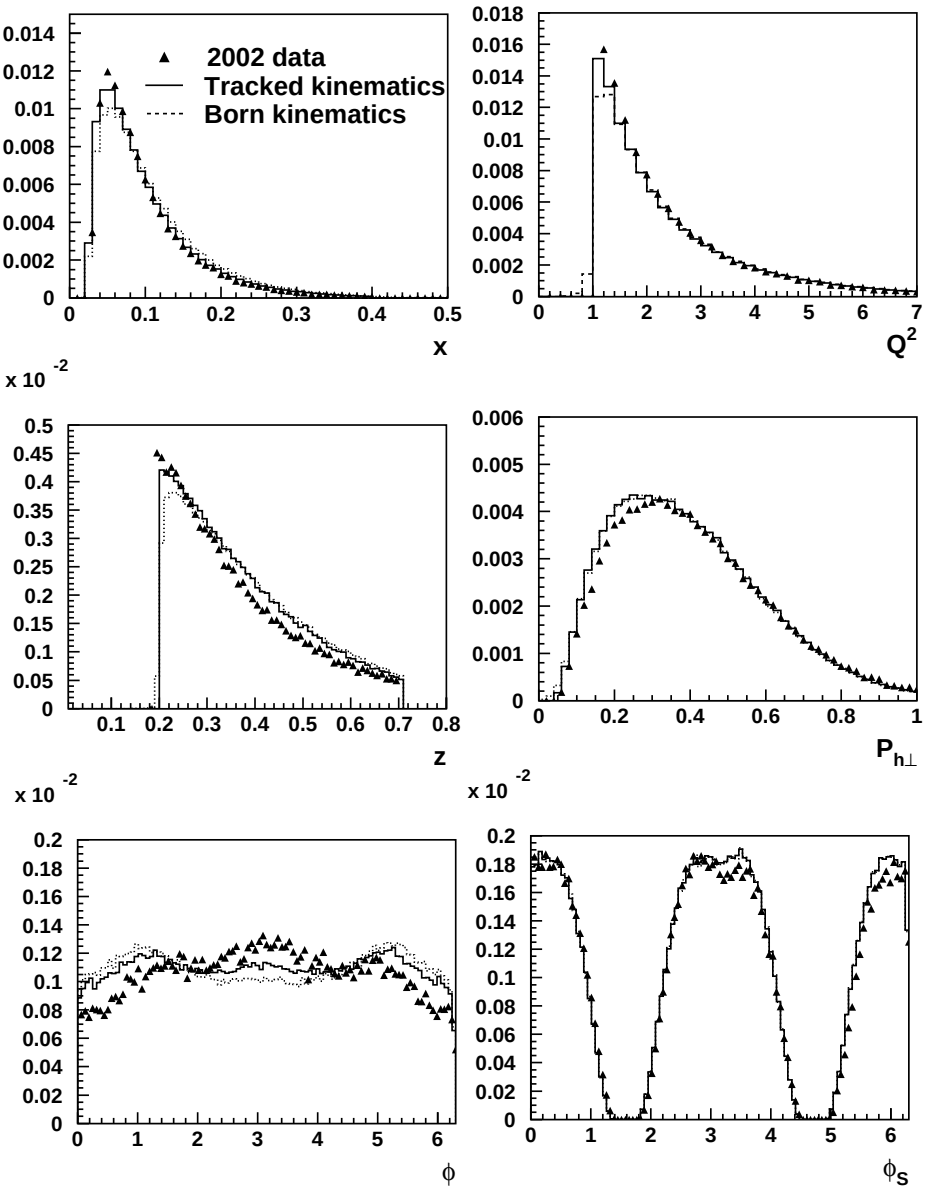

Figure 6.2: Comparison of kinematic distributions of π^+ normalized to the total number of DIS events. The distributions were obtained from the experimental data and tracked dataset. In this figure, the experimental data (triangle), the tracked dataset (solid histogram) and the Born kinematic distributions (dashed histogram) are displayed.

matics of ϕ and ϕ_S, the QED radiative effect is not taken into account. The x distribution of the tracked kinematics is shifted to smaller values compared to the distribution of the Born kinematics. The z and Q^2 distributions of the Born kinematics has a tail to lower values.

Born dataset

For Born level DIS data, simulations only with the lowest order QED processes without radiative effects and without detector effects are carried out. So a DIS event generated with `LEPTO` is passed directly to `JETSET`. The *box acceptance* cuts are applied to the produced particles, which takes into account for the geometrical acceptance of the HERMES spectrometer. Therefore, this dataset does not include radiative and instrumental effects.

This dataset is needed in the smearing correction procedure, because the QED radiative effects do not conserve the total cross section as mentioned in Section 6.2. The details for use of this dataset will be discussed in Section 6.4.

6.3.2 Test of Smearing Effect

Radiative effect

In general, the calculation of the radiative effect requires the information of the nucleon structure, structure function for DIS and form factor for elastic processes.

As described in references [84, 83, 85], the radiative effect can have spin dependence because the structure functions have spin dependence. For example in the studies of quark helicity distribution Δq, the polarized structure function g_1 is used in the evaluation of radiative corrections [83]. The g_1 has been measured from inclusive measurement of the DIS.

However, the structure functions of the transversely polarized nucleon are not available, since the inclusive measurement with a transversely polarized target does not provide useful information on the structure of the transversely polarized nucleon. With absence of transverse structure function, there is no radiative event generator available for a transversely polarized target. The spin dependent radiative effect can systematically influence the lepton scattering and hadron production planes as shown in Eqs. (6.6) and (6.4).

Figure 6.3 shows radiative photon energy distribution obtained from tracked dataset. Low energy radiative photons are dominant, so it is expected that the radiative photons are most likely collinearly emitted from the lepton.

As far as using `RADGEN`, one cannot identify whether the radiative photon is emitted in initial or final state. But there is an evaluation of bremsstrahlung

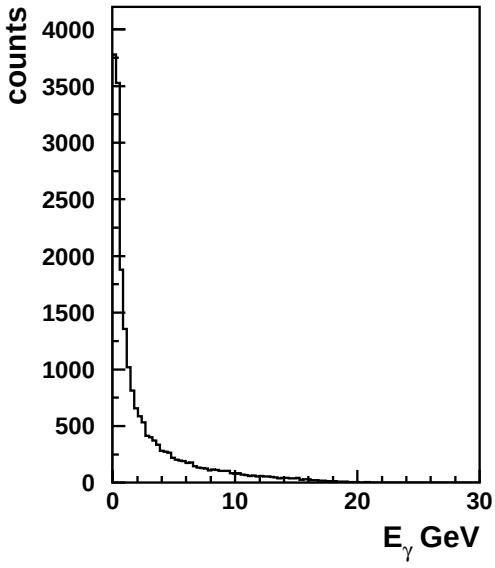

Figure 6.3: Energy distribution of unpolarized radiative photons in semi-inclusive DIS.

processes. Figure 6.4 shows differential cross section of bremsstrahlung as a function of $\theta_{\gamma^*\gamma}$ in HERMES kinematics region. In the figure, a specific case where the radiative photon is in the same plane as the incoming and outgoing lepton is displayed [17]. As shown in Fig. 6.4, the bremsstrahlung cross section has a three peak structure corresponding to the emitted radiative photon being collinear to the virtual photon or incoming or outgoing lepton.

A test for radiative effect on the determination of lepton scattering plane was performed. Fig. 6.5 shows the angle distribution between two *true* lepton scattering planes calculated according to Eq. (6.6) assuming the initial and final state radiation in one event. As shown in the figure, the angle between two lepton scattering planes are very small, around 0.007 rad. The result of Fig. 6.5 indicates that the radiative photons is emitted collinearly to the parent lepton and the radiative photon is almost in the same plane which is determined by the incoming or outgoing lepton. The radiative effect, at least unpolarized case, changes the lepton scattering plane less than 0.05 rad.

In addition to the evaluation of lepton scattering plane, the smearing of ϕ_S was also evaluated in a similar way to Fig. 6.5. The results are presented in Fig. 6.6. As shown in Fig. 6.6, the possible effect on the azimuthal angle ϕ_S is also less than 0.05 rad.

As a conclusion, the radiative effect in the unpolarized case is much smaller than the bin size of ϕ and ϕ_S. Moreover, looking at tracked dataset,

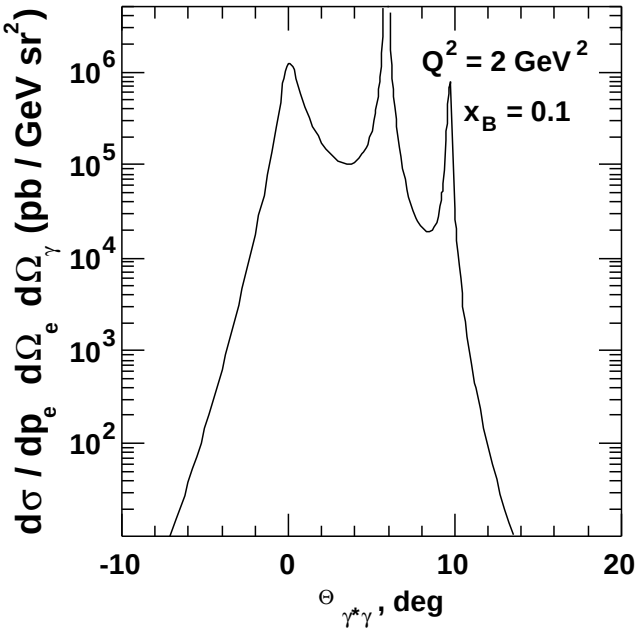

Figure 6.4: Differential cross section of bremsstrahlung process as function of $\theta_{\gamma^*\gamma}$ which is defined as the angle between the virtual photon and the radiative real photon. Taken from [17].

the radiative events are roughly ∼30% in the simi-inclusive data sample. However the implications of the spin dependent radiative effect are still not known.

Instrumental Effect

In contrast to the radiative effect, the detector instrumental effect, such as multiple scattering, can influence all tracks of the data sample. Fig. 6.7 shows the instrumental effect on ϕ_S. Comparing Fig. 6.7 with Fig. 6.6, the detector smearing effect is found to be larger than radiative effects.

In this analysis, only the detector instrumental effect is taken into account for the evaluation of Born ϕ and ϕ_S value.

6.4 Unfolding Procedure

The measured kinematic variables are smeared by the QED radiative effect and the detector instrumental effect as mentioned in the previous sections.

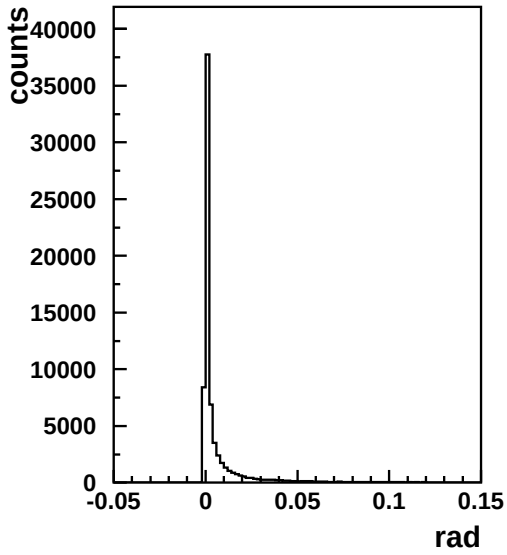

Figure 6.5: Distribution of the angle between lepton scattering planes which are evaluated by assuming the initial and final state radiation in each event. This results obtained by requiring the DIS criteria and at least one hadron in acceptance.

As a common method of the smearing correction for an observed asymmetry, a correction factor which works as a dilution factor of the asymmetry is introduced. For example, the correction factor δ_{RC} for the radiative correction is given by,

$$\delta_{RC}^{u,p} \equiv \frac{\sigma_X^{u,p}}{\sigma_B^{u,p}}, \tag{6.9}$$

where σ_X and σ_B are observed and Bron cross sections, and the superscripts u and p indicate unpolarized and polarized cases, respectively. This gives a simple relation between Born A^B asymmetry and experimentally observed asymmetry A^X,

$$\frac{A^X - A^B}{A^B} = \frac{\delta_{RC}^p - \delta_{RC}^u}{\delta_{RC}^u}. \tag{6.10}$$

The same relation can be applied for the detector smearing correction using reliable Monte Carlo simulations and the Born cross section calculation. However as already mentioned in the previous section, the Born cross section for the transversely polarized nucleon is unknown. So we cannot apply this method to this analysis.

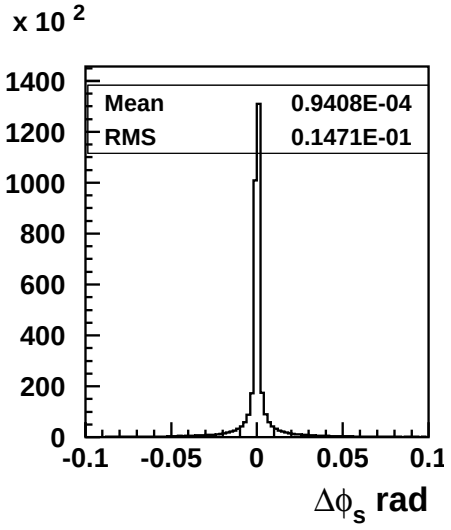

Figure 6.6: This figure shows the deference of two radiative corrected ϕ_S's which are evaluated assuming the initial ($\phi_{S,ini}$) and final ($\phi_{S,fin}$) state radiation. $\Delta\phi_S$ is defined as $\Delta\phi_S \equiv \phi_{S,ini} - \phi_{S,fin}$. Note that this results do not include detector instrumental effects.

In this section, an alternative method to correct for the smearing effects will be discussed. The correction method is based on an unfolding algorithm [86]. The method has been originally developed in the analyses of quark helicity distribution Δq [10, 9]. It is also assumed that the Born cross section σ_B is already known. But the underlying basic idea of this method is the *event migration*. The idea of the event migration is illustrated in Fig. 6.8. The observed kinematics are smeared by the radiative and detector smearing effects. As a result, the event migrates from the Born kinematics (x, ϕ, ϕ_S) to the smeared kinematics (x', ϕ', ϕ'_S). This algorithm uses the relation between Born and measured kinematics for the extraction of the Born asymmetry.

In the following discussion, we use two symbols to distinguish measured asymmetry, A^X, and the smearing corrected asymmetry (Born asymmetry [1]), A^B. Here we consider the asymmetry as a function of x, ϕ and ϕ_S; $A^{X,B}(x, \phi, \phi_S)$, where the other kinematics, such as z, Q^2, are integrated over the measured range.

The measured asymmetry can be written with measured hadron yields

[1]Note that A^B is not perfect Born level asymmetry because the spin dependent smearing effects are not taken into account, but expediently A^B is called as Born asymmetry.

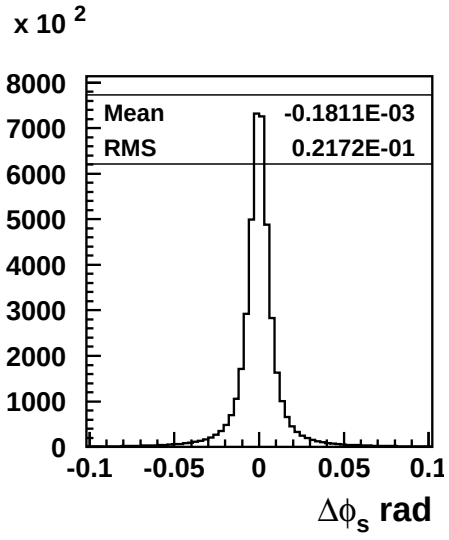

Figure 6.7: Difference between two ϕ_S's which evaluated with and without the detector smearing effects. Note this result is independent of the QED radiative effect.

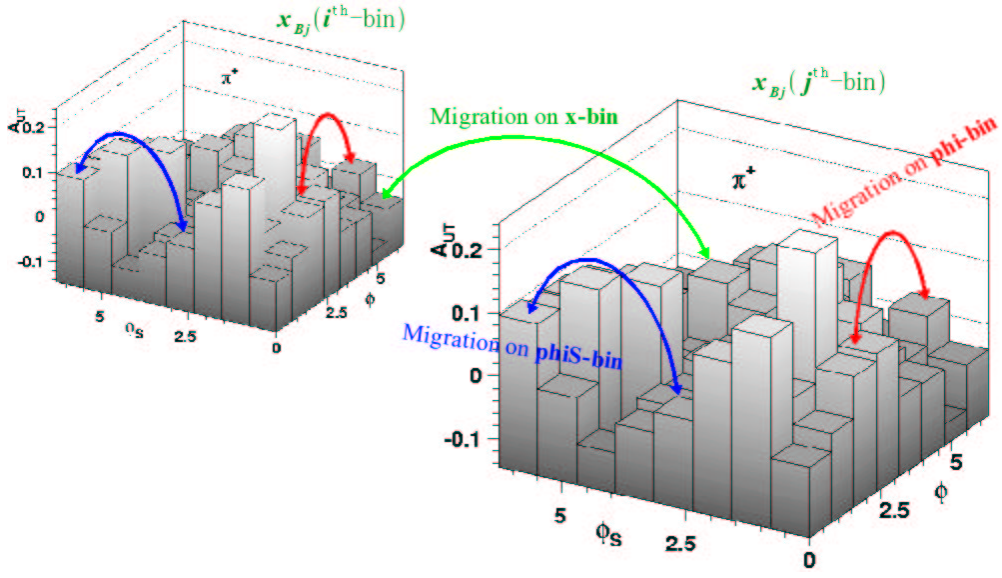

Figure 6.8: Schematic illustration of event migration.

(normalized with luminosity), $X^{\uparrow\downarrow}(x, \phi, \phi_S)$, for each kinematic bin,

$$A^X(x_{k'}, \phi_{l'}, \phi_{Sm'}) = \frac{X^{\uparrow}(x_{k'}, \phi_{l'}, \phi_{Sm'}) - X^{\downarrow}(x_{k'}, \phi_{l'}, \phi_{Sm'})}{X^{\uparrow}(x_{k'}, \phi_{l'}, \phi_{Sm'}) + X^{\downarrow}(x_{k'}, \phi_{l'}, \phi_{Sm'})} \quad (6.11)$$

$$\equiv \frac{X_p(x_{k'}, \phi_{l'}, \phi_{Sm'})}{X_u(x_{k'}, \phi_{l'}, \phi_{Sm'})}, \quad (6.12)$$

where subscripts u and p indicate *unpolarized* and *polarized* respectively, and subscripts of kinematic variables, k', l' and m' denote the measured kinematic bin numbers.

The goal of this unfolding procedure is to obtain the Born asymmetries, $A^B(x_k, \phi_l, \phi_{Sm})$, where k, l, m indicate the corresponding bin number for the Born kinematics. For simplicity, we introduce new symbols i and j representing the measured kinematics and the Born kinematics.

So now we can rewrite the asymmetry with one index i

$$A^X(x_{k'}, \phi_{l'}, \phi_{Sm'}) = A^X(i) = \frac{X^{\uparrow}(i) - X^{\downarrow}(i)}{X^{\uparrow}(i) + X^{\downarrow}(i)} \equiv \frac{X_p(i)}{X_u(i)}. \quad (6.13)$$

Using the Born yield defined as $B^{\uparrow\downarrow}(j) \equiv B^{\uparrow\downarrow}(x_k, \phi_l, \phi_{Sm})$, the asymmetry can be expressed as follows,

$$A^B(x_k, \phi_l, \phi_{Sm}) = A^B(j) \quad (6.14)$$

$$= \frac{B^{\uparrow}(j) - B^{\downarrow}(j)}{B^{\uparrow}(j) + B^{\downarrow}(j)} \quad (6.15)$$

$$\equiv \frac{B_p(j)}{B_u(j)}. \quad (6.16)$$

In this expression, the smearing effect appears as an event migration from the Born kinematic bin j to another measured bin i. The migration of j-bin to i-bin is described with a *Smearing Matrix*, $S^{\uparrow\downarrow}(i, j)$. The smearing matrix is defined as,

$$S^{\uparrow\downarrow}(i, j) \equiv \frac{\partial \sigma_X^{\uparrow\downarrow}(i)}{\partial \sigma_B^{\uparrow\downarrow}(j)}, \quad (6.17)$$

where $\sigma_X^{\uparrow\downarrow}$ and $\sigma_B^{\uparrow\downarrow}$ are the measured and Born cross sections, respectively. Here we rewrite the definition, replacing the cross sections by hadron yields,

$$S^{\uparrow\downarrow}(i, j) \equiv \frac{\partial X^{\uparrow\downarrow}(i)}{\partial B^{\uparrow\downarrow}(j)}, \quad (6.18)$$

From Eq. (6.18), we can express a relation between the measured and Born hadron yields as,

$$X^{\uparrow\downarrow}(i) = \sum_{j=0}^{N_B} S^{\uparrow\downarrow}(i,j)\ B^{\uparrow\downarrow}(j), \quad i = 1, ..., N_X, \tag{6.19}$$

where the Born yield in bin j is independent of other Born bins. In the above relation, N_B and N_X indicate the number of the Born and measured kinematic bins.

It should be noted that the sum for j starts at 0th bin; events generated outside of the acceptance but smeared into the acceptance are stored in 0th bin. Therefore the matrix consists of $N_X \times (N_B + 1)$ elements.

If we know the smearing matrix, the Born asymmetry can be obtained from $B^{\uparrow\downarrow}(j)$. In principle, the smearing matrix should have spin dependence as in Eq. (6.17). We assume the matrix can be decomposed to two parts,

$$X^{\uparrow\downarrow}(i) = \sum_{j=0}^{N_B} S(i,j)\Delta^{\uparrow\downarrow}(i,j)\ B^{\uparrow\downarrow}(j). \tag{6.20}$$

where $S(i,j)$ and $\Delta^{\uparrow\downarrow}(i,j)$ are the spin-independent and spin-dependent smearing matrices, respectively. Using the decomposed smearing matrix, the polarized and unpolarized part yield,

$$X^{p}(i) = \sum_{j=0}^{N_B} S(i,j)\left\{\Delta^{\uparrow}(i,j)\ B^{\uparrow}(j) - \Delta^{\downarrow}(i,j)\ B^{\downarrow}(j)\right\}, \tag{6.21}$$

$$X^{u}(i) = \sum_{j=0}^{N_B} S(i,j)\left\{\Delta^{\uparrow}(i,j)\ B^{\uparrow}(j) + \Delta^{\downarrow}(i,j)\ B^{\downarrow}(j)\right\} \tag{6.22}$$

However at this moment, we do not have reliable information about transverse spin structure of the nucleon. Under the assumption that spin dependence of the smearing matrix is small, Δ's are close to 1.

$$\Delta^{\uparrow(\downarrow)}(i,j) \simeq 1.$$

Finally we obtain,

$$\begin{aligned} X^{p,u}(i) &= \sum_{j=0}^{N_B} S(i,j)\left\{B^{\uparrow}(j) \mp B^{\downarrow}(j)\right\} \\ &= \sum_{j=0}^{N_B} S(i,j)B^{p,u}(j). \end{aligned} \tag{6.23}$$

To obtain the spin independent smearing matrix, two types of unpolarized Monte Carlo datasets are employed as already described in Section 6.3.1. One is the Born dataset, this gives a Born event distribution $n_B^u(j)$. Another is the tracked dataset which includes detector simulation and reconstruction algorithm used in experiment. The tracked dataset gives tracked event distribution $n_X^u(i)$, where the difference from $X^u(j)$ is a normalization with luminosity in experiment and Monte Carlo. Thus X^u and n_X^u are related with a normalization constant k_i,

$$X^u(i) = k_i \; n_X^u(i) \tag{6.24}$$

By comparing Born and tracked kinematics in the tracked dataset, each event which migrates from j to i bin can be identified. Using this dataset we can obtain an event rate of migration j to i; $n^u(i,j)$ which forms a matrix. This migration event rate is related with tracked event distribution $n_X^u(i)$,

$$n_X^u(i) = \sum_{j=0}^{N_B} n^u(i,j). \tag{6.25}$$

The matrix $n(i,j)$ also consists of $N_X \times (N_B + 1)$ elements.

From Eqs. (6.23) - (6.25),

$$\begin{aligned} X^u(i) &= k_i \sum_{j=0}^{N_B} n^u(i,j), = \sum_{j=0}^{N_B} S(i,j) n_B^u(j) \\ \sum_{j=0}^{N_B} &\Big[k_i \; n^u(i,j) - S(i,j) \; n_B^u(j) \Big] = 0, \end{aligned}$$

where $B^u(j) = n_B(j)$ was used. Finally we obtained the smearing matrix

$$S(i,j) = k_i \frac{n^u(i,j)}{n_B^u(j)}. \tag{6.26}$$

where k_i is given in Eq. (6.24) and it works as a normalization factor. Thus the k_i only depends on measured bin i. It can be expressed in the form of an $N_X \times N_X$ diagonal matrix $k(i,i)$.

It should be noted that the Born event distribution $n_B^u(j)$ is obtained from the Born dataset. As already mentioned in Section 6.3.1, the QED radiative effects do not conserve the total cross section. Therefore the matrix $n^u(i,j)$ which is obtained from tracked dataset has to be normalized by $n_B^u(j)$ as appeared in the smearing matrix (Eq. (6.26)).

We have now smearing matrix $S(i,j)$. From Eq. (6.23), Born yield $B(j)$ can be evaluated from measured yield $X(i)$. Using the smearing matrix and Eq. (6.23), we can obtain the Born yield by minimizing χ^2 defined as,

$$\chi^2 = \left(X^p - SB^p\right)^T C_X^{-1} \left(X^p - SB^p\right), \tag{6.27}$$

where C_X is the covariance matrix of the observed polarized hadron yield. For the covariance matrix, the statistical correlation between observed bins are neglected. Actually most of all off-diagonal elements are zero, because the event rate which contains two hadron tracks is very small. Therefore the actual covariance matrix does not have any off-diagonal elements,

$$(C_X)_{ii} = \left[\delta X^p(i)\right]^2, \tag{6.28}$$

$$(C_X)_{ij} = 0 \quad (i \neq j), \tag{6.29}$$

where $\delta X^p(i)$ indicates the statistical uncertainties of observed polarized hadron yield. Thus the statistical uncertainties on the Born yield B^p is given by square-root of the diagonal elements of covariance matrix defined as,

$$C_B = \left[\left(S^T C_X^{-1} S\right)^{-1} S^T C_X^{-1}\right] C_X \left[\left(S^T C_X^{-1} S\right)^{-1} S^T C_X^{-1}\right]^T. \tag{6.30}$$

This correction procedure is performed both for the polarized and unpolarized observed yields, because there are small discrepancies between data and tracked dataset. The evaluated Born asymmetries using ratio of polarized to unpolarized Born yields may minimize the systematic effect due to Monte Carlo simulation.

The smearing correction for asymmetries of neutral pion is not demonstrated since it is difficult to obtain the two-dimensional asymmetry with background correction.

6.5 Results

6.5.1 Smearing Matrices

In this analysis, number of bins $N_X = 320$ $(= 5 \times 8 \times 8)$ is used; 5 x-bins, 8 ϕ- and ϕ_S-bins, and $N_B = 321$ including Born 0th bin. Thus the smearing matrices have 320×321 elements.

The tracked and the Born dataset were used to determine the matrices $n^u(i,j)$ and $n^u_X(i)$ and $n^u_B(j)$. For evaluation of $n^u(i,j)$ and $n^u_B(j)$, the Born kinematics of x is determined including the QED radiative effect according

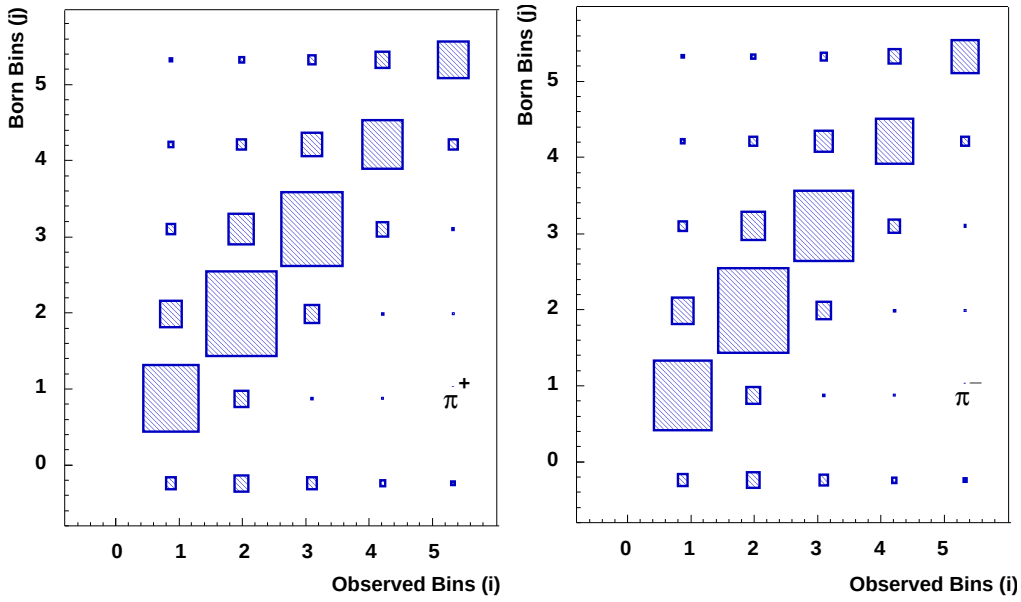

Figure 6.9: Matrix $n^u(i,j)$ for x-smearing of π^+ (left panel) and π^- (right panel). Note that these results integrated over the ϕ and ϕ_S.

to Eq. (6.1). The smearing matrix was divided into the x-smearing and (ϕ, ϕ_S)-smearing parts for convenience.

Figure 6.9 presents the matrix for the x-smearing of the charged pion tracks, which are integrated over the ϕ and ϕ_S bins. The bin-number of x presented in the figure follows Table 5.3. As shown in the figure, diagonal elements dominate. A small amount of background migrates into acceptance due to the detector instrumental and QED radiative effects. They are found in the $j = 0$ row. It is found that roughly 20% of the total number of reconstructed tracks (including leptons) are assigned to the $j = 0$ row. The smearing effect tends to make the reconstructed x larger than the Born kinematics. Comparing results for π^+ and π^-, no charge dependence is found.

Figure 6.10 shows the matrices $n^u(i,j)$ for the azimuthal angles, ϕ and ϕ_S. In the figure the matrices integrated over x-bins are shown. The matrices have 64×65 elements with combination of ϕ and ϕ_S bins. The rule of the

bin assignment is as follows,

$$\begin{aligned}
&(\phi_1, \phi_{S,m=1,..,8}) && \text{for } \; i = 1, .., 8, \\
&(\phi_2, \phi_{S,m=1,..,8}) && \text{for } \; i = 9, .., 10, \\
&\qquad\qquad \vdots \\
&(\phi_8, \phi_{S,m=1,..,8}) && \text{for } \; i = 57, .., 64.
\end{aligned}$$

The bin assignment of ϕ and ϕ_S bins are schematically illustrated in Fig. 6.11. For example if we look at the combination of $(\phi_1, \phi_{S,m})$, this corresponds to a small matrix of Fig. 6.10. This small matrix is a $n(i,j)$ matrix for ϕ_S as shown in Fig. 6.12. The matrix of ϕ_S shows a cosine structure in the diagonal elements. This is because of the acceptance effect as seen in Fig. 5.2. The tridiagonal matrix structure of the matrix in Fig. 6.10 is due to migration among ϕ-bins. The smearing effect on ϕ_S is smaller than ϕ. One of the reasons of the large smearing effect on ϕ is the momentum resolution of hadrons which is worse than leptons.

6.5.2 Corrected Asymmetries

The unweighted asymmetries corrected for the smearing effects were obtained from the measured asymmetries presented in Chapter 6 and the smearing matrix described above. The corrected asymmetries were obtained with reduced χ^2 of 1.3 and 1.7 for π^+ and π^- asymmetries, respectively. The results are shown in Fig. 6.13 and 6.14. In the figures, the un-corrected asymmetries are also shown.

The statistical uncertainties of the corrected asymmetries were enlarged by the smearing correction, since events which enter into the acceptance from outside are taken into account. For example, the measured yield N contains the real signal N_s and the background N_b which comes from outside of the acceptance, so $N = N_s + N_b$. The statistical uncertainty δN_s of the signal becomes larger than that of N; $\delta N_s = \sqrt{\delta N^2 + \delta N_b^2}$.

The resulting asymmetry of π^+ stayed non-zero values after the smearing correction applied. The magnitude of the correction were small compared with the statistical errors. For π^-, in particular Collins asymmetry, there are small fluctuations at high x region. The Sivers asymmetry involves $\sin(\phi - \phi_S)$, and the Sivers angle $(\phi - \phi_S)$ is independent of lepton scattering plane. On the other hand, the Collins angle $(\phi + \phi_S)$ depends on the lepton scattering plane. Thus the smearing effect on the Collins asymmetry can be larger than the Sivers asymmetry.

This migration method moves around the events according to the smearing matrices. In principle, the weighted asymmetries can also be corrected

with the same method as used for unweighted asymmetries. Then the smearing correction has been carried out also for weighted asymmetries. The smearing corrections on the weighted asymmetries[2] resulted in the relatively large reduced chi-square more than 4 for both π^+ and π^-. Since the weighted asymmetry contains the $(P_{h\perp}/z)$ factor in the numerator, it can be expected that the smearing correction for the weighted asymmetries is more sensitive to the reproducibility of the Monte Carlo simulation than for the unweighted asymmetries. In the event distribution of $P_{h\perp}$ and z, there are small discrepancies between experimental data and tracked Monte Carlo data as shown in Fig. 6.2. Figure 6.15 shows comparison between the event distributions for the Born and reconstructed kinematics of z and $P_{h\perp}$. As shown in Fig. 6.15 the event distribution of reconstructed and Born $P_{h\perp}$ are almost consistent. The comparison of the z distributions shows small tail due to QED radiative effect. This tail can make the Born asymmetry slightly smaller than measured. At the end, it is expected that the smearing effect for the weighted asymmetry is the similar magnitudes for the unweighted asymmetry, making the Born asymmetry smaller.

[2]For the correction of the weighted asymmetry, $(P_{h\perp}/z)$-weighted smearing matrix was used. The $(P_{h\perp}/z)$-weighted smearing matrix can be obtained by filling the $n(i,j)$ and $n_B(j)$ matrix with weight of $P_{h\perp}$.

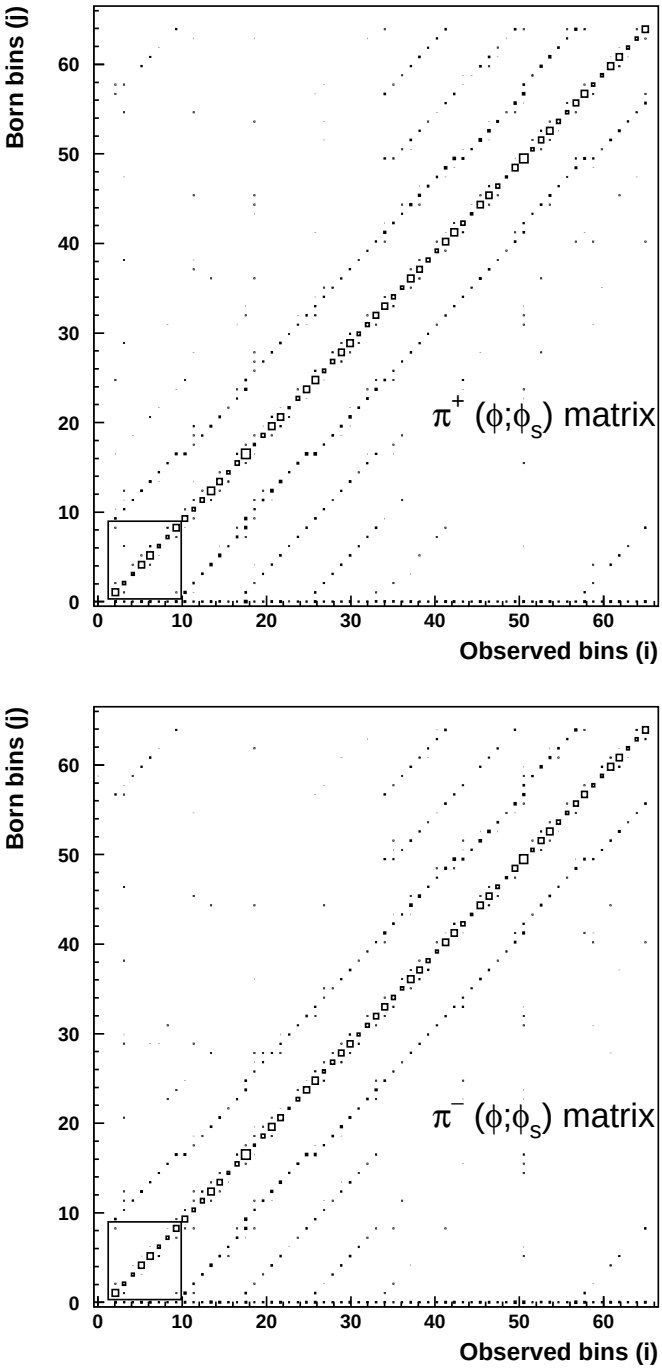

Figure 6.10: Matrix $n^u(i,j)$ for π^+ (top panel) and π^- (lower panel). The horizontal axis is the observed bins and vertical axis is Born bins. Note that these results are integrated over all x bins.

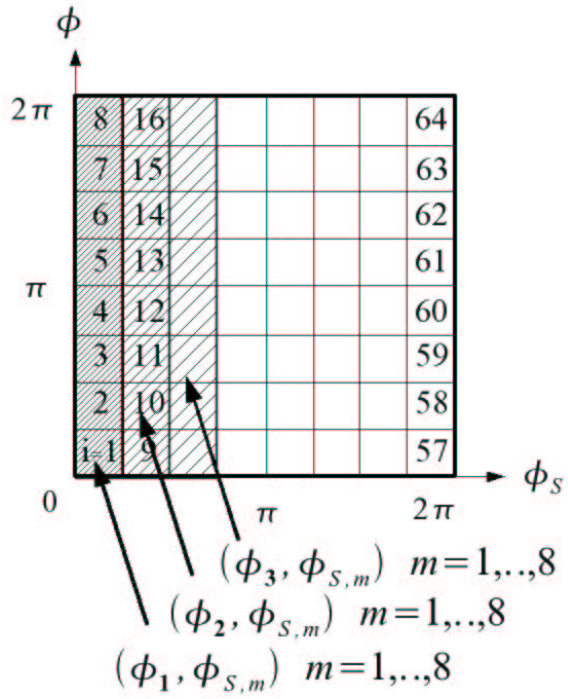

Figure 6.11: Schematic illustration of ϕ and ϕ_S combination.

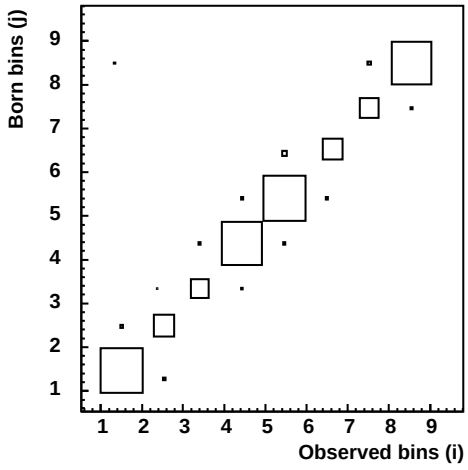

Figure 6.12: Matrix $n(i,j)$ on ϕ_S. This shows a small matrix of Fig. 6.10.

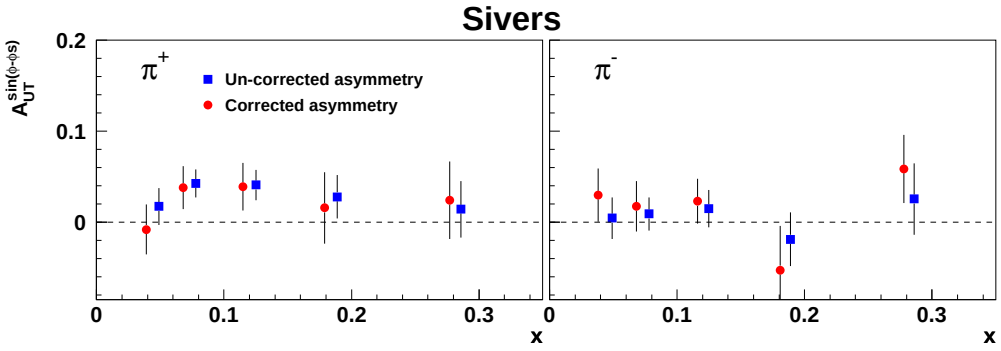

Figure 6.13: Comparison between measured asymmetries (square) and corrected asymmetries (circle) for Sivers type. This results were obtained using unweighted asymmetries.

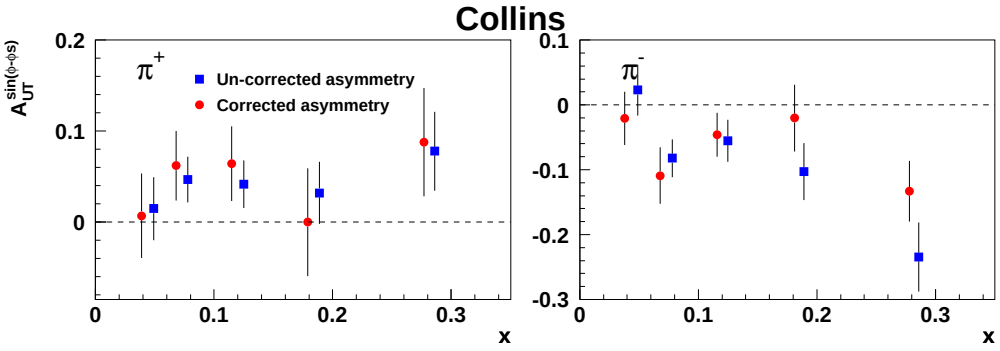

Figure 6.14: Comparison between measured asymmetries (square) and unfolded asymmetries (circle) for Collins type. This results were obtained using unweighted asymmetries.

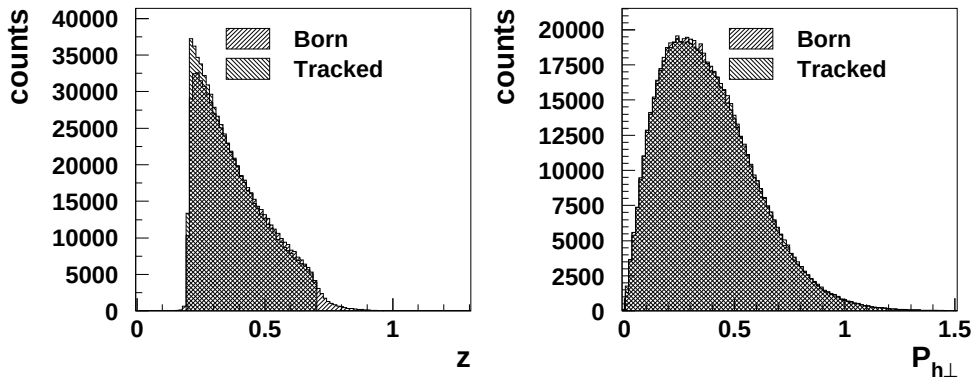

Figure 6.15: Comparison between generated and reconstructed event distributions for z (left) and $P_{h\perp}$ (right).

Chapter 7

Extraction of Sivers Function

The observed Sivers type asymmetry in π^+ production suggests significant non-zero values even after correction for the smearing effect as demonstrated in the previous chapter. Based on this result, interpretations of the Sivers type asymmetries are investigated in this chapter in the framework of quark parton model.

First we discuss the possibility to apply the quark parton model interpretation to the observed asymmetries. Then the Sivers function for different quark types is actually extracted. Finally discussion of the obtained results is given together with some theoretical investigations.

Note that $f_{1T}^{\perp(1)}$ and $f_{1T}^{\perp(1/2)}$ defined in Section 3.1.2 is, in a precise sense, a *moment* of p_T. Nevertheless in the following we call this moment of p_T as Sivers function. In addition, to simplify the expression, new symbols are introduced: $\bar{A}_{\mathcal{S}}$ for weighted asymmetries and $A_{\mathcal{S}}$ for unweighted asymmetries.

7.1 Deconvolution on Transverse Momenta

Recalling Eqs. (3.2)-(3.4), the Sivers type cross section is expressed with parton distribution and fragmentation functions (PDF's and FF's),

$$\begin{aligned} d^4\sigma_S(x,z,P_{h\perp}) \;\propto\; & \\ & \sum_q e_q^2 \int d\boldsymbol{p}_T\, d\boldsymbol{k}_T \left(\frac{\boldsymbol{p}_T\cdot\hat{\boldsymbol{P}}_{h\perp}}{M}\right) f_{1T}^{\perp q}(x,p_T^2)\; D_1^{q\to h}(z,z^2k_T^2) \\ & \times\delta\left(\boldsymbol{p}_T - \frac{\boldsymbol{P}_{h\perp}}{z} - \boldsymbol{k}_T\right). \end{aligned} \tag{7.1}$$

At the moment, we do not have any information on transverse momenta p_T and k_T, and we do not know the behavior of PDF's and FF's as a function

of the transverse momenta, even for the unpolarized FF D_1. Therefore, in order to obtain the Sivers function $f_{1T}^{\perp}$, Eq. (7.1) needs to be deconvoluted.

The observed asymmetries are expressed with $\sigma_{\mathcal{S}}$,

$$\text{Un-weighted:} \qquad A_{\mathcal{S}}(x,z) = \frac{\int dz\ d^2\boldsymbol{P}_{h\perp}\sigma_S(x,z,P_{h\perp})\ \varepsilon(x,z,P_{h\perp})}{\int dz\ d^2\boldsymbol{P}_{h\perp}\sigma_{UU}(x,z,P_{h\perp})\ \varepsilon(x,z,P_{h\perp})} \tag{7.2}$$

$$\text{Weighted:} \qquad \bar{A}_{\mathcal{S}}(x,z) = \frac{\int dz\ d^2\boldsymbol{P}_{h\perp}\left(\frac{P_{h\perp}}{zM}\right)\sigma_S(x,z,P_{h\perp})\varepsilon(x,z,P_{h\perp})}{\int dz\ d^2\boldsymbol{P}_{h\perp}\sigma_{UU}(x,z,P_{h\perp})\varepsilon(x,z,P_{h\perp})} \tag{7.3}$$

where $\varepsilon(x,z,P_{h\perp})$ is an acceptance function which describes geometrical and kinematical acceptance dependence for the detected hadrons at HERMES. In general the acceptance function can depend not only on x, z and $P_{h\perp}$ but also on Q^2, y and so on.

However we focus on the acceptance effect of $P_{h\perp}$, since, as seen in Eq. (7.1), the integration over $P_{h\perp}$ plays important roles for the deconvolution of the asymmetries. Thus we focus on the acceptance function for the transverse momentum of the hadrons.

7.1.1 Acceptance Effect on $P_{h\perp}$

Figure 7.1 shows x and $P_{h\perp}$ correlation. As presented in the figure, the mean value of $P_{h\perp}$ changes depending on x, and shape of the distribution also changes.

As pointed out in [61, 45], the transverse momentum of the quark can depend on x, so that the transverse momentum of the hadrons can also depend on x. However the kinematical correlation between x and $P_{h\perp}$ as in Fig. 7.1 does not originate only from physics but also include an acceptance effect.

To see the acceptance effect, we use unpolarized Monte Carlo simulation which has no information about x dependence of $\boldsymbol{p}_T$, so that $P_{h\perp}$ distribution of hadrons generated in 4π geometry do not have any x dependence of $P_{h\perp}$. Fig. 7.2 shows comparison of $P_{h\perp}$ distributions obtained in 4π geometry and in acceptance. The top panel of Fig. 7.2 shows the small $P_{h\perp}$ dependence on x in the 4π geometry. Due to technical problem of Monte Carlo simulation program, hadrons are generated not completely in 4π (but close to 4π).

The histograms in Fig. 7.2 shows that the $P_{h\perp}$ distributions in HERMES acceptance are systematically shifted to higher $P_{h\perp}$. This is due to the criteria of $\theta_{\gamma^* h}$ which suppress lower $P_{h\perp}$. Moreover in lower x-bins, the $P_{h\perp}$

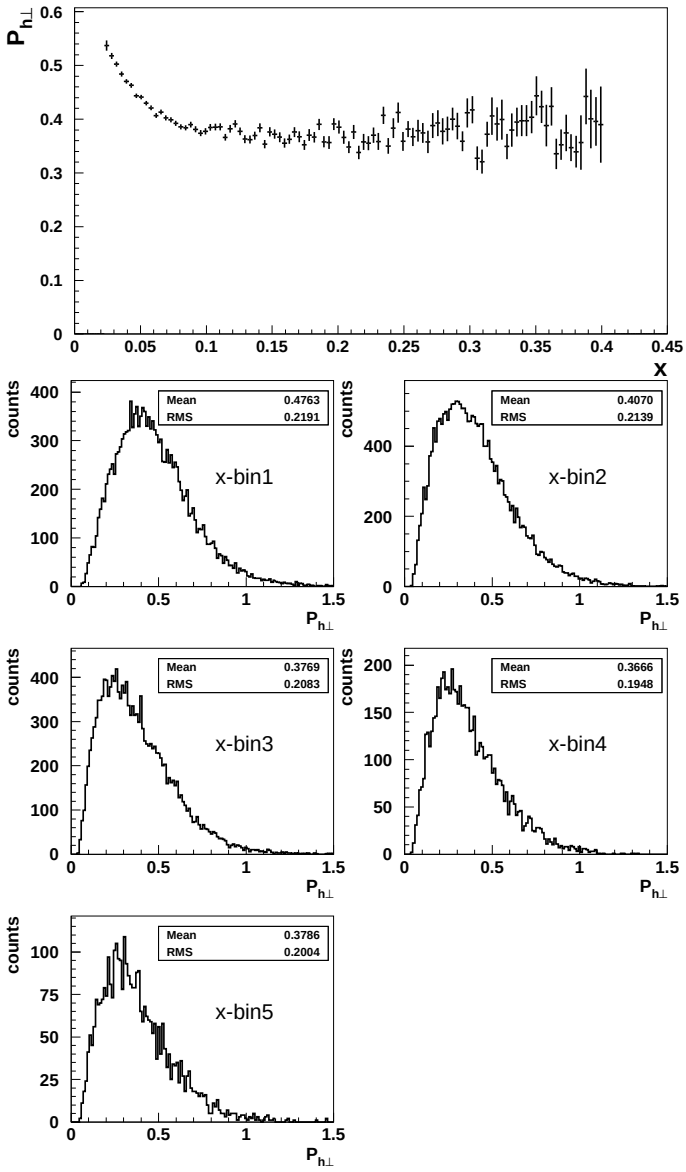

Figure 7.1: Correlation between x and $P_{h\perp}$ obtained from experimental data. Uppermost plot shows mean values of $P_{h\perp}$ (vertical axis) in each x point (horizontal axis), the error bars indicate RMS. Lower five histograms show $P_{h\perp}$ distribution in each x bin, the definition of x-binning is listed in Table 5.3.

distribution is broad compared to that of high x-bins. This is because a low x value corresponds to a small scattered angle, and therefore hadrons are produced in the direction close to the beam pipe in the low x events. In this case hadrons with low $P_{h\perp}$ go through the gap of the two detector halves and cannot be detected.

As the consequence of the acceptance effect on $P_{h\perp}$, we need to test whether the convolution integral are solved in the observed asymmetries.

7.1.2 Unweighted Asymmetries

The unweighted asymmetries are basically independent of the acceptance function because the acceptance effect cancels out when the ratio of the cross section is taken. Actually as already demonstrated in Section 5.2.2, the asymmetries obtained with the two-dimensional fit-method are consistent with the generated asymmetries. The unweighted asymmetries are, essentially, *pure* cross section asymmetries. Therefore they are not influenced by the acceptance effect.

On the other hand, the unweighted asymmetries cannot be expressed with a product of parton distribution and fragmentation functions (PDF's and FF's) like $f_{1T}^{\perp}(x)D_1(z)$, unless we assume Gaussian behavior of p_T and k_T. There is no proof to reject or justify the Gaussian assumption. In the present analysis the asymmetries are expressed with the deconvoluted form assuming the Gaussian,

$$A_{\mathcal{S}}(x) = -\frac{\sum_q e_q^2 \; f_{1T}^{\perp(1/2)q}(x) \int dz \; D_1^{q\to h}(z) \; \widetilde{\varepsilon}(x,z)}{\sum_q e_q^2 \; f_1^q(x) \int dz \; D_1^{q\to h}(z) \; \widetilde{\varepsilon}(x,z)} \tag{7.4}$$

$$\widetilde{\varepsilon}(x,z) \equiv \int d^2\boldsymbol{P}_{h\perp} \; \varepsilon(x,z,P_{h\perp})$$

where $\widetilde{\varepsilon}(x,z)$ is acceptance function but it is already integrated over $P_{h\perp}$. With an assumption of Gaussian distribution of p_T and k_T, the p_T-dependence of the Sivers function is completely separated from $f_{1T}^{\perp}(x)$. Hence the integration over the transverse momenta can be separately performed.

7.1.3 Weighted Asymmetries

In contrast to the unweighted asymmetries, it is theoretically clean to express the weighted asymmetry in the deconvoluted form. Similarly to unweighted

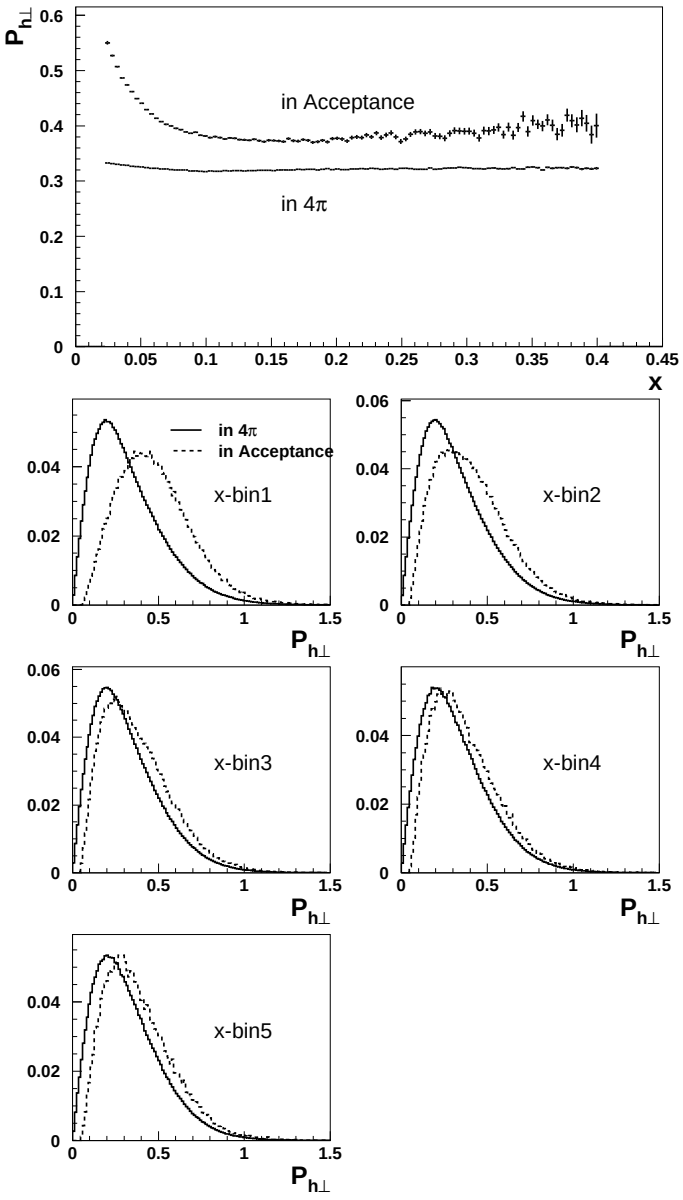

Figure 7.2: Correlation between x and $P_{h\perp}$ obtained from Monte Carlo data. The data in 4π geometry and in acceptance are superimposed. For the data in acceptance, the criteria adopted are the same as experimental data. In uppermost plot, the statistical mean value and RMS are displayed for 4π and for acceptance as labeled in the plot. Lower histograms show distribution of $P_{h\perp}$ in each x bin, solid histogram indicates 4π data and dashed histogram is obtained in acceptance. These histograms are normalized with their entries.

one's but using the first moment of the Sivers function $f_{1T}^{\perp(1)}$, the weighted asymmetry can be written,

$$\bar{A}_{\mathcal{S}}(x) = -\frac{\sum_q e_q^2 \; f_{1T}^{\perp(1)q}(x) \int dz \; D_1^{q\to h}(z) \; \widetilde{\varepsilon}(x,z)}{\sum_q e_q^2 \; f_1^q(x) \int dz \; D_1^{q\to h}(z) \; \widetilde{\varepsilon}(x,z)}. \tag{7.5}$$

This expression is obtained without any assumptions for the transverse momentum as detailed in Appendix A.

However as presented in Eq. (7.3), the acceptance effect of $P_{h\perp}$ may not be negligible for weighted asymmetries, since the weighted asymmetry is not a simple cross section ratio. The weighted asymmetry involves the $P_{h\perp}$ factor only in the numerator. One can have an idea to solve the acceptance problem, namely to apply the weight function of $P_{h\perp}$ to the denominator as well. It is unfortunately theoretically suggested that the $P_{h\perp}$-weighted unpolarized cross section cannot be resolved for the convolution integral,

$$\int d^2\boldsymbol{P}_{h\perp} |P_{h\perp}| \sigma_{UU} \not\propto f_1(x) \; D_1(z).$$

At the moment, no guidance is available to make sure that the observed asymmetries are deconvoluted. However there is an interesting attempt to test it.

Internal Consistency

For a test of the deconvolution, we apply the formula of Eq. (7.5) to the measured asymmetries, namely assuming that observed weighted asymmetry is completely deconvoluted. In this case, recalling Eq. (7.5), the asymmetries are expressed as,

$$\bar{A}_{\mathcal{S}}^h(x) = -\frac{\sum_q e_q^2 \; f_{1T}^{\perp(1)q}(x) \; \widetilde{D}_1^{q\to h}(x)}{\sum_q e_q^2 \; f_1^q(x) \; \widetilde{D}_1^{q\to h}(x)}, \tag{7.6}$$

$$\widetilde{D}_1^{q\to h}(x) \equiv \int_{0.2}^{0.7} dz \; D_1^{q\to h}(z) \; \widetilde{\varepsilon}(x,z), \tag{7.7}$$

$$\tag{7.8}$$

where index of sum q runs over u-, d-, $\bar{u}$- and $\bar{d}$-quarks. In addition to the above simplest formula Eq. (7.5), using charge conjugation and isospin invariance, we have two independent unpolarized fragmentation functions with

labels of fav and dis which are "favored" and "disfavored" fragmentation function respectively,

$$\begin{aligned} D^{fav} &\equiv D_1^{u\to\pi^+} \simeq D_1^{u\to\pi^+} \simeq D_1^{d\to\pi^-} \simeq D_1^{\bar{u}\to\pi^-} \simeq D_1^{\bar{d}\to\pi^+}, \\ D^{dis} &\equiv D_1^{u\to\pi^-} \simeq D_1^{u\to\pi^-} \simeq D_1^{d\to\pi^+} \simeq D_1^{\bar{u}\to\pi^+} \simeq D_1^{\bar{d}\to\pi^-} \\ \frac{1}{2}(D^{fav}+D^{dis}) &\equiv D_1^{u\to\pi^0} \simeq D_1^{d\to\pi^0} \simeq D_1^{\bar{u}\to\pi^0} \simeq D_1^{\bar{d}\to\pi^0}. \end{aligned}$$

This assumption is supported by an experimental result which is observed as multiplicity ratio of neutral pion to charged pions, $2n^{\pi^0}/(n^{\pi^-}+n^{\pi^+})$. It shows unity [87] at least in the z range used in this analysis.

Using D^{fav} and D^{dis} fragmentation functions, the asymmetries for each pions can be rewritten as follows,

$$\begin{aligned} \bar{A}_{\mathcal{S}}^{\pi^+}(x,z) &= -\frac{\sum_q e_q^2\, f_{1T}^{\perp(1)q}(x)\, D_1^{q\to\pi^+}(z)}{\sum_q e_q^2\, q(x)\, D_1^{q\to\pi^+}(z)} \\ &= -\frac{(4f_{1T}^{\perp(1)u}+f_{1T}^{\perp(1)\bar{d}})D^{fav}+(f_{1T}^{\perp(1)d}+4f_{1T}^{\perp(1)\bar{u}})D^{dis}}{(4u+\bar{d})D^{fav}+(d+4\bar{u})D^{dis}}, \qquad (7.9) \\ \bar{A}_{\mathcal{S}}^{\pi^-}(x,z) &= -\frac{(4f_{1T}^{\perp(1)u}+f_{1T}^{\perp(1)\bar{d}})D^{dis}+(f_{1T}^{\perp(1)d}+4f_{1T}^{\perp(1)\bar{u}})D^{fav}}{(4u+\bar{d})D^{dis}+(d+4\bar{u})D^{fav}}, \qquad (7.10) \\ \bar{A}_{\mathcal{S}}^{\pi^0}(x,z) &= -\frac{(4f_{1T}^{\perp(1)u}+f_{1T}^{\perp(1)\bar{d}}+f_{1T}^{\perp(1)d}+4f_{1T}^{\perp(1)\bar{u}})(D^{fav}+D^{dis})}{(4u+\bar{d}+d+4\bar{u})(D^{fav}+D^{dis})} \qquad (7.11) \end{aligned}$$

where $u(x), d(x), \bar{u}(x), \bar{d}(x)$ are unpolarized quark distributions of respective quarks. In the framework of this assumption, the three asymmetries of $\pi^{\pm}$ and π^0 have to satisfy the following relation,

$$\bar{A}_{\mathcal{S}}^{\pi^+}(x,z) + C(x,z)\bar{A}_{\mathcal{S}}^{\pi^-}(x,z) - (1+C(x,z))\bar{A}_{\mathcal{S}}^{\pi^0}(x,z) = 0 \qquad (7.12)$$

$$C(x,z) = \frac{r(x)+4\mathcal{D}(z)}{r(x)\mathcal{D}(z)+4} \qquad (7.13)$$

$$r(x) = \frac{d(x)+4\bar{u}(x)}{u(x)+\frac{1}{4}\bar{d}} \qquad (7.14)$$

$$\mathcal{D}(z) = \frac{D^{fav}(z)}{D^{dis}(z)} \qquad (7.15)$$

where $C(x,z)$ consists only of unpolarized objects and is possible to compute with the parametrization which is published and distributed. In this analysis CTEQ5 parton distribution function [88, 89] together with F_1, F_2 correction

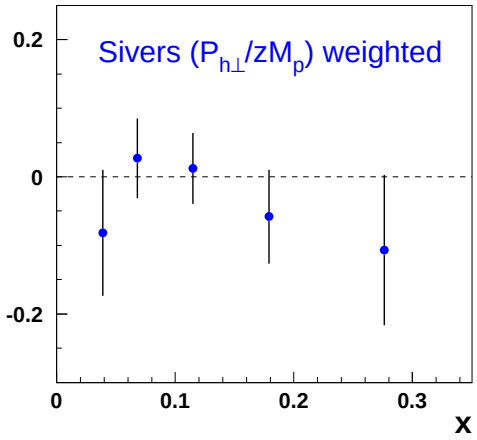

Figure 7.3: A consistency test. The results are from the weighted asymmetries. The vertical axis is the value of the left-hand side of Eq. (7.12).

factor for unpolarized structure function [90, 91] is used. For parameterization of fragmentation function, [92] is used.

The left-hand side of Eq. (7.12) was calculated for each x-bin. The results are shown in Fig. 7.3 as a function of x. As shown in Fig. 7.3, promisingly, the weighted asymmetries satisfy the relation Eq. (7.12) in the whole x region. From this result, the weighted asymmetries are deconvoluted at least within the statistical uncertainties.

It becomes even clearer if we look at average weighted asymmetries over the whole measured range;

$$\bar{A}_{\mathcal{S}}^{\pi^+}(\langle x\rangle,\langle z\rangle) + C(\langle x\rangle,\langle z\rangle)\bar{A}_{\mathcal{S}}^{\pi^-}(\langle x\rangle,\langle z\rangle) - (1+C(\langle x\rangle,\langle z\rangle))\bar{A}_{\mathcal{S}}^{\pi^0}(\langle x\rangle,\langle z\rangle) = -0.009 \pm 0.030.$$

where the corresponding mean values of the kinematics are; $\langle x\rangle = 0.09$, $\langle z\rangle = 0.36$ and $\langle Q^2\rangle = 2.40$ GeV^2.

7.2 Extracting Sivers Function

Encouraged with the result of the internal consistency test as shown in Fig. 7.3, we move on to the extraction of the Sivers function with the deconvoluted formula of the asymmetries.

7.2.1 Decomposition Procedure

Recalling the deconvoluted expression for weighted and unweighted asymmetries, Eqs. (7.5), (7.6) and (7.7), one can transform the formula. For example of weighted asymmetries,

$$\begin{aligned} \bar{A}^h_{\mathcal{S}}(x) &= -\sum_q \frac{e_q^2 f_1^q(x)\widetilde{D}_1^{q\to h}(x)}{\sum_{q'} e_{q'}^2 f_1^{q'}(x)\widetilde{D}_1^{q'\to h}(x)} \cdot \left(\frac{f_{1T}^{\perp(1)q}}{f_1^q}(x)\right) \\ &= -\sum_q P_q^h(x) \cdot \left(\frac{f_{1T}^{\perp,q}}{f_1^q}(x)\right) \qquad (7.16) \end{aligned}$$

$$P_q^h(x) \equiv \frac{e_q^2 f_1^q(x)\widetilde{D}_1^{q\to h}(x)}{\sum_{q'} e_{q'}^2 f_1^{q'}(x)\widetilde{D}_1^{q'\to h}(x)} \qquad (7.17)$$

where P_q^h can be interpreted as a probability that the virtual photon has struck a quark of type q when one observed a hadron h in the acceptance. This value is so-called *purity*. The acceptance function $\widetilde{\varepsilon}$ is confined in the purity. Using the purity formalism the asymmetry can be written as a linear combination of the Sivers functions ratio to unpolarized quark distribution function.

This probabilistic linear equations can be expressed with a matrix equation,

$$\overrightarrow{A} = P \cdot \overrightarrow{Q}. \qquad (7.18)$$

The vectors and the matrix here are defined as follows,

$$\overrightarrow{A} = \begin{pmatrix} A_{\mathcal{S}}^{\pi^+} \\ A_{\mathcal{S}}^{\pi^-} \\ A_{\mathcal{S}}^{\pi^0} \end{pmatrix}, \quad P = \begin{pmatrix} P_{q_1}^{\pi^+} & \cdots & P_{q_n}^{\pi^+} \\ P_{q_1}^{\pi^-} & \cdots & P_{q_n}^{\pi^-} \\ P_{q_1}^{\pi^0} & \cdots & P_{q_n}^{\pi^0} \end{pmatrix}, \quad \overrightarrow{Q} = \begin{pmatrix} \frac{f_{1T}^{\perp(1)q_1}}{f_1^{q_1}} \\ \vdots \\ \frac{f_{1T}^{\perp(1)q_n}}{f_1^{q_n}} \end{pmatrix}. \qquad (7.19)$$

where the index of q indicates the quark types. In this analysis the possible contributions of $u, d, \bar{u}$ and $\bar{d}$ quarks are considered.

Based on the approximation of $favored$ and $disfavored$ fragmentation functions, the expression of the asymmetry can be rewritten. For example,

π^+ asymmetry is,

$$
\begin{aligned}
A_{\mathcal{S}}^{\pi^+}(x) &= -\frac{\left(e_u^2 f_1^u(x) + e_{\bar{d}}^2 f_1^{\bar{d}}(x)\right)\widetilde{D}^{fav}(x)}{\sum_{q'} e_{q'}^2 f_1^{q'}(x)\widetilde{D}_1^{q'\to h}(x)} \cdot \left(\frac{e_u^2 f_{1T}^{\perp(1)u} + e_{\bar{d}}^2 f_{1T}^{\perp(1)\bar{d}}}{e_u^2 f_1^u + e_{\bar{d}}^2 f_{1T}^{\bar{d}}}\right) \\
&\quad - \frac{\left(e_d^2 f_1^u(x) + e_{\bar{u}}^2 f_1^{\bar{u}}(x)\right)\widetilde{D}^{dis}(x)}{\sum_{q'} e_{q'}^2 f_1^{q'}(x)\widetilde{D}_1^{q'\to h}(x)} \cdot \left(\frac{e_d^2 f_{1T}^{\perp(1)d} + e_d^2 f_{1T}^{\perp(1)\bar{u}}}{e_d^2 f_1^d + e_d^2 f_{1T}^{\bar{u}}}\right),
\end{aligned}
\tag{7.20}
$$

$$
\widetilde{D}^{fav,dis}(x) \equiv \int_{0.2}^{0.7} D^{fav,dis}(z)\ \widetilde{\varepsilon}(x,z). \tag{7.21}
$$

In this way, the purities are summed for the respective quark types, e.g. $P_{u+\bar{d}}^{\pi^+} = P_u^{\pi^+} + P_{\bar{d}}^{\pi^+}$. Then the free parameters of the matrix equation is reduced to only two,

$$
\overrightarrow{Q}^T = \begin{pmatrix} \dfrac{f_{1T}^{\perp(1)u} + \frac{1}{4} f_{1T}^{\perp(1)\bar{d}}}{f_1^u + \frac{1}{4} f_{1T}^{\bar{d}}} & \dfrac{f_{1T}^{\perp(1)d} + 4 f_{1T}^{\perp(1)\bar{u}}}{f_1^d + 4 f_{1T}^{\bar{u}}} \end{pmatrix} \tag{7.22}
$$

The solution of $\overrightarrow{Q}$ is obtained by searching for the minimum χ^2, which is defined

$$
\chi^2 = (\overrightarrow{A} - P \cdot \overrightarrow{Q})^T C_A^{-1} (\overrightarrow{A} - P \cdot \overrightarrow{Q}) \tag{7.23}
$$

where C_A is a covariance matrix of the asymmetries. This covariance matrix takes into account the statistical correlation between asymmetries. The element of the matrix $(C_A)_{ij}$ consists of statistical uncertainties of the asymmetries and correlation coefficient ρ_{ij} between hadron type of i and j,

$$
(C_A)_{ij} = \rho_{ij}\ \delta A_{\mathcal{S}}^{h_i} \cdot \delta A_{\mathcal{S}}^{h_j}. \tag{7.24}
$$

so that diagonal elements of the covariance matrix is just given by squared statistical uncertainties,

$$
(C_A)_{jj} = \left[\delta A_{\mathcal{S}}^{h_j}\right]^2 \tag{7.25}
$$

For the off-diagonal elements, the statistical correlation coefficients ρ_{ij} can be related to averaged hadron multiplicities in each event $\langle n^{h_i} \rangle$

$$
\rho_{ij} = \mathrm{Cor}(A_{\mathcal{S}}^{h_i}, A_{\mathcal{S}}^{h_j}) = \frac{\langle n^{h_i} n^{h_j} \rangle}{\sqrt{\langle (n^{h_i})^2 \rangle \langle (n^{h_j})^2 \rangle}}. \tag{7.26}
$$

To obtain the covariance matrix, each element is integrated over kinematics of ϕ, ϕ_S and z. Especially for correlation coefficient which includes π^0, the $\langle n^{\pi^\pm} n^{\pi^0} \rangle$ value is obtained by weighting the π^0 candidate with SN-ratio used in background correction of the asymmetry Eq. (5.39).

In general, the minimum χ^2 of Eq. (7.23) is given by $\partial\chi^2/\partial\overrightarrow{Q} = 0$, so that the covariance matrix C_Q of solution $\overrightarrow{Q}$ can be computed by

$$C_Q = \left[\left(P^T C_A^{-1} P \right)^{-1} P^T C_A^{-1} \right] C_A \left[\left(P^T C_A^{-1} P \right)^{-1} P^T C_A^{-1} \right]^T. \tag{7.27}$$

The statistical uncertainties of $\overrightarrow{Q}$ is given by square-root of the diagonal elements of the covariance matrix,

$$\delta \left(\overrightarrow{Q} \right)_j = \sqrt{(C_Q)_{jj}}. \tag{7.28}$$

7.2.2 Purity and Acceptance Effect on z

The purity is basically acceptance dependent function of x. Actually the similar plot as Fig. 7.1, but correlation between x and z in the data is shown in Fig. 7.4.

For evaluation of the acceptance dependent purities, unpolarized Monte Carlo simulation is used. As the inputs of the Monte Carlo simulation, a parametrization of parton distribution function and Lund string model are employed. The parton distribution function uses CTEQ5 parameterization, and the string model is based on data from e^+e^- experiments and is finely tuned to reproduce HERMES data. In the simulation, the detected hadrons of type h are collected with tagging the struck quark type q. The collected number of detected hadron N_q^h is related with PDF's and FF's

$$N_q^h(x) \;\propto\; e_q^2 \, f_1^q(x) \int dz \; D_1^{q\to h}(z) \; \widetilde{\varepsilon}(x,z). \tag{7.29}$$

The acceptance dependent purity can be calculated as

$$P_q^h(x) \equiv \frac{N_q^h(x)}{\sum_q N_q^h(x)}. \tag{7.30}$$

Fig. 7.5 shows the purity evaluated with Monte Carlo which takes into account the acceptance effect. Also the purities are shown in the figure, which are calculated with product of parametrization of PDF's and FF's (no acceptance effect included) with the different FF parametarizations. In the

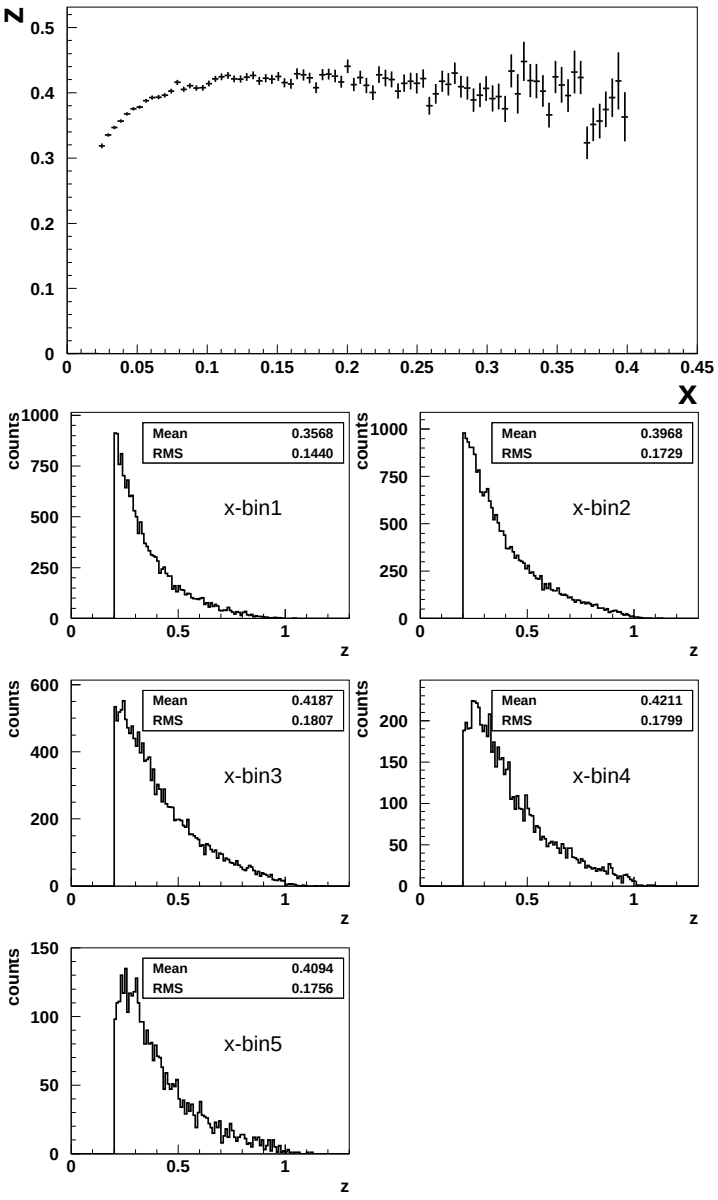

Figure 7.4: Correlation between x and z obtained from experimental data. In the plots, the upper z cut is not applied. z value exceeds 1 in some events due to smearing and resolution effects of the detector.

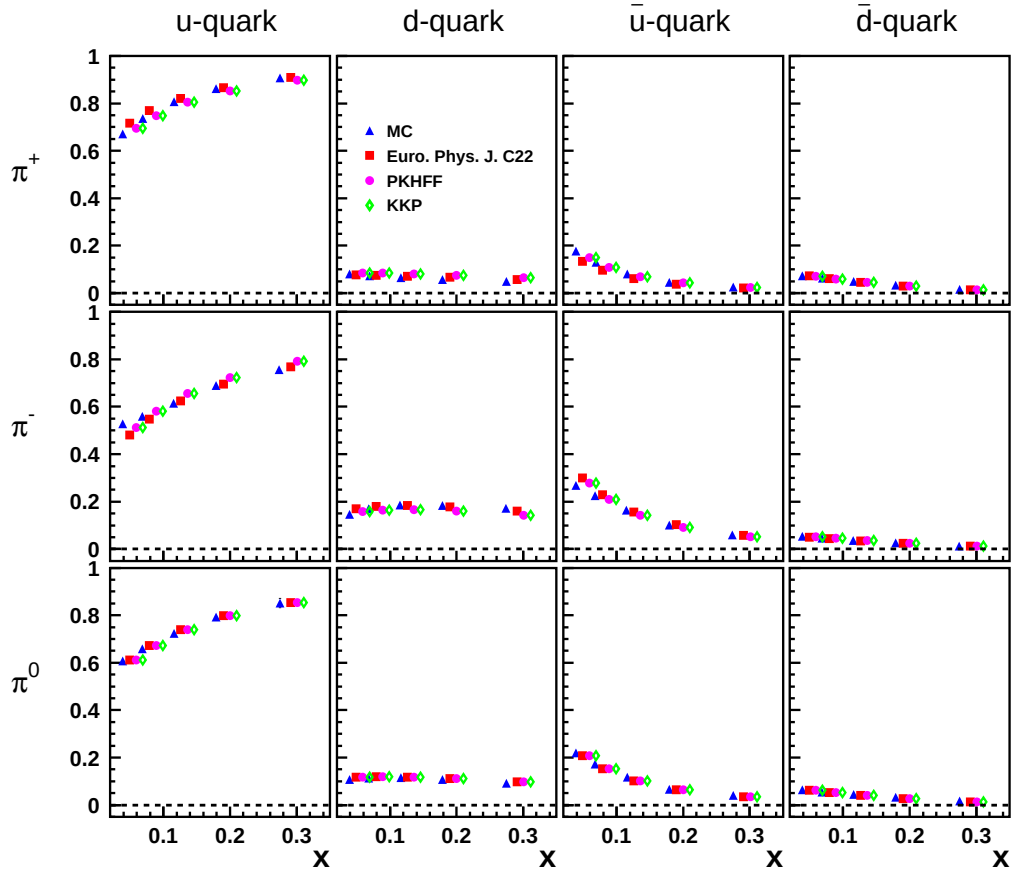

Figure 7.5: Comparison of purities evaluated with Monte Carlo which takes into account the detector acceptance (triangle). All others are evaluated as a product of PDF's and FF's, where the FF's of different type of parametrization were used; [92](square), [93](circle), [94](rhombus). Note : for all evaluated purity, the identical PDF (CTEQ5) is used to see the acceptance effect on z.

comparison in Fig. 7.5, all calculated purities use the same PDF parameterization as used in the Monte Carlo.

Although there is small differences between acceptance dependent purity and ideal purities, they show almost consistent values. The small differences are of the same magnitude as that between the respective parameterizations of fragmentation functions.

7.3 Results

7.3.1 The Sivers Functions as Ratio to Unpolarized PDF

Using the asymmetries in charged and neutral pion production and the purities presented in Fig. 7.5 as inputs, one can decompose the Sivers asymmetries to the individual quark flavor contributions. Due to limited statistics, the Sivers functions are extracted for the combination of the quark types; $u + \frac{1}{4}\bar{d}$ and $d + 4\bar{u}$ as explained in Eq. (7.20).

Figure 7.6 shows the results of Sivers functions as a ratio to the unpolarized parton distribution function. These have been extracted using several types of purities evaluated in Fig. 7.5.

The difference in the results in Fig. 7.6 originates only from fragmentation function evaluated with Monte Carlo and with parameterizations since the input PDF parametrization is identical for all the purities. Depending on the fragmentation function (actually purity), the statistical uncertainties of results can be different. As the result, the error propagation to the results is, roughly speaking, expressed as; $\delta\bar{A}_{\mathcal{S}} \sim \sum_q P_q^h \delta(f_{1T}^{\perp}/f_1)$ where $\delta\bar{A}_{\mathcal{S}}$ indicates statistical uncertainties of asymmetry, $\delta(f_{1T}^{\perp}/f_1)$ is statistical uncertainties of the Sivers function ratio to unpolarized PDF.

In the following analysis, the purities evaluated with Monte Carlo will be used.

7.3.2 The Extracted Sivers Functions

The Sivers function can be obtained by multiplying unpolarized parton distribution to Fig. 7.6. The Sivers function itself should have a Q^2-dependence as other parton distribution functions have. However the Q^2-evolution equations for the Sivers function have not been established yet. Looking at Fig. 5.22, the observed Sivers asymmetries as functions of Q^2 show no clear Q^2-dependence. The event distribution in Q^2 is very narrow. The mean

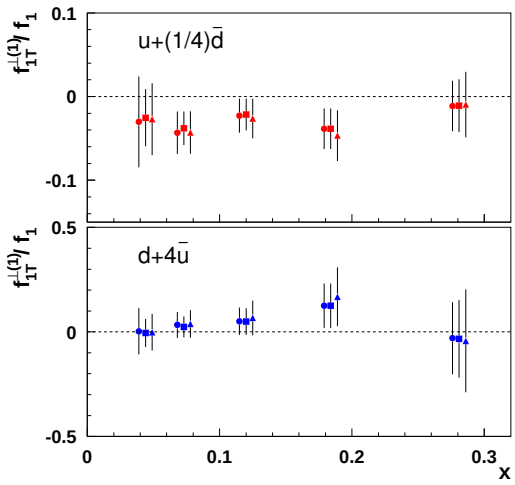

Figure 7.6: Results of the Sivers function as ratio to the unpolarized quark distribution function using different purities evaluated with Monte Carlo (circle), [93] (squared), [92] (triangle). For all purities the same parameterization of parton distribution function CTEQ5 [88] is used.

value of the Q^2 is found to be $\langle Q^2 \rangle = 2.4$ GeV^2. Therefore in this analysis it is assumed that the Q^2-dependence of the Sivers function as ratio to unpolarized PDF is very small for the whole x-bins.

The Sivers functions $f_{1T}^{\perp}(x, Q_0^2)$ are obtained from Fig. 7.6 by multiplying unpolarized parton distribution function $f_1(x, Q_0^2)$ at fixed scale of Q_0^2. The unpolarized quark distributions are taken from CTEQ5LO which is used also in purity evaluation. The Sivers functions have been determined at a fixed scale of $Q_0^2 = 2.4$ GeV^2. Figure 7.7 shows the extracted Sivers function for the different quark type combinations, $u + \frac{1}{4}\bar{d}$ and $d + 4\bar{u}$. Fig. 7.8 shows also the extracted Sivers function for u- and d-quark neglecting sea-quark's contributions (set to $f_{1T}^{\perp(1)\bar{u}} = f_{1T}^{\perp(1)\bar{d}} = 0$). As shown in Fig. 7.8, the extracted Sivers functions are consistent even if the sea-quark contributions are neglected. With help of Fig. 7.5, this result can be interpreted that most of all hadrons originates from u-quarks. Within the current statistics, sea-quark contribution to Sivers asymmetries is not significant. Therefore, we can determine Sivers function for u-quark safely. As the consequence, the Sivers function for u-quark is found negative, and d-quark contains positive value.

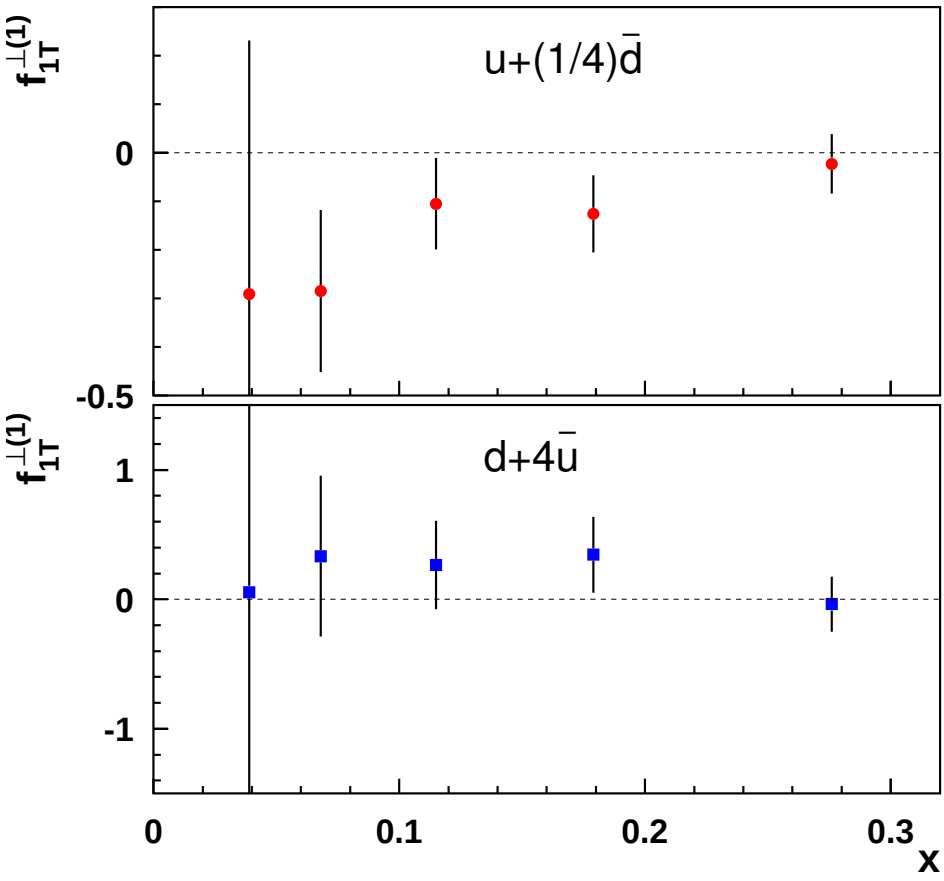

Figure 7.7: The extracted Sivers functions for two flavor-charge combinations $u + \frac{1}{4}\bar{d}$ (upper panel) and $d + 4\bar{u}$ (lower panel). The error bars represent statistical uncertainties.

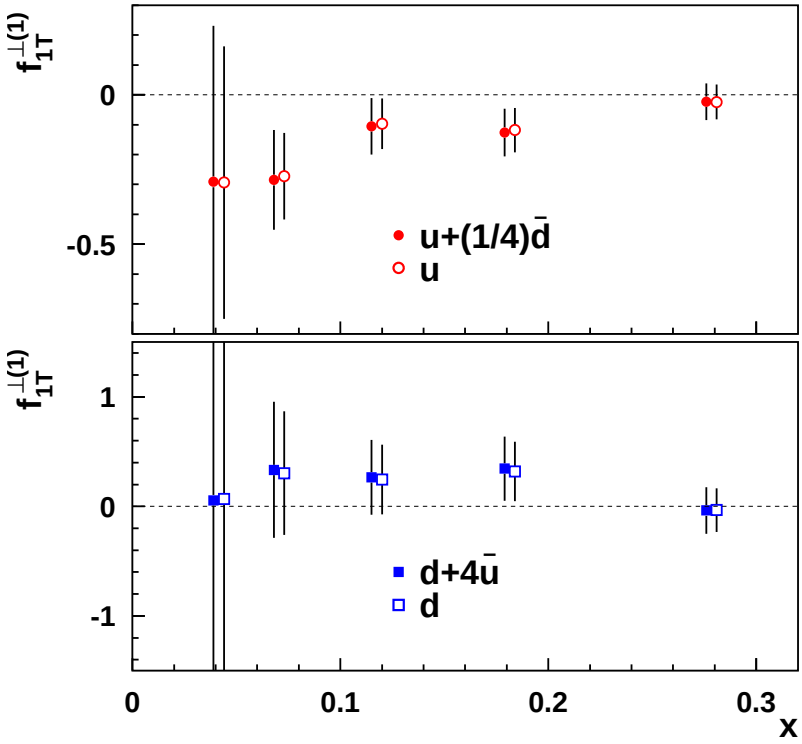

Figure 7.8: Comparison of the extracted Sivers functions for $u + \frac{1}{4}\bar{d}$ and $d + 4\bar{u}$ combination with Sivers functions of u- and d-quark neglecting sea-quark contributions ($f_{1T}^{\perp(1)\bar{u}} = f_{1T}^{\perp(1)\bar{d}} = 0$).

Moreover the extracted Sivers functions using unweighted asymmetries with the assumption that the convolution is resolved are shown in Fig. 7.9. The Sivers function using unweighted and weighted asymmetries are fully consistent within the statistical uncertainties. This results will be discussed in Section 7.3.5.

7.3.3 Systematic Studies

Combination of the Input Asymmetries

For the decomposition to $u + \frac{1}{4}\bar{d}$ and $d + 4\bar{u}$, any combinations of input as asymmetries can be used. Results from different options are compared. In Fig. 7.10, one can find the results obtained using all the asymmetries of $\pi^{\pm}$

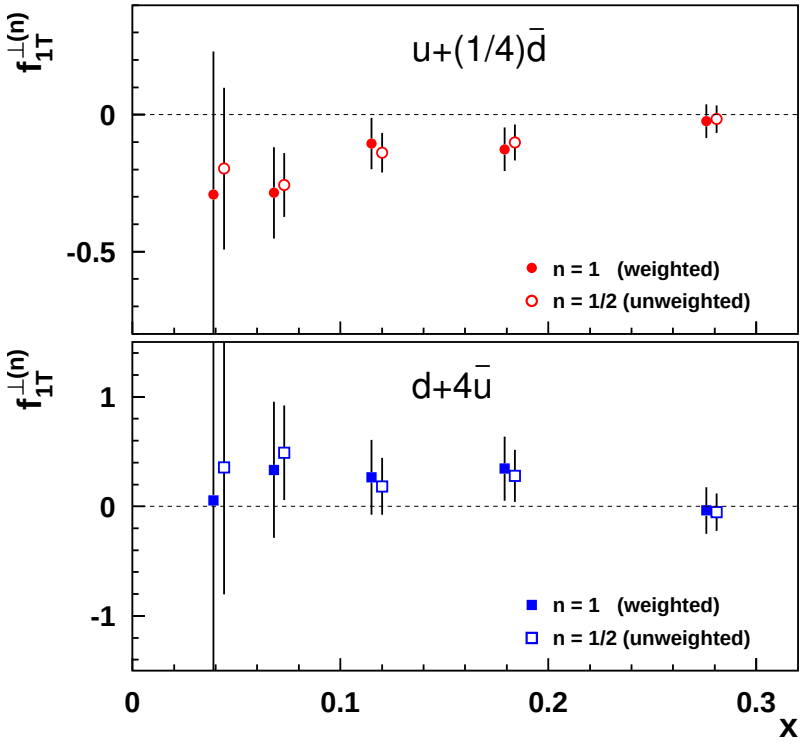

Figure 7.9: The extracted Sivers functions for two flavor-charge combinations $u + \frac{1}{4}\bar{d}$ (circle) and $d + 4\bar{u}$ (square). Both the extracted Sivers function from weighted (solid) and unweighted asymmetries (open) are plotted. The moment "$n = 1/2$" is obtained from unweighted asymmetries assuming the Gaussian distribution of transverse momentum p_T and k_T.

and π^0, and the results using the asymmetries $\pi^\pm$ only.

Smearing effect

As already demonstrated in Chapter 6, the unweighted asymmetries for charged pions which are corrected for smearing effects are available. In Fig. 7.11, a comparison of the Sivers functions obtained from asymmetries with and without the smearing correction is shown. At the lowest x-bin, the Sivers functions with smearing correction is largely fluctuates. The largest contribution to this behavior originates from multiplying the unpolarized PDF. At lowest x-bin, the unpolarized PDF becomes as large as 7 - 9, thus

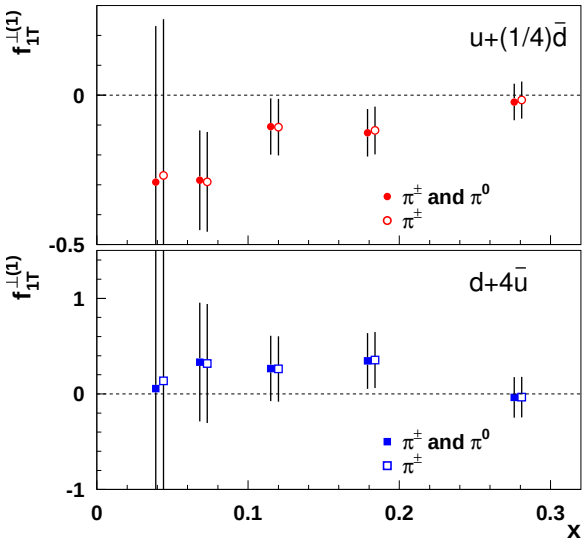

Figure 7.10: Comparison of the Sivers functions obtained using all the asymmetries for $\pi^{\pm}$, π^0 (closed marks) and those obtained using asymmetries for $\pi^{\pm}$ (open marks) only.

even with small amount of the effect of smearing can be large.

7.3.4 Comparison with Theoretical Predictions

In Fig. 7.12, a comparison between extracted Sivers functions of u- and d-quarks with three theoretical predictions is presented. The theoretical prediction are as already explained in Section 3.4.

In the prediction [57], the Sivers function is obtained from a phenomenological studies of single-spin asymmetry A_N in $p^{\uparrow}p$ collision of E704 expeirment. The sing of the predicted Sivers functions is consistent with the results of this thesis[1]. However the prediction of $f_{1T}^{\perp(1)u,d}$ has been obtained from a parameterization [56] which assumes that observed asymmetries for $\pi^{\pm}$ and π^0 production are only associated with Sivers effect. As mentioned in Section 5.6, the observed A_N involves both Sivers and Collisn effects, and they, basically, cannot be disentangled in proton-proton collision. Moreover in different theoretical studies [79, 80], non-negligible higher-twist contributes

[1]It should be noted that the sign of the Sivers functions is set to opposite to those in the paper [57] according to the reference [46].

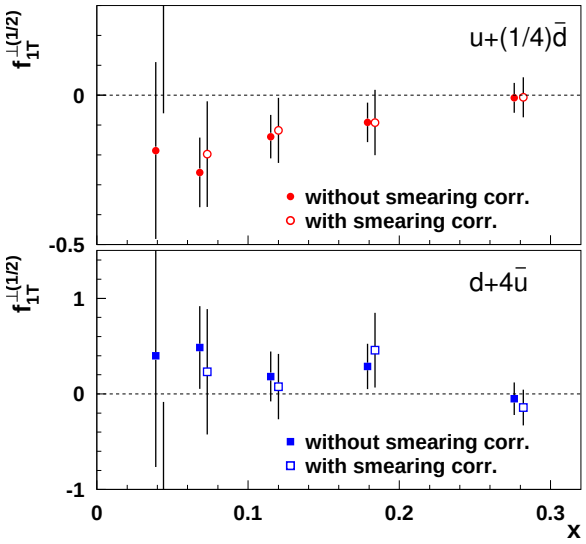

Figure 7.11: Comparison between the extracted Sivers functions using unweighted $\pi^{\pm}$ asymmetries without (closed marks) and with smearing correction (open marks).

to A_N in proton-proton collision is suggested. Thus the comparison needs careful investigations.

Universality

As mentioned in Section 5.6, the A_N for π^0 production in proton-proton collision measured at STAR experiment shows the similar results to E704's even in different energy scale. As discussed in the reference [95], partonic reaction, $qg \to qg$ and $gg \to gg$, is dominant in inclusive measurement of the π^0 production in the STAR acceptane.

When the universality on gauge link structure is considered [52, 48], it is expected that the results of Sivers function obtained from DIS and from Drell-Yan processes (e.g. $q\bar{q} \to q\bar{q}$) have opposite sign. However universality for the reactions, $qg \to qg$ and $gg \to gg$, are not yet clear [48]. More theoretical studies are needed.

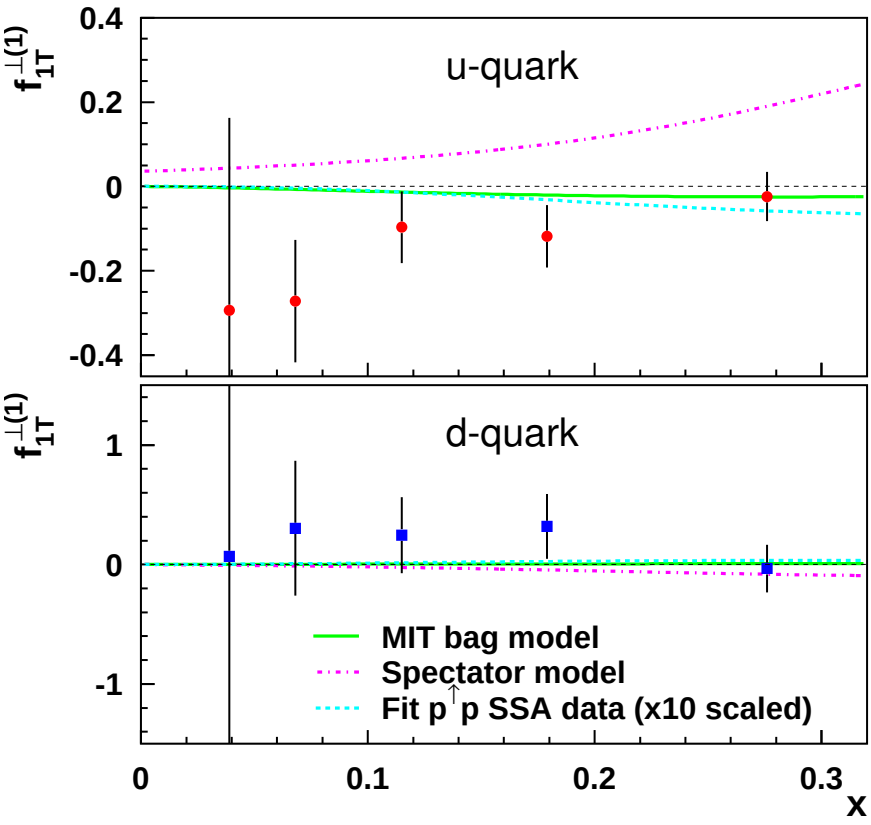

Figure 7.12: Comparison of the extracted Sivers function neglecting sea-quark contributions with three theoretical predictions described in Section 3.4. Note that the prediction of "Fit $p^{\uparrow}p$ SSA data" is 10 times scaled.

7.3.5 Discussion

For unweighted asymmetries, a Gaussian distribution of the p_T and k_T is assumed. Then, the result of Fig. 7.9 is obtained, and it indicates $f_{1T}^{\perp(1)} \simeq f_{1T}^{\perp(1/2)}$. To discuss adequateness of Gaussian assumption, a similar test to Fig. 7.3 is performed for unweighted asymmetries. The left-hand side of Eq. (7.12) are computed with the same inputs as used in Fig. 7.3. Figure 7.13 presents the result.

Looking at the results in Fig. 7.13, the internal consistency is not satisfactory. However the Gaussian assumption of the transverse momenta especially for p_T could be valid for part of x-region. For example in the limit of $x \sim 1$,

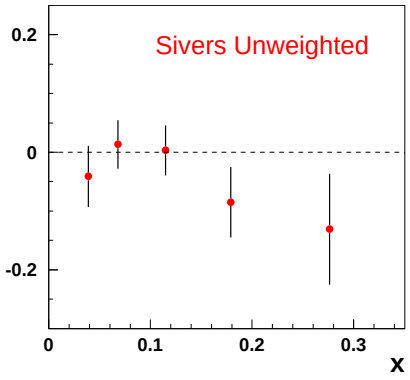

Figure 7.13: A consistency test. The result is from unweighted asymmetries.

the quarks probably cannot have p_T, but in lower x-region it could be allowed to have transverse momentum of Gaussian type,

$$f_{1T}^{\perp}(x, \boldsymbol{p}_T^2) \equiv f_{1T}^{\perp}(x) \left(\frac{\exp\left(-\boldsymbol{p}_T^2/\langle \boldsymbol{p}_T^2 \rangle\right)}{\pi \langle \boldsymbol{p}_T^2 \rangle} \right) \tag{7.31}$$

The definition of the moment of the Sivers function is given in Eq. (3.13) and Eq. (3.16). Based on the Gaussian assumption, we obtained an expression of the moments of the Sivers function for $n = 1$ and $n = 1/2$,

$$f_{1T}^{\perp(1)}(x) = \frac{1}{4M_p} \sqrt{\pi \langle p_T^2 \rangle} f_{1T}^{\perp}(x) \tag{7.32}$$

$$f_{1T}^{\perp(1/2)}(x) = \frac{\langle p_T^2 \rangle}{2M_p^2} f_{1T}^{\perp}(x). \tag{7.33}$$

Here we have results of $f_{1T}^{\perp(1)} \simeq f_{1T}^{\perp(1/2)}$. This result yields,

$$\frac{f_{1T}^{\perp(1)}}{f_{1T}^{\perp(1/2)}} = \frac{2\sqrt{\langle p_T^2 \rangle}}{M_p \sqrt{\pi}} \sim 1 \tag{7.34}$$

From this relation, we can estimate the width $\langle p_T^2 \rangle$ of the distribution of quark intrinsic transverse momentum as $\langle p_T^2 \rangle \sim 0.7$ (GeV/c)^2. The Gaussian assumption leads to the relation of $\langle p_T^2 \rangle = 4\langle p_T \rangle / \pi$. Thus one can obtain the average of the transverse momentum as $\langle p_T \rangle \sim 0.7$ GeV/c.

This result looks very large, because the average intrinsic transverse momentum can be expected to be a few 100 MeV from Heisenberg uncertainty principle for the quarks confined in the nucleon with radius of $r_p \simeq 0.81$

fm. However such large intrinsic transverse momentum $\langle p_T \rangle$ have been reported in other papers [96, 97]. In reference [96], the $\langle p_T \rangle = 848$ MeV/c was extracted by applying fit with Gaussian assumption of p_T distribution to experimental data of Drell-Yan $\mu^+\mu^-$-production of proton-proton collision ($pp \to \mu^+\mu^- X$) at $\sqrt{s} = 27.4$ GeV. Reference [97] have reported the transverse momentum of $\langle p_T \rangle \sim 1$ GeV/c which was extracted from jet-jet angular distribution in proton-proton and proton-nucleus reactions with the proton beam of 400 GeV.

There are other results on $\langle p_T \rangle$ extracted from experimental data with parameterization based on Gaussian assumption. They also observed rather a large transverse momentum of $1-2$ GeV/c (e.g. references [98, 99]). However, there are also some alerts for the large transverse momentum, which point out contributions of some additional mechanisms which enlarge *observed* transverse momentum. According to references [100]–[104], the extracted (observed) transverse momentum from experimental data is around $\langle p_T \rangle_{obs} 1-2$ GeV/c, but it is obtained from *real* intrinsic transverse momentum of $\langle p_T \rangle_{real} \sim 0.2 - 0.4$ GeV *plus* some supplemental contributions, such as soft gluon emission. It still leaves room for a variety of interpretations for the large transverse momentum. Some interesting interpretations on it can be found in Chapter B.

In addition to above, for the intrinsic transverse momentum of quarks (and hadrons), there are many other approaches and studies [105] –[110], but at this moment, there is no unified view on it yet. It needs further investigations.

Chapter 8

Conclusion

HERMES is a deep inelastic scattering experiment with positron beam at DESY-HERA. Transversely polarized proton target and unpolarized positron beam were used for the present study.

The HERMES experiment has measured the single-spin asymmetries associated with the Sivers and Collins mechanisms with semi-inclusive measurement of $\pi^{\pm}$, π^0. In this thesis, the observed Sivers and Collins type asymmetries in $\pi^{\pm}$ and π^0 production are reported.

The resulting, Collins and Sivers type asymmetries have following characterizations,

- **Collins asymmetries:**
  - The asymmetry for π^- is negative with more than 3σ significance,
  - The asymmetry for π^+ is positive with 2σ level,
  - The asymmetry for π^0 is almost zero.
- **Sivers asymmetries:**
  - The asymmetry for π^+ is positive with 3σ significance,
  - The asymmetry for π^0 is positive with 2σ level,
  - The asymmetry for π^- is consistent with zero with in the statistical uncertainties.

Smearing effect due to finite momentum/energy resolution of the detector and radiative effect was corrected for the observed asymmetries. It was found that the magnitude of the correction are small compared with the statistical uncertainties.

It is theoretically suggested that the diffractive vector meson, ρ^0 and ω, contributions can influence the semi-inclusive pion sample. The diffractive

events can also make azimuthal asymmetry, and the observed Sivers and Collins asymmetries could contain systematic contribution from them. This is a theoretical and experimental open question at the moment and further studies are needed.

From the observed Sivers asymmetries for $\pi^{\pm}$ and π^0, the Sivers quark distribution functions were then actually extracted. The Sivers functions for different quark types have been extracted for the first time. With assumption of the isospin symmetry for the fragmentation function of pions, the Sivers function for quark type combination of $f_{1T}^{\perp(1)u} + \frac{1}{4} f_{1T}^{\perp(1)\bar{d}}$ and $f_{1T}^{\perp(1)d} + 4 f_{1T}^{\perp(1)\bar{u}}$ are extracted. At the same time, the Sivers functions of u- and d-quarks are also extracted neglecting sea-quark contributions ($f_{1T}^{\perp(1)\bar{u}} = f_{1T}^{\perp(1)\bar{d}} = 0$). The extracted Sivers functions with and without the assumption of $f_{1T}^{\perp(1)\bar{u}} = f_{1T}^{\perp(1)\bar{d}} = 0$ are fully consistent within the statistical uncertainties. In the result, the Sivers function of u-quark is negative and d-quark is slightly positive.

If the Sivers function can be related to the orbital angular momentum of quarks in proton as was suggested in theories, the present result will provide a new insight to the nucleon spin problem.

Acknowledgments

During my study at Tokyo Institute of Technology and at DESY, Hamburg, I was helped by a lot of people. I would like to express my thanks to all the people who supported me.

First of all, I would like to thank Prof. Toshi-Aki Shibata who motivated me to join the HERMES collaboration and provided me many advices. I am indebted to Dr. Yoshiyuki Miyachi for his valuable advice and suggestions during my entire studies. I wish to express my thanks to Dr. Gunar Schnell. His many advices and critical comments towards the completion of this work were indispensable.

My thanks are also due to all the members of HERMES collaborators with whom I worked, notably Ulrike Elschenbroich. Her helps and advices were crucial for the completion of the asymmetry analyses. Many thanks to Dr. Maurice Bouwhuis gave me a lot of advices and helps when I wrote a paper on Gain Monitoring System.

I would also like to express my thank to the members of Tokyo Tech group, especially, Hiroshi Ohsuga, he and I had good discussions on HERMES experiment and physics. Tomohiro Kobayashi had many occasions to discuss my study with me. It was very helpful for me.

Additionally, I thank the members of the HERMES Collaboration. Particularly, Dr. Elke-Caroline Aschenauer gave me a lot of advices and helps. I received a lot of helps from the HERMES collaborators. Thanks to all of them.

Appendix A

Resolving Convolution Integral

A.1 Weighted Cross-section Asymmetry (Sivers type)

Transversity h_1, Collins fragmentation function $H_1^\perp$, Sivers function $f_{1T}^\perp$ and spin averaged fragmentation function D_1, their moment of the transverse momenta are defined as follows:

$$h_1^{(1)}(x) = \int d^2\boldsymbol{p_T} \left(\frac{{\boldsymbol{p_T}}^2}{2M_N^2}\right) h_1(x, {\boldsymbol{p_T}}^2) \tag{A.1}$$

$$H_1^{\perp(1)}(x) = z^2 \int d^2\boldsymbol{k_T} \left(\frac{{\boldsymbol{k_T}}^2}{2M_h^2}\right) H_1^\perp(z, z^2{\boldsymbol{k_T}}^2) \tag{A.2}$$

$$f_{1T}^{\perp(1)}(x) = \int d^2\boldsymbol{p_T} \left(\frac{{\boldsymbol{p_T}}^2}{2M_N^2}\right) f_{1T}^\perp(x, {\boldsymbol{p_T}}^2) \tag{A.3}$$

$$D_1(z) = z^2 \int d^2\boldsymbol{k_T} D_1(z, z^2{\boldsymbol{k_T}}^2) \tag{A.4}$$

The Weighted Sivers type cross section can be written as follows,

$$\int d^2\boldsymbol{P_{h\perp}} \left(\left[\frac{P_{h\perp}}{zM_N}\right] \cdot d\sigma_{UT}^{\text{Sivers}} \right) \equiv -\frac{2\alpha^2}{sxy^2} A(y) \sum_q e_q^2 \; I_q, \tag{A.5}$$

$$\begin{aligned} I_q &\equiv \frac{1}{z} \int d^2\boldsymbol{P_{h\perp}} \int d^2\boldsymbol{p_T} \left(\frac{\boldsymbol{p_T}\cdot\boldsymbol{P_{h\perp}}}{M_N^2}\right) f_{1T}^{\perp q}(x, {\boldsymbol{p_T}}^2) \int d^2\boldsymbol{k_T} D_1(z, z^2{\boldsymbol{k_T}}^2) \\ &\quad \times\delta^{(2)}(\boldsymbol{p_T} - \boldsymbol{k_T} - \frac{\boldsymbol{P_{h\perp}}}{z}) \qquad (A.6) \\ &= \frac{1}{z} \int dP_{h\perp 1}\; dP_{h\perp 2} \int dp_{T1}\; dp_{T2} \left(\frac{p_{T1}P_{h\perp 1} + p_{T2}P_{h\perp 2}}{M_N^2}\right) f_{1T}^\perp(x, p_{T1}^2 + p_{T2}^2) \\ &\quad \times \int dk_{T1}\; dk_{T2}\; D_1(z, z^2k_{T1}^2 + z^2k_{T2}^2)\delta(p_{T1} - \frac{P_{h\perp 1}}{z} - k_{T1})\delta(p_{T2} - \frac{P_{h\perp 2}}{z} - k_{T2}). \end{aligned}$$

where $\boldsymbol{p_T} \cdot \boldsymbol{P_{h\perp}} = p_{T1}P_{h\perp 1} + p_{T2}P_{h\perp 2}$, is used. So we separate above equation to two terms, $I_q = I_q\Big|_1 + I_q\Big|_2$.

The term of $I_q\Big|_1$ is defined as follows:

$$
\begin{aligned}
I_q\Big|_1 &= \frac{1}{z}\int dP_{h\perp 1}\; dP_{h\perp 2}\; \int dp_{T1}\; dp_{T2}\; \left(\frac{p_{T1}P_{h\perp 1}}{M_N^2}\right) f_{1T}^{\perp}(x, p_{T1}^2 + p_{T2}^2) \\
&\quad \times \int dk_{T1}\; dk_{T2}\; D_1(z, z^2k_{T1}^2 + z^2k_{T2}^2)\delta(p_{T1} - \frac{P_{h\perp 1}}{z} - k_{T1})\delta(p_{T2} - \frac{P_{h\perp 2}}{z} - k_{T2}) \\
&= \int dp_{T2}\; dk_{T2}\; dP_{h\perp 2}\; \delta(p_{T2} - \frac{P_{h\perp 2}}{z} - k_{T2}) \qquad \text{(A.7)} \\
&\quad \times \frac{1}{z}\int d\xi \int dp_{T1}\; \left(\frac{p_{T1}}{M_N^2}\right) e^{2\pi i\xi p_{T1}} f_{1T}^{\perp}(x, p_{T1}^2 + p_{T2}^2) \\
&\quad \times \int dk_{T1} e^{-2\pi i\xi k_{T1}}\; D_1(z, z^2k_{T1}^2 + z^2k_{T2}^2) \qquad \text{(A.8)} \\
&\quad \times \int dP_{h\perp 1}\; e^{-2\pi i\xi \frac{P_{h\perp 1}}{z}} P_{h\perp 1} \qquad \text{(A.9)}
\end{aligned}
$$

The integration, (A.7), of the p_{T2}, k_{T2} and $P_{h\perp 2}$

$$
\begin{aligned}
&\int dp_{T2}\; dk_{T2}\; dP_{h\perp 2}\; \delta(p_{T2} - \frac{P_{h\perp 2}}{z} - k_{T2}) f_{1T}^{\perp}(x, p_{T1}^2 + p_{T2}^2) D_1(z, k_{T1}^2 + k_{T2}^2) \\
&= \int d\xi\; \int dp_{T2}\; e^{2\pi i\xi p_{T2}} f_{1T}^{\perp}(x, p_{T1}^2 + p_{T2}^2) \int dk_{T2}\; e^{-2\pi i\xi k_{T2}} D_1(z, k_{T1}^2 + k_{T2}^2) \\
&\quad \times \underbrace{\int dP_{h\perp 2}\; e^{-2\pi i\xi \frac{P_{h\perp 2}}{z}}}_{=z\delta(\xi)} \\
&= z\int dp_{T2}\; f_{1T}^{\perp}(x, p_{T1}^2 + p_{T2}^2) \int dk_{T2}\; D_1(z, z^2k_{T1}^2 + z^2k_{T2}^2) \underbrace{\int d\xi\; e^{2\pi i\xi(p_{T2} - k_{T2})}\delta(\xi)}_{=1}
\end{aligned}
$$

Additionally, the factor (A.9),

$$
\int dP_{h\perp 1}\; e^{-2\pi i\xi \frac{P_{h\perp 1}}{z}} P_{h\perp 1} \;=\; \left(\frac{-z^2}{2\pi i}\right)\frac{\partial}{\partial \xi}\delta\left(\xi\right)
$$

Using these relation, $I_q\Big|_1$ is re-written as follows,

$$\begin{aligned} I_q\Big|_1 &= \left(\frac{-z^2}{2\pi i}\right)\int dp_{T1}p_{T2}\ \left(\frac{p_{T1}}{M_N^2}\right) f_{1T}^{\perp}(x, p_{T1}^2 + p_{T2}^2) \\ &\quad \times \int dk_{T1}k_{T2}\ D_1(z, z^2k_{T1}^2 + z^2k_{T2}^2) \qquad \text{(A.10)} \\ &\quad \times \underbrace{\int d\xi \left(\frac{\partial}{\partial \xi}\delta(\xi)\right) e^{2\pi i\xi(p_{T1}-k_{T1})}}_{=-2\pi i(p_{T1}-k_{T1})} \qquad \text{(A.11)} \\ &= \int d\boldsymbol{p_T}\ \left(\frac{p_{T1}^2}{M_N^2}\right) f_{1T}^{\perp}(x, \boldsymbol{p_T}^2) \int d\boldsymbol{k_T}\ z^2 D_1(z, z^2\boldsymbol{k_T}^2) \qquad \text{(A.12)} \\ &\quad -\frac{z^2}{M_N^2}\int d\boldsymbol{p_T}\ (p_{T1}) f_{1T}^{\perp}(x, \boldsymbol{p_T}^2) \int d\boldsymbol{k_T}\ (k_{T1}) D_1(z, z^2\boldsymbol{k_T}^2) \qquad \text{(A.13)} \end{aligned}$$

Here, the term (A.13) is vanished, since the functions, $f_{1T}^{\perp}$ and D_1, are even function about $\boldsymbol{p_T}$ and $\boldsymbol{k_T}$.

$$\int dp_{T2}\int dp_{T1}\ p_{T1} f_{1T}^{\perp}(x, \boldsymbol{p_T}^2) = 0, \quad \int dk_{T1}\int dk_{T2}\ k_{T1} D_1(z, z^2\boldsymbol{k_T}^2) = 0$$

Finally, we obtained the $I_q\Big|_1$ as follows,

$$I_q\Big|_1 = \ = \int d\boldsymbol{p_T}\ \left(\frac{p_{T1}^2}{M_N^2}\right) f_{1T}^{\perp}(x, \boldsymbol{p_T}^2) \int d\boldsymbol{k_T}\ z^2 D_1(z, z^2\boldsymbol{k_T}^2) \qquad \text{(A.14)}$$

Using the same procedure, we obtained the $I_q\Big|_2$. Finally the I_q is written as,

$$\begin{aligned} I_q &= I_q\Big|_1 + I_q\Big|_2 \\ &= \int d\boldsymbol{p_T}\ \left(\frac{p_{T1}^2}{M_N^2}\right) f_{1T}^{\perp}(x, \boldsymbol{p_T}^2) \int d\boldsymbol{k_T}\ z^2 D_1(z, z^2\boldsymbol{k_T}^2) \qquad \text{(A.15)} \\ &\quad + \int d\boldsymbol{p_T}\ \left(\frac{p_{T2}^2}{M_N^2}\right) f_{1T}^{\perp}(x, \boldsymbol{p_T}^2) \int d\boldsymbol{k_T}\ z^2 D_1(z, z^2\boldsymbol{k_T}^2) \\ &= \int d\boldsymbol{p_T}\ \left(\frac{\boldsymbol{p_T}^2}{M_N^2}\right) f_{1T}^{\perp}(x, \boldsymbol{p_T}^2) \int d\boldsymbol{k_T}\ z^2 D_1(z, z^2\boldsymbol{k_T}^2) \qquad \text{(A.16)} \end{aligned}$$

From the results, (A.16), and definitions of $f_{1T}^{\perp(1)}(x)$ and $D_1(z)$, (A.3) and (A.4),

$$\therefore \quad \int d^2\boldsymbol{P_{h\perp}} \left(\left[\frac{P_{h\perp}}{zM_N} \right] \cdot d\sigma_{UT}^{\text{Sivers}} \right) \;=\; -\frac{2\alpha^2}{sxy^2} A(y) \sum_q e_q^2 f_{1T}^{\perp(1)}(x) D_1(z) \tag{A.17}$$

From similar procedure, the spin-averaged cross-section can be written as follows:

$$\begin{aligned} \int d^2\boldsymbol{P_{h\perp}}\; d\sigma_{UU} &= \frac{2\alpha^2}{sxy^2} A(y) \sum_q e_q^2 \int d^2\boldsymbol{p_T}\; f_1(x, \boldsymbol{p_T^2}) \int d^2\boldsymbol{k_T}\; z^2 D_1(z, z^2 \boldsymbol{k_T}^2) \\ &= \frac{2\alpha^2}{sxy^2} A(y) \sum_q e_q^2 f_1(x) D_1(z) \end{aligned} \tag{A.18}$$

Here we build up the asymmetries from (A.17), (A.18) and the definition of $D_1(z)$, Eq. (A.4) as follows:

$$\begin{aligned} A_{UT}^{Sivers}(x,y,z) &\equiv -\frac{\int d^2\boldsymbol{P_{h\perp}} \left(\left[\frac{P_{h\perp}}{zM_N} \right] \cdot d\sigma_{UT}^{\text{Sivers}} \right)}{\int d^2\boldsymbol{P_{h\perp}}\; d\sigma_{UU}} \\ &= -\frac{\sum_q e_q^2 f_{1T}^{\perp(1)}(x) D_1(z)}{\sum_q e_q^2 f_1(x) D_1(z)} \end{aligned} \tag{A.19}$$

Appendix B

Transverse Momentum of Quarks

As shown in Section 7.3.5, the intrinsic transverse momentum of quarks $\langle p_T \rangle \sim 0.7$ GeV/c was observed. From reference [45], a relation between transverse momenta can be written as,

$$\langle P_{h\perp}^2(x,z) \rangle = z^2 \left\{ \langle p_T^2(x) \rangle + \langle k_T^2(z) \rangle \right\}. \tag{B.1}$$

In the measured range used in this thesis, the corresponding mean values are; $\langle P_{h\perp} \rangle = 0.41$ GeV/c, $\langle z \rangle = 0.36$, $\langle x \rangle = 0.09$. From Eq. (B.1), the transverse momentum of the final state quark $\langle k_T \rangle$ can be computed using the kinematical mean values and observed $\langle p_T \rangle \sim 0.7$ GeV/c. The resulting, one can find the value of $\langle k_T \rangle \sim 0.5$ GeV/c. This is comparable to the result of reference [96].

For the intrinsic transverse momentum of quarks p_T, there are various theories and approaches, but at this moment, there is no unified view on it yet. In the following, some of specific approaches are explained.

1. Valence quark core
2. Perturbative QCD (pQCD) analysis
3. Soft gluon contribution

Valene quark core

From the Heisenberg uncertainty principle, one can calculate maximum possible transverse momentum $\langle p_T \rangle_{max}$. The nucleon rms radius is given $r_{rms} = 0.81$ fm, thus $c\langle p_T \rangle_{max} \simeq c\hbar / r_{rms} \sim 0.2$ GeV. On the other hand, using

observed transverse momentum $\langle p_T \rangle \sim 0.7$ GeV, one can compute $effective$ radius occupied by quarks as $r_{eff} \sim 0.3$ fm. Such small radius is led by a completely different theoretical approach [111, 112, 113, 114]. According to reference [111], the region occupied by valence quarks $r_{val} \sim 0.2$ fm and for sea-quarks is $r_{sea} = r_{rms}$. So this is so-called "valence quark core" [114]. The proposal for a valence quark core to the nucleon is further confirmed in references [112, 113]. They are independently arrive at a radius of the core $r_{val} \simeq 0.33$ fm. This is comparable with the $effective$ radius r_{eff} obtained in this analysis. As we already seen in Fig. 7.8, the sea-quark contributions for the extracted Sivers functions are small and most likely negligible. Thus it can be expected that valence-quarks are responsible for the obtained *effective* radius r_{eff}.

By introducing the valence quark core picture, the large intrinsic transverse momentum can be explained.

pQCD analyses at LO and NLO

Recently, global perturbative QCD (pQCD) analyses [98, 99] have reported the intrinsic transverse momentum evaluated using several experimental data of inclusive measurement of hadron production in proton-proton collisions for 20 GeV $\leq \sqrt{s} \leq$ 60 GeV and $\sqrt{s} \geq$ 100 GeV energies. In Fig. B.1, the results of width of the intrinsic transverse momentum $\langle p_T^2 \rangle$ as function of energy $\sqrt{s}$ are shown (note that in the figure vertical axis is labeled $\langle k_T^2 \rangle$, but this symbol corresponds to $\langle p_T^2 \rangle$ of this thesis). The results were obtained by fitting to several experimental data with leading-order (LO) and next-to-leading order (NLO) perturbative QCD parameterization with assumption of Gaussian distribution of p_T. As shown in Fig. B.1, the width of the transverse momentum reaches up to $\langle p_T^2 \rangle \sim 2$ GeV^2 in LO analysis, but the width become smaller, $\langle p_T^2 \rangle \sim 1$ GeV^2 in NLO. Both LO and NLO analysis results were obtained from the same input of experimental data. From results in Fig. B.1, the higher order pQCD contributions can magnify *real* intrinsic transverse momentum. It can be regarded that outgoing quark emits hard-gluon (gluon bremsstrahlung [96]).

Looking at Fig. B.1, the intrinsic transverse momentum depends on the energy. Basically, the energy dependence of the *observed* intrinsic transverse momentum originates from energy dependence of transverse momentum of final state hadron or jet ($cf.$ reference [115]). So if energy dependence of the hadron transverse momentum is measured in wider range and small interval, we could learn more about the quark intrinsic transverse momentum.

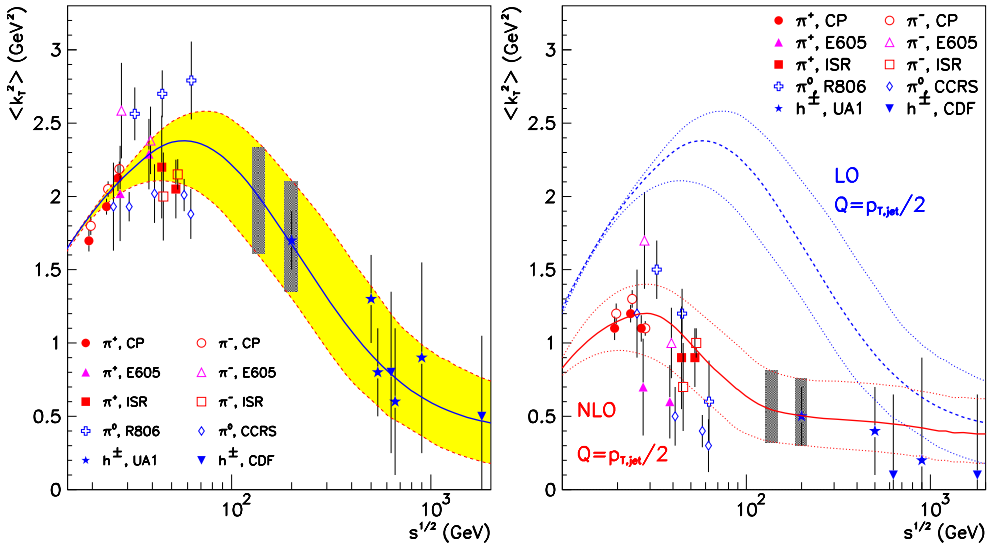

Figure B.1: Extracted intrinsic transverse momentum as function of center of mass energy $\sqrt{s}$ by leading-order (left) [98] and next-to-leading order (right) [99] pQCD analyses.

Soft gluon contribution

EMC collaboration at CERN showed interesting studies on intrinsic transverse momentum of quarks and hadrons [102, 116, 117]. They have investigated kinemaical correlation between x_F and hadron transverse momentum $P_{h\perp}$ using their data obtained from semi-inclusive measurement of charged hadron production in DIS using 280 GeV muon beam and hydrogen target. From this study, asymmetric $P_{h\perp}$ distribution between forward ($x_F > 0$) and backward ($x_F < 0$) regions was observed. To evaluate the effect of intrinsic transverse momentum, Lund model of reference [100] which includes soft gluon emission processes were used with two different input parameter sets,

Input 1 $\langle p_T^2 \rangle = 0.19$ GeV^2, soft gluon included,

Input 2 $\langle p_T^2 \rangle = 0.77$ GeV^2, soft gluon excluded.

The "Input 1" reproduced the data in both forward and backward region, namely this input reproduces the asymmetric distribution of the transverse momentum. In contrast, "Input 2" showed some discrepancies in backward region, even though this input well describes the data in forward region. From this results, the soft gluon emission, multiple soft gluon radiation from struck quark, is responsible for the observed transverse momentum.

It could be concluded that the transverse momentum, $\langle p_T \rangle_{obs} \sim 1$ GeV, extracted from experimental data is larger than *real* intrinsic transverse momentum, $\langle p_T \rangle_{real} \sim 0.2 - 0.4$ GeV (see reference [101]), due to soft gluon contributions.

Bibliography

[1] John C. Collins. Fragmentation of transversely polarized quarks probed in transverse momentum distributions. *Nucl. Phys.*, B396:161–182, 1993, hep-ph/9208213.

[2] Dennis W. Sivers. Single spin production asymmetries from the hard scattering of point - like constituents. *Phys. Rev.*, D41:83, 1990.

[3] J. Ashman et al. A measurement of the spin asymmetry and determination of the structure function g_1 in deep inelastic muon proton scattering. *Phys. Lett.*, B206:364, 1988.

[4] J. Ashman et al. An investigation of the spin structure of the proton in deep inelastic scattering of polarized muons on polarized protons. *Nucl. Phys.*, B328:1, 1989.

[5] D. h. Perkins. Introduction to high-energy physics. Reading, Usa: Addison-wesley (1982) 437p.

[6] Kuang-Ta Chao. Baryon magnetic moments with confined quarks. *Phys. Rev.*, D41:920–923, 1990.

[7] S. Eidelman et al. Review of particle physics. *Phys. Lett.*, B592:1, 2004.

[8] B. Adeva et al. Polarised quark distributions in the nucleon from semi-inclusive spin asymmetries. *Phys. Lett.*, B420:180–190, 1998, hep-ex/9711008.

[9] A. Airapetian et al. Flavor decomposition of the sea quark helicity distributions in the nucleon from semi-inclusive deep-inelastic scattering. *Phys. Rev. Lett.*, 92:012005, 2004, hep-ex/0307064.

[10] A. Airapetian et al. Quark helicity distributions in the nucleon for up, down, and strange quarks from semi-inclusive deep-inelastic scattering. 2004, hep-ex/0407032.

[11] R. L. Jaffe and Aneesh Manohar. The g_1 problem: Fact and fantasy on the spin of the proton. *Nucl. Phys.*, B337:509–546, 1990.

[12] Xiang-Dong Ji. Deeply-virtual compton scattering. *Phys. Rev.*, D55:7114–7125, 1997, hep-ph/9609381.

[13] Xiang-Dong Ji. Gauge invariant decomposition of nucleon spin. *Phys. Rev. Lett.*, 78:610–613, 1997, hep-ph/9603249.

[14] Xiang-dong Ji. Generalized parton distributions and the spin structure of the nucleon. *Nucl. Phys. Proc. Suppl.*, 119:41–49, 2003, hep-lat/0211016.

[15] R. L. Jaffe. The spin structure of the nucleon: Theoretical overview. *AIP Conf. Proc.*, 588:54–74, 2001, hep-ph/0102281.

[16] Xiao-tong Song. Orbital angular momentum in chiral quark model. 1998, hep-ph/9802206.

[17] V. A. Korotkov and W. D. Nowak. Future measurements of deeply virtual compton scattering at hermes. *Eur. Phys. J.*, C23:455–461, 2002, hep-ph/0108077.

[18] Dennis W. Sivers. Hard scattering scaling laws for single spin production asymmetries. *Phys. Rev.*, D43:261–263, 1991.

[19] Xiang-dong Ji, Jian-Ping Ma, and Feng Yuan. Three-quark light-cone amplitudes of the proton and quark-orbital-motion dependent observables. *Nucl. Phys.*, B652:383–404, 2003, hep-ph/0210430.

[20] Zhun Lu and Bo-Qiang Ma. Sivers function in light-cone quark model and azimuthal spin asymmetries in pion electroproduction. *Nucl. Phys.*, A741:200–214, 2004, hep-ph/0406171.

[21] Matthias Burkardt and Dae Sung Hwang. Sivers asymmetry and generalized parton distributions in impact parameter space. *Phys. Rev.*, D69:074032, 2004, hep-ph/0309072.

[22] Matthias Burkardt. Chromodynamic lensing and transverse single spin asymmetries. *Fizika*, B13:565–576, 2004, hep-ph/0309269.

[23] Matthias Burkardt. Quark correlations and single-spin asymmetries. 2004, hep-ph/0408009.

[24] Bo-Qiang Ma and Ivan Schmidt. The quark orbital angular momentum in a light-cone representation. *Phys. Rev.*, D58:096008, 1998, hep-ph/9808202.

[25] Xiang-Song Chen. Magnetic moment, spin structure and tensor charge of the baryon. 1998, hep-ph/9802347.

[26] Xiang-Song Chen, Di Qing, Wei-Min Sun, Hong-Shi Zong, and Fan Wang. Spin orbital structure of the nucleon magnetic moment. *Phys. Rev.*, C69:045201, 2004.

[27] R. D. Klem et al. Measurement of asymmetries of inclusive pion production in proton proton interactions at 6 GeV/c and 11.8 GeV/c. *Phys. Rev. Lett.*, 36:929–931, 1976.

[28] W. H. Dragoset et al. Asymmetries in inclusive proton - nucleon scattering at 11.75 GeV/c. *Phys. Rev.*, D18:3939–3954, 1978.

[29] J. Antille et al. Spin dependence of the inclusive reaction p p (polarized) $\rightarrow$ pi0 X at 24 GeV/c for high p_t pi0 produced in the central region. *Phys. Lett.*, B94:523, 1980.

[30] A. Bravar et al. Single-spin asymmetries in inclusive charged pion production by transversely polarized antiprotons. *Phys. Rev. Lett.*, 77:2626–2629, 1996.

[31] D. L. Adams et al. Comparison of spin asymmetries and cross-sections in pi0 production by 200 GeV polarized anti-protons and protons. *Phys. Lett.*, B261:201–206, 1991.

[32] D. L. Adams et al. Analyzing power in inclusive pi+ and pi- production at high x_f with a 200 GeV polarized proton beam. *Phys. Lett.*, B264:462–466, 1991.

[33] J. Adams et al. Cross sections and transverse single-spin asymmetries in forward neutral pion production from proton collisions at $\sqrt{s} = 200$ GeV. *Phys. Rev. Lett.*, 92:171801, 2004, hep-ex/0310058.

[34] K. Hasuko, M. Grosse Perdekamp, A. Ogawa, J. S. Lange, and V. Siegle. Future measurements of spin dependent fragmentation functions in e+ e- annihilation at belle. *AIP Conf. Proc.*, 698:628–631, 2004.

[35] P. J. Mulders and R. D. Tangerman. The complete tree-level result up to order $1/Q$ for polarized deep-inelastic leptoproduction. *Nucl. Phys.*, B461:197–237, 1996, hep-ph/9510301.

[36] Daniel Boer and P. J. Mulders. Time-reversal odd distribution functions in leptoproduction. *Phys. Rev.*, D57:5780–5786, 1998, hep-ph/9711485.

[37] A. Airapetian et al. Measurement of single-spin azimuthal asymmetries in semi-inclusive electroproduction of pions and kaons on a longitudinally polarised deuterium target. *Phys. Lett.*, B562:182–192, 2003, hep-ex/0212039.

[38] E. Leader. *Spin In Particle Physics*. Cambridge University Press, 2001. ed. T .Ericson, P. V. Landshoff.

[39] Mauro Anselmino, Mariaelena Boglione, and Francesco Murgia. Phenomenology of single spin asymmetries in p(pol.) p $\rightarrow \pi X$. *Phys. Rev.*, D60:054027, 1999, hep-ph/9901442.

[40] M. Anselmino, Mariaelena Boglione, J. Hansson, and F. Murgia. Predictions for single spin asymmetries in lp(pol.) $\rightarrow \pi X$ and γ^*p(pol.) $\rightarrow \pi X$. *Eur. Phys. J.*, C13:519–526, 2000, hep-ph/9906418.

[41] Robert L. Jaffe. Spin, twist and hadron structure in deep inelastic processes. 1996, hep-ph/9602236.

[42] M. Osipenko et al. Self-consistent data analysis of the proton structure function g_1 and extraction of its moments. 2004, hep-ex/0409038.

[43] A. Bacchetta, Mariaelena Boglione, A. Henneman, and P. J. Mulders. The full spin structure of quarks in the nucleon. 2000, hep-ph/0005140.

[44] John C. Collins and Davison E. Soper. Parton distribution and decay functions. *Nucl. Phys.*, B194:445, 1982.

[45] Alessandro Bacchetta. Probing the transverse spin of quarks in deep inelastic scattering. 2002, hep-ph/0212025.

[46] Alessandro Bacchetta, Umberto D'Alesio, Markus Diehl, and C. Andy Miller. Single-spin asymmetries: The trento conventions. *Phys. Rev.*, D70:117504, 2004, hep-ph/0410050.

[47] S. J. Brodsky, D. S. Hwang, and I. Schmidt. Final state interactions and single spin asymmetries in semiinclusive deep inelastic scattering. *Int. J. Mod. Phys.*, A18:1327–1334, 2003.

[48] Daniel Boer, P. J. Mulders, and F. Pijlman. Universality of T-odd effects in single spin and azimuthal asymmetries. *Nucl. Phys.*, B667:201–241, 2003, hep-ph/0303034.

[49] John C. Collins and Andreas Metz. Universality of soft and collinear factors in hard- scattering factorization. *Phys. Rev. Lett.*, 93:252001, 2004, hep-ph/0408249.

[50] M. Anselmino, U. D'Alesio, and F. Murgia. Transverse single spin asymmetries in Drell-Yan processes. *Phys. Rev.*, D67:074010, 2003, hep-ph/0210371.

[51] C. J. Bomhof, P. J. Mulders, and F. Pijlman. Gauge link structure in quark quark correlators in hard processes. *Phys. Lett.*, B596:277–286, 2004, hep-ph/0406099.

[52] John C. Collins. Leading-twist single-transverse-spin asymmetries: Drell-Yan and deep-inelastic scattering. *Phys. Lett.*, B536:43–48, 2002, hep-ph/0204004.

[53] D. Muller, D. Robaschik, B. Geyer, F. M. Dittes, and J. Horejsi. Wave functions, evolution equations and evolution kernels from light-ray operators of QCD. *Fortschr. Phys.*, 42:101, 1994, hep-ph/9812448.

[54] Xiang-Dong Ji. Gauge invariant decomposition of nucleon spin. *Phys. Rev. Lett.*, 78:610–613, 1997, hep-ph/9603249.

[55] A. V. Radyushkin. Nonforward parton densities and soft mechanism for form factors and wide-angle compton scattering in QCD. *Phys. Rev.*, D58:114008, 1998, hep-ph/9803316.

[56] Mauro Anselmino and Francesco Murgia. Single spin asymmetries in p(pol.) p and anti-p(pol.) p inclusive processes. *Phys. Lett.*, B442:470–478, 1998, hep-ph/9808426.

[57] Mariaelena Boglione and P. J. Mulders. Time-reversal odd fragmentation and distribution functions in p p and e p single spin asymmetries. *Phys. Rev.*, D60:054007, 1999, hep-ph/9903354.

[58] Alessandro Bacchetta, Andreas Schaefer, and Jian-Jun Yang. Sivers function in a spectator model with axial-vector diquarks. *Phys. Lett.*, B578:109–118, 2004, hep-ph/0309246.

[59] Feng Yuan. Sivers function in the mit bag model. *Phys. Lett.*, B575:45–54, 2003, hep-ph/0308157.

[60] R. Jakob, P. J. Mulders, and J. Rodrigues. Modelling quark distribution and fragmentation functions. *Nucl. Phys.*, A626:937–965, 1997, hep-ph/9704335.

[61] J. D. Jackson, Graham G. Ross, and R. G. Roberts. Polarized structure functions in the parton model. *Phys. Lett.*, B226:159, 1989.

[62] K. Ackerstaff et al. Hermes spectrometer. *Nucl. Instrum. Meth.*, A417:230–265, 1998, hep-ex/9806008.

[63] A. A. Sokolov and I. M. Ternov. On polarization and spin effects in the theory of synchrotron radiation. *Phys. Dokl.*, 8:1203–1205, 1964.

[64] S. Bernreuther et al. The HERMES back drift chambers. *Nucl. Instrum. Meth.*, A416:45–58, 1998, hep-ex/9803005.

[65] M. Kobayashi *et al*. *KEK internal report*, 93-015, 1993.

[66] H. Avekian *et al*. Performance of F101 radiation resistant lead glass shower counters. *Nucl. Instr. and Meth.*, A378:155, 1993.

[67] F. M. Menden R. Kaiser and M. C. Vetterli. Probability Analysis of the TRD Response and the Contribution of Flus Ratios to HERMES Particle. *HERMES Internal*, 97-036, 1997.

[68] K. Suetsugu. Performance of pion kaon and proton identification with ring imaging Čerenkov counter of hermes. 2001, DESY-THESIS-2001-016.

[69] H. Tanaka et al. A gain monitoring system with a Nd:YAG laser for the photomultipliers of the hermes experiment. *Nucl. Instrum. Meth.*, A515:725–732, 2003.

[70] Leonard P. Gamberg, Gary R. Goldstein, and Karo A. Oganessyan. Novel transversity properties in semi-inclusive deep inelastic scattering. *Phys. Rev.*, D67:071504, 2003, hep-ph/0301018.

[71] A. Airapetian et al. Observation of a single-spin azimuthal asymmetry in semi-inclusive pion electro-production. *Phys. Rev. Lett.*, 84:4047–4051, 2000, hep-ex/9910062.

[72] A. Airapetian et al. Single-spin azimuthal asymmetries in electroproduction of neutral pions in semi-inclusive deep-inelastic scattering. *Phys. Rev.*, D64:097101, 2001, hep-ex/0104005.

[73] The hermes polarized hydrogen and deuterium gas target in the hera electron storage ring. 2004, physics/0408137.

[74] Stanley J. Brodsky, Paul Hoyer, Nils Marchal, Stephane Peigne, and Francesco Sannino. Structure functions are not parton probabilities. *Phys. Rev.*, D65:114025, 2002, hep-ph/0104291.

[75] Torbjorn Sjostrand, Leif Lonnblad, and Stephen Mrenna. Pythia 6.2: Physics and manual. 2001, hep-ph/0108264.

[76] K. Goeke, Maxim V. Polyakov, and M. Vanderhaeghen. Hard exclusive reactions and the structure of hadrons. *Prog. Part. Nucl. Phys.*, 47:401–515, 2001, hep-ph/0106012.

[77] Qing-Hua Xu and Zuo-Tang Liang. Contribution of vector meson dominance to the single-spin azimuthal asymmetry in semiinclusive pion electro- production. *Chin. Phys. Lett.*, 18:1021–1023, 2001.

[78] Daniel Boer and Werner Vogelsang. Asymmetric jet correlations in p p(pol.) scattering. *Phys. Rev.*, D69:094025, 2004, hep-ph/0312320.

[79] Jian-wei Qiu and George Sterman. Single transverse-spin asymmetries in hadronic pion production. *Phys. Rev.*, D59:014004, 1999, hep-ph/9806356.

[80] Yuji Koike. Single transverse spin asymmetry in p(pol.) p $\rightarrow$ pi x and e p(pol.) $\rightarrow$ pi x. *Nucl. Phys.*, A721:364–367, 2003, hep-ph/0211400.

[81] R. Brun, F. Bruyant, M. Maire, A. C. McPherson, and P. Zanarini. Geant3. CERN-DD/EE/84-1.

[82] G. Ingelman, A. Edin, and J. Rathsman. Lepto 6.5 - a monte carlo generator for deep inelastic lepton-nucleon scattering. *Comput. Phys. Commun.*, 101:108–134, 1997, hep-ph/9605286.

[83] I. Akushevich, H. Bottcher, and D. Ryckbosch. Radgen 1.0: Monte carlo generator for radiative events in dis on polarized and unpolarized targets. 1998, hep-ph/9906408.

[84] I. V. Akushevich and N. M. Shumeiko. Radiative effects in deep inelastic scattering of polarized leptons by polarized light nuclei. *J. Phys.*, G20:513–530, 1994.

[85] A. V. Afanasev, I. Akushevich, G. I. Gakh, and N. P. Merenkov. Radiative corrections to polarized inelastic scattering in coincidence. *J. Exp. Theor. Phys.*, 93:449–461, 2001, hep-ph/0105032.

[86] A. Miller. Applying radiative correction to polarized asymmetries for deep inelastic scattering. *To be published.*

[87] K. Rith. Spin asymmetries in deep-inelastic electron nucleon scattering: Selected hermes results. *Prog. Part. Nucl. Phys.*, 49:245–324, 2002.

[88] H. L. Lai et al. Global QCD analysis of parton structure of the nucleon: CTEQ5 parton distributions. *Eur. Phys. J.*, C12:375–392, 2000, hep-ph/9903282.

[89] J. Pumplin et al. New generation of parton distributions with uncertainties from global qcd analysis. *JHEP*, 07:012, 2002, hep-ph/0201195.

[90] K. Abe et al. Measurements of R = sigma(l)/sigma(t) for $0.03 < x < 0.1$ and fit to world data. *Phys. Lett.*, B452:194–200, 1999, hep-ex/9808028.

[91] L. W. Whitlow, Stephen Rock, A. Bodek, E. M. Riordan, and S. Dasu. A precise extraction of R = sigma-l / sigma-t from a global analysis of the slac deep inelastic e p and e d scattering cross-sections. *Phys. Lett.*, B250:193–198, 1990.

[92] Stefan Kretzer, Elliott Leader, and Ekaterina Christova. Fragmentation functions from semi-inclusive dis pion production and implications for the polarized parton densities. *Eur. Phys. J.*, C22:269–276, 2001, hep-ph/0108055.

[93] S. Kretzer. Fragmentation functions from flavour-inclusive and flavour-tagged e+ e- annihilations. *Phys. Rev.*, D62:054001, 2000, hep-ph/0003177.

[94] Bernd A. Kniehl, G. Kramer, and B. Potter. Fragmentation functions for pions, kaons, and protons at next-to-leading order. *Nucl. Phys.*, B582:514–536, 2000, hep-ph/0010289.

[95] L. C. Bland. Star results from polarized proton collisions at rhic. 2004, hep-ex/0403012.

[96] R. P. Feynman, R. D. Field, and G. C. Fox. Quantum-chromodynamic approach for the large-transverse- momentum production of particles and jets. *Phys. Rev.*, D18:3320, 1978.

[97] M. D. Corcoran et al. Evidence for multiple scattering of high-energy partons in nuclei. *Phys. Lett.*, B259:209–215, 1991.

[98] Yi Zhang, George I. Fai, Gabor Papp, Gergely G. Barnafoldi, and Peter Levai. High-p_t pion and kaon production in relativistic nuclear collisions. *Phys. Rev.*, C65:034903, 2002, hep-ph/0109233.

[99] G. G. Barnafoldi, George I. Fai, P. Levai, G. Papp, and Y. Zhang. Jets and produced particles in p p collisions from sps to rhic energies for nuclear applications. *J. Phys.*, G27:1767–1774, 2001, nucl-th/0004066.

[100] Gunnar Ingelman, Bo Andersson, Gosta Gustafson, and Torbjorn Sjostrand. Transverse momentum effects and angular energy flow in lepto-production. *Nucl. Phys.*, B206:239, 1982.

[101] P. K. Malhotra and R. Orava. A determination of intrinsic transverse momentum of quarks. *Z. Phys.*, C18:53, 1983.

[102] M. Arneodo et al. Transverse momentum and its compensation in current and target jets in deep inelastic muon - proton scattering. *Phys. Lett.*, B149:415, 1984.

[103] E. Bonvin et al. Intrinsic transverse momentum in the pi- p $\rightarrow$ gamma gamma x reaction at 280 GeV/c. *Phys. Lett.*, B236:523, 1990.

[104] Nikolai N. Nikolaev. Intrinsic k_t in the pomeron. 1998, hep-ph/9905562.

[105] M. A. Kimber, Alan D. Martin, and M. G. Ryskin. Unintegrated parton distributions. *Phys. Rev.*, D63:114027, 2001, hep-ph/0101348.

[106] M. Anselmino, M. Boglione, U. D'Alesio, E. Leader, and F. Murgia. Parton intrinsic motion: Suppression of the collins mechanism for transverse single spin asymmetries in p(pol.) p $\rightarrow$ pi x. *Phys. Rev.*, D71:014002, 2005, hep-ph/0408356.

[107] Hung-Liang Lai and Hsiang-nan Li. Origin of the k_t smearing in direct photon production. *Phys. Rev.*, D58:114020, 1998, hep-ph/9802414.

[108] Cheuk-Yin Wong and Hui Wang. Effects of parton intrinsic transverse momentum on photon production in hard-scattering processes. *Phys. Rev.*, C58:376–388, 1998, hep-ph/9802378.

[109] Xiao-feng Guo and Jian-wei Qiu. Nuclear dependence in direct photon production. *Phys. Rev.*, D53:6144–6155, 1996, hep-ph/9512262.

[110] B. Cox and P. K. Malhotra. Comparison of energy dependence of transverse momentum of dimuons produced in p n and pi- n interactions with qcd predictions. *Phys. Rev.*, D29:63, 1984.

[111] Jay Orear. Evidence for a proton core. *Phys. Rev.*, D18:2484, 1978.

[112] G. E. Brown and Mannque Rho. The little bag. *Phys. Lett.*, B82:177–180, 1979.

[113] G. E. Brown, Mannque Rho, and Vicente Vento. Little bag dynamics. *Phys. Lett.*, B84:383, 1979.

[114] Jay Orear. A determination of quark intrinsic transverse momentum. CLNS-80/446.

[115] J. K. Yoh et al. Study of scaling in hadronic production of dimuons. *Phys. Rev. Lett.*, 41:684, 1978.

[116] J. J. Aubert et al. Balance of transverse momentum of hadrons produced in deep inelastic muon proton scattering. *Phys. Lett.*, B119:233, 1982.

[117] M. Arneodo et al. Charge and transverse momentum correlations in deep inelastic muon - proton scattering. *Z. Phys.*, C31:333, 1986.

List of Figures